

University of St Andrews



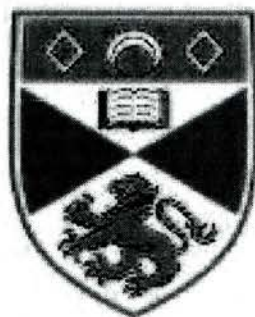
Full metadata for this thesis is available in
St Andrews Research Repository
at:

<http://research-repository.st-andrews.ac.uk/>

This thesis is protected by original copyright

Design and Development of a Microfabricated Sensor for Biochemical Detection

Naiara Elejalde Ochandiano



Thesis Submitted for the Degree of Doctor of Philosophy of
the University of St. Andrews on 11th October 2002.

TH
E336

Declaration

I, Naiara Elejalde Ochandiano, hereby certify that this thesis, which is approximately 40,000 words in length, has been written by me, that it is the record of work carried out by me and that it has not been submitted in any previous application for a higher degree.

datesignature of candidate

I was admitted as a research student in October 1998 and as a candidate for the degree of PhD in October 1999; the higher study for which this is a record was carried out in the University of St. Andrews between October 1998 and October 2002 .

datesignature of candidate

I hereby certify that the candidate has fulfilled the conditions of the Resolution and Regulations appropriate for the degree of PhD in the University of St. Andrews and that the candidate is qualified to submit this thesis in application for that degree.

datesignature of supervisor

In submitting this thesis to the University of St. Andrews I understand that I am giving permission for it to be made available for use in accordance with the regulations of the University Library for the time being in force, subject to any copyright vested in the work not being affected thereby. I also understand that the title and abstract will be published, and that a copy of the work may be made and supplied to any bona fide library or research worker.

datesignature of candidate

To who believed in me.

Caminante, no hay camino,
se hace camino al andar.
Al andar se hace camino,
y al volver la vista atrás
se ve la senda que nunca
se ha de volver a pisar.

Antonio Machado



1. I imaging when I am an engineer, puf!
2. Weelll. I'll design a bridggee
3. No, I won't be the way I'm now! When I am an engineer I won't be the way I am now!
4. Because I will be famous and everybody will want me to build dikes and roads and factories and tunnels and aqueducts and...
5. Oh Lord! How will I get everything done?

DESIGN AND DEVELOPMENT OF A MICROFABRICATED SENSOR FOR BIOCHEMICAL DETECTION

ABSTRACT

This thesis is concerned with the design and development of a highly sensitive sensor based on micromechanical resonating elements which would be suitable for routine application in molecular probe chemistry for biological research. The sensor will work by monitoring the changes in the resonant properties of the device, mainly resonant frequency, due to the accumulation of reaction product at the sensor surface.

The motivation behind this work was the desire to develop a sensor capable of overcoming the limitations of the technology available. Until recent years the research has been focused on optimising piezoelectric crystal-based gravimetric devices, the practical limitations encountered suggested the need for an alternative approach. These limitations can be overcome by oscillating cantilevers, the design of which will depend on the nature of the application.

A first generation of devices were designed and microfabricated successfully. Basic mechanical analysis was used to optimise the dimensions in order to achieve the required force constant, and finite element analysis was used to further refine the geometry. The chosen route involved actuation of the sensors via tiny magnetic elements adhered to the surface of the resonator, and detection via piezoresistors placed in the cantilever legs. A prototype measurement system was constructed which would be suitable for application in a portable device capable of being used in challenging environments. This system was subsequently used to demonstrate the feasibility of this approach, and some preliminary examples of dynamic reaction monitoring were undertaken.

Major consideration was given to the actuation mechanism. Since it is fundamental for mass-produced sensors to be fabricated reproducibly, the magnetic elements needed to be implemented within the process, necessitating the study of several different approaches. Electrodeposition was chosen as the technique for the growth of high-aspect ratio magnetic particles, and their magnetic properties were carefully characterised.

The work undertaken has demonstrated the feasibility of this approach to chemical detection, and forms the basis for future development work in electronic integration, instrumentation and optimisation of device morphology for specific chemical sensing applications.

Contents

1	Chemical Detection Review	1
1.1	Introduction	1
1.2	Biochemical Detection	2
1.3	Sensors Review	6
1.3.1	Summary of Micromechanical Sensors	10
1.4	Excitation and Detection Mechanisms in Silicon	11
1.4.1	Electrostatic Excitation	12
1.4.2	Magnetic Excitation	12
1.4.3	Thermal Excitation	13
1.4.4	Piezoelectric Excitation and Detection	14
1.4.5	Optical Detection	14
1.4.6	Piezoresistive Detection	15
1.4.7	Capacitive Detection	15
1.5	Conclusions	16
2	Cantilevers Design Criteria and Selection	22
2.1	Introduction	22
2.2	Geometrical Design	23

2.3	Mechanical Properties of the Cantilevers	23
2.3.1	Force Constant of a V-shaped Microcantilever Paddle	24
2.4	Natural Frequencies	26
2.4.1	Harmonic Oscillation Theory	27
2.4.1.1	Effect of Varying the Damping Term	31
2.4.1.2	Frequency Shift	33
2.4.2	Q Factor	36
2.4.3	Surroundings Damping Mechanisms	38
2.4.3.1	Viscous Damping	38
2.4.3.2	Acoustic Damping	38
2.4.3.3	Squeezed Film Damping	39
2.4.4	Structural Damping	39
2.4.5	Internal Loss Mechanism	40
2.4.6	Summary of the Q Factor	41
2.5	Silicon Properties	41
2.5.1	Piezoresistivity	42
2.5.2	The Piezoresistive Sensitivity	48
2.6	Conclusions	51
3	Finite Element Analysis of the Cantilevers	56
3.1	Introduction	56
3.2	FEA Modelling	57
3.2.1	Model Building	58
3.2.2	Modal Analysis Theory	60
3.2.3	Review of the Results	62
3.3	Model validation	63

3.3.1	Determination of the right angle	65
3.3.2	Strain in the Cantilever Paddles	66
3.4	Cantilevers with a Long Iron Cylinder attached to the Paddle	68
3.5	Cantilevers with the Electroplated Nickel Pillars	70
3.6	Conclusions	72
4	Batch Process	75
4.1	Introduction	75
4.2	Silicon Microfabrication Techniques	76
4.2.1	Oxidation	76
4.2.1.1	Wet and Dry Oxidation	78
4.2.1.2	Low Temperature Oxidation (LTO)	79
4.2.1.3	Preoxidation Surface Cleaning	80
4.2.1.4	Oxide Charges	81
4.2.1.5	Masking Properties	83
4.2.1.6	Passivation	84
4.2.2	Lithography	84
4.2.2.1	Photoresist	86
4.2.3	Impurity Diffusion and Ion Implantation	88
4.2.4	Etching	89
4.2.4.1	Wet Etching	91
4.2.4.2	Dry Etching	93
4.3	Mask Design	95
4.4	Processing of The First Batch	99
4.5	Conclusions	103

5	Preliminary Experimental Results on the Microfabricated Cantilevers	107
5.1	Introduction	107
5.2	Magnetic Excitation	108
5.2.1	Optimisation of Coil Geometry	108
5.2.1.1	On-Axial Field Due to a Current Loop	109
5.2.1.2	Axial Field of a Finite, Thin Shell Solenoid	110
5.2.1.3	Axial Field of a Finite Solenoid	111
5.2.2	Torque Mode	113
5.2.3	Force Mode	114
5.2.4	Summary of Driving Mechanism	116
5.3	Piezoresistive Detection	116
5.3.1	Wheatstone Bridge	116
5.3.2	Noise in Piezoresistors	119
5.3.2.1	Johnson Noise	121
5.3.2.2	1/f Noise	122
5.3.2.3	Thermo-Mechanical Noise	123
5.3.3	Sensitivity	124
5.4	Experimental Set-up and Electronic Considerations	126
5.4.1	Study of the Circuit	127
5.5	Initial Results	130
5.6	Conclusions	136
6	Microfabrication and Design of Magnetic Particles	140
6.1	Introduction	140
6.2	Fabrication Techniques	141
6.2.1	Ion Beam Milling	141

6.2.2	Lift-Off	146
6.2.3	Electroplating	148
6.3	Moulds for Electroplating	150
6.3.1	SU-8 Negative Photoresist	151
6.3.2	SPR220-7 Positive Photoresist	157
6.3.2.1	Electroplating of the Moulds	160
6.3.2.2	Magnetic Properties of the Electroplated Pillars	164
6.3.3	Summary of Microfabrication Techniques for Creating High-Aspect Ratio Magnetic Particles	166
6.4	Cantilevers With Integrated Ni Pillars	167
6.5	Conclusions	172
7	Conclusions and Further Work	177
7.1	Conclusions	177
7.2	Future Work	180
	Appendixes	184
A	Detailed Resolution of the Mechanical Properties	184
A.1	Cantilevers Design Criteria and Selection	184
A.2	β Correction Factor for the Piezoresistors	189
B	Process Listings	194
B.1	Simple Cantilever Paddles	195
B.2	Cobalt Etching with Ion-beam Miller	197
B.3	Cobalt Lift-off	197
B.4	Test for Electroplating	198
B.5	Cantilevers with Electroplated Nickel Using SU-8 Photoresist	199

B.6	Cantilevers with Electroplated Nickel Using SPR220-7 Photoresist	202
C	Finite Element Analysis	205
C.1	Determination of The Right Angle	205
C.2	Iron Magnetic Particle	208
C.3	Mass Sensitivity with Iron Magnetic Particle	211

Chapter 1

Chemical Detection Review

1.1 Introduction

The ability to exclusively identify the presence of a particular chemical species is an extremely powerful tool in fields as diverse as biomedical diagnostics, environmental monitoring, gene probe chemistry, agriculture, forensic science, counterfeiting and chemical defence.

However, the increasing demand for medical diagnosis has implications on health care costs. As the demands of diagnostic laboratories increases, the health cost rises and the necessity for rapid and non-expensive medical tests is becoming increasingly apparent [1, 2, 3, 4]. A reduction in sample and test reagent volumes along with the improved detection and increased ease of automation are necessary to both reduce the cost of diagnosis and increase the speed in obtaining results.

The implementation of microfabricated devices in the research laboratory has raised these issues in all areas of laboratory testing, from sample preparation [5] to sample reaction, separation and detection [6, 7, 8, 9]. As a consequence of the miniaturisation of the diagnostic test environment, the reaction chamber, the sample to be studied and the detection appara-

tus are minimised. A reduction in the sample to be studied means that less of the potentially infectious specimen is necessary, translating into smaller samples taken from patients. With smaller reaction chambers, a faster reaction [10] is possible using only nanolitre to femtolitre volumes of reagents. A smaller detection apparatus leads to a reduction of the reacted sample needed for measurement. The combination of these three microsystems on one microfabricated device will create a single micro total analysis system (μ TAS) performing a task of several large instruments [11]. This approach presents a number of new challenges, for example the difficulty of mixing fluids in micro-vessels [12]. There is thus a requirement for novel actuators and sensors that are compatible with this emerging technology.

1.2 Biochemical Detection

Until very recently, particularly in the field of biochemical analysis, the number of approaches to highly quantitative detection of a particular species were very limited. Indeed, a great many methods are concerned with an end-point determination, that is, whether or not the species is present, measured relative to some threshold sensitivity. In terms of quantitative methods the use of conjugated dyes and fluorescent labels, which are activated by specific chemical reactions, are now extremely important. In the case of an antibody the label may for instance be fluorescent, radioactive or enzymatic, which is either directly attached to a primary antibody or attached to a secondary antibody which recognises the antigen.

A typical example is the ELISA (enzyme-linked immunosorbent assay), dyes are commonly employed in ELISA, which exploit the specificity of antibodies in order to detect tiny amounts of a specific protein. In these reactions antibodies with a highly specific affinity for a given antigen are immobilised on the walls of a PVC microwell plate. Addition of a biological sample will cause the target antigen, if present, to bind to the immobilised antibody, and any unattached molecules are subsequently washed away. A second antibody specific

to a different site on the antigen is then added, which becomes attached to the immobilised antigen, as can be seen illustrated in Fig. 1.1.

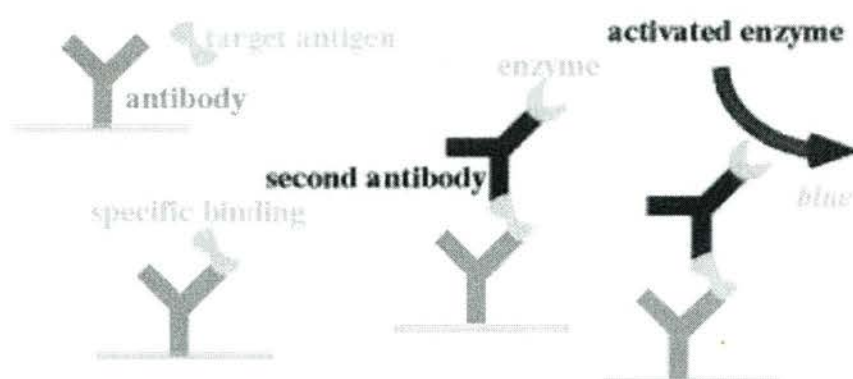


Figure 1.1: Schematic of an ELISA reaction for the specific detection of an antigen. The binding is detected by the activation of a dye.

If the second antibody has previously been attached to an appropriate enzyme, such as alkaline phosphatase, this can be activated with a substrate into a coloured or fluorescent product [13].

Gene probes, to identify a specific DNA target sequence, can be labelled in a similar manner, and can be extremely sensitive if combined with an amplification technique such as the polymerase chain reaction (PCR) [13]. The PCR reaction, for which Mullis won the Noble Prize in 1984, allows the selective amplification of sequences of DNA (or RNA), called *amplicons*, provided that short sequences either side of the amplicon are known (the primer sequence). PCR allows extremely large numbers of copies of the amplicon to be made *in vitro*, thus allowing the easy detection of target sequences initially present in tiny amounts. By combining this approach with the use of a fluorogenic label, it is possible to

confirm the presence of tiny amount of target material. Nevertheless, precise quantification of actual concentrations is difficult, since it involves extrapolation of signal obtained from measurements of high numbers of binding events and careful calibration of the system. This approach ideally also requires a dynamic monitoring of the amplification process, rather than a single 'end-point' analysis.

Direct detection of small amounts of antigen or target DNA sequence is also limited by sensitivity, particularly due to the signals arising from non-specific binding products. High specificity sensitive end-point measurement techniques, such as the Southern blotting method which combines gel electrophoresis with radioactive labelling for detecting specific DNA sequences, are both labour intensive and difficult to automate. This precludes their routine application in many situations especially where cost is an important consideration. More conventional gel electrophoresis techniques, which separate DNA fragments according to molecular weight, are also subject to uncertainty as specificity is only implied indirectly from the fragment size. Similar arguments apply to melting point determinations of reaction products.

Both the ELISA and PCR reactions can be highly automated using modern commercial devices such as plate readers, which automatically examine large arrays of microplate wells, or sequentially interrogate small glass capillaries in PCR machines such as the LightCyclerTM [14]. The latter represents in some sense a dynamic measurement, in as much as the quantity of material is assessed after each cycle. Yet the development of truly dynamic reaction monitoring is of increasing importance, particularly in view of innovative approaches to understanding biomolecular function in terms of kinetic and affinity constants e.g. [15]. In this context the development of surface plasmon resonance (SPR) studies of species immobilised on membranes is a particularly promising approach to label-free dynamic specific detection [15].

There are some general requirements on an ideal specific detection system for μ TAS and

other applications. High sensitivity is obviously important, but this is not only dependent on the physical detection system. In particular, non-specific adsorption or adhesion can lead to a background level, below which it is not possible to detect target species. This relies heavily on appropriate biochemical protocols to ‘block’ sites where unwanted species might attach. Approaches to solve this problem obviously depend critically on the particular detection mechanism and reaction type. Ideally, probes should also be capable of operating in fluids. As in the case of the SPR mentioned above, the ability not only to measure small masses of product but also to operate in small volumes is useful, particularly in a μ TAS context. A move to automate and miniaturise conventional approaches is one option. For instance, while modern PCR machines such as that in [14] operate on modest yet macroscopic volumes, the successful operation of a rapid-cycling micromachined silicon PCR chip has recently been demonstrated. The use of microfabrication to develop μ TAS systems naturally raises the possibility of using micromechanical elements as detection systems.

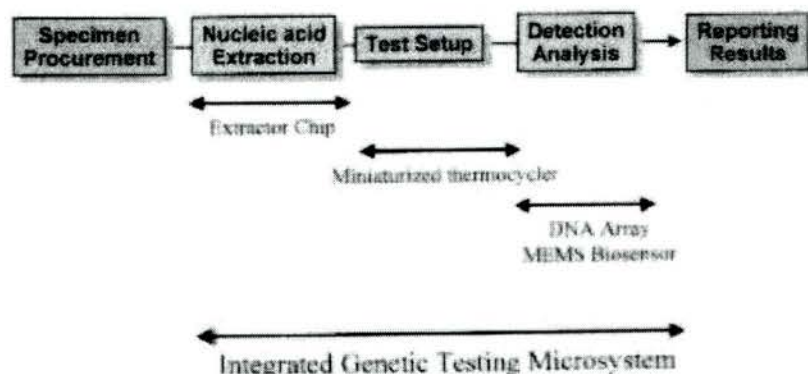


Figure 1.2: Operational scheme of a molecular diagnostics laboratory [16].

In the attempt to create a portable and cost effective specific chemical detection system, there has been a need to converge expertise in molecular biology and engineering. The challenge remains to design miniaturised laboratory components that can be produced economically, are very small, and have performance superior to macroscale systems. Micro-electromechanical systems (MEMS) are one potential solution since the silicon processing

industry allows a decrease in the production cost, while permitting the exploration of new principles of sensing not possible with conventional techniques. Fig. 1.2 shows the operational schema of specific chemical detection, including the sample collection.

1.3 Sensors Review

MEMS provide a means to make microminiaturised devices that do physical work such as pumping, valving, and oscillating, that could serve as actuators. Physical sensors are the primary commercial application of MEMS, although new approaches towards combining the mechanical features of MEMS with biological materials are laying the foundation for a whole new class of biosensors. MEMS systems can be configured into highly portable and inexpensive instrumentation.

The manufacture of MEMS involves processes common to IC technology, such as photolithography, surface machining, deposition of thin films, and bulk micromachining. These techniques are explained in detailed in Chapter 4.

True MEMS sensors have only recently been shown to also function as biochips. MEMS devices take advantage of certain mechanical properties of structures that have analogues in the macroscale world. Examples of macroscopic piezoelectric devices are the so-called quartz crystal microbalance (QCM) [17, 18, 19], the surface acoustic wave sensor (SAW) [20, 21] and acoustic plate mode (APM) [22].

In 1959 Sauerbrey provided a description and experimental proof of the mass-frequency relation for foreign layers deposited on thickness-shear mode crystals that are still widely used today for determination of mass changes at the surface of shear mode transducers [23]. This mass sensing format is commonly known as the QCM. The derivation of the mass-frequency relation implicitly relies on the assumption that the deposited foreign material

exists entirely at the antinode of the standing wave propagating across the thickness of the quartz crystal, so that the deposition could be treated as an extension of the quartz crystal. The QCM adapted to the liquid medium may give a direct response signal which characterises the binding event between a sensitive layer, grafted onto the surface transducer, and the analyte to be detected [24].

Piezoelectric mass detection can also be accomplished with other vibrational modes. SAW devices generally comprise two pairs of closely spaced interdigitated electrodes separated by a region of piezoelectric substrate. An alternating electric field applied by the transmitter pair of electrodes produces a periodic strain that launches an acoustic wave. The interaction of the surface wave with a foreign mass in the region between the two arrays results in a change in the SAW velocity and amplitude. This can be sensed by the interaction of the SAW with the interdigitated electrodes at the receiver end as a change in the signal intensity produced or a change in the arrival time of the wave with respect to that in a reference SAW device or both. The mechanical properties of the material on the SAW device influence the correlation between mass and the velocity or amplitude of the SAW. The researchers who constructed SAW devices using thin film piezoelectric materials also exploited specific chemical detection [25]. In this case, biomolecules are immobilised on a planar surface and set into oscillatory mode by a microfabricated transmitter. An oscillatory signal is sent across the piezoelectric devices and is detected at the receiver at a known time, which is dependent on any attenuation of the transmitted signal, such as that caused by bonded DNA.

Acoustic plate mode (APM) oscillators that rely on flexure Lamb waves or shear horizontal waves have also been reported. The flexure model devices [26, 27] comprise a piezoelectric substrate, for example, zinc oxide (ZnO) on silicon (Si), that is thin enough so that the mode propagates with minimal energy loss. In contrast with SAW devices, excitation by the interdigitated electrode array induces motion in the entire substrate. Shear horizontal acoustic plate mode (SH-APM) devices use thin quartz plates without an inert support [28]. In

this case an alternating field causes particle displacement parallel to the surface and normal to the propagation direction. The mass-frequency relation for the fundamental mode is identical to that of the flexure mode devices, but operation at higher harmonics affords better sensitivity [22]. Wang et al. [29] demonstrated the utility of the APM sensor for the detection of serum-based proteins.

Recent years have seen a growth in the use of scanning force microscopy (SFM) probes as miniaturised sensors for a number of chemical detection applications e.g. [30, 31]. SFM probes are essentially microfabricated cantilevers, and for application as chemical sensors can be operated in two basic modes: static bending and resonant oscillation. In the static bending mode material is selectively adhered to one surface of the device leading to a differential surface stress. The resultant bending of the cantilever is thus a measure of the amount of deposited material. This mode of operation is ultimately the more sensitive [31]. The bending of an array of specially fabricated cantilevers has even been used to detect a single base mismatch between two oligonucleotide sequences [32]. This technique can, however, be subject to difficulties due to drift, long equilibration times and fluid turbulence [32]. The alternative mode of operation is analogous to the QCM, in that the cantilever is resonated by an externally applied signal and the resonance frequency monitored as a function of surface absorption. The resonant frequencies of SFM probes are typically a few tens of KHz, implying much simpler operation and, due to the reduced importance of hydrodynamic effects, a more straightforward interpretation. Theoretical considerations suggest that microcantilever devices have sensitivities that are competitive with other gravimetric devices such as the QCM [30], and carry the advantage of being suitable for use in liquids and having dimensions appropriate for μ TAS environments.

By design, many of these approaches can be adapted to a variety of test types. Table 1.1 shows a comparison of the most promising miniaturised sensing technologies at the moment [16].

Type of chip	Technical Principle
Microcapillary Electrophoresis	Separation of analytes by electrophoresis in a microfabricated capillary 1-30 μ m in diameter
DNA hybridation chip	Synthesis or site-directed fixation of oligonucleotide probes onto chip surface; detection by laser-induced fluorescence of hybridised PCR product
Surface acoustic wave sensor (SAW)	Detection of change in the propagation of a surface wave from transmitter to receiver through a molecular binding domain
Surface plasmon resonance (SPR)	Detection of the evanescent wave propagated from the interface of a reflecting metal to which is bound a hybridised analyte
Electromechanical MEMS sensor	Detection of mass loading, either by shift in resonant frequency or by static flex of a piezoelectric transducer
Porous silicon interferometer	Silicon is 'roughened' to increase the surface area; oligonucleotide probes are fixed to the surface; light reflected from the surface will shift in wavelength as a function of the change in the optical thickness attributable to sample binding
Artificial biomembrane sensor	A phospholipid bilayer containing a synthetic protein, e.g. gramicidin, over a gold electrode creates ionic pores that permit a current to cross the membrane; distortion of the pores because of binding of a ligand to a 'tethered' receptor decreases the ionic current, which is measured by a galvanometer

Table 1.1: Comparison of miniaturised sensing technologies by McGlennen [16].

1.3.1 Summary of Micromechanical Sensors

Detectors with resonating piezoelectric crystals used to determine the physical and mechanical changes at nanogram scale, have the advantages of low detection limit and wide working range. Although mass sensitivities obtained with piezoelectric resonators are good, the stress and thermal sensitivities are low due to their large size. In addition, there exists a limit beyond which piezoelectric resonators cannot be miniaturised. However, various authors have observed a discrepancy between the mass estimated from the frequency shift of the QCM, through the Sauerbrey equation, and the biomolecule mass loading measured by other analytical techniques [24, 33, 34].

Until now, most DNA biosensors previously reported are based on substrates which are either fiberoptic probes, glass or silica plates. These are externally connected to a photosensing system, which generally consist of a conventional detection device, such as a photomultiplier, or a charge-coupled device. Although the probes on the sampling platform are small, the entire device containing excitation laser sources and detection system (often a confocal microscope system) is relatively large, e.g. table-top size systems.

We propose a cantilever based biosensor. The resonant frequency of an oscillating cantilever $f_0 \propto \sqrt{k/m}$ depends on both the effective mass m of the loaded device and on the force constant k . Since k can change due to the surface layer absorbed onto the cantilever, care must be taken to properly account for the separate contributions to the shift in f_0 . By designing devices in which the absorption is localised to an area at the end of the cantilever, the contribution from the change in force constant can be minimised [31]. The narrow V-shaped design of commercial SFM probes are not necessarily well suited to this type of application, and specially design cantilevers are necessary, such as the paddles discussed in the following chapters.

1.4 Excitation and Detection Mechanisms in Silicon

A cantilever is a mechanical structure designed to vibrate at its resonant frequency. Micromechanical cantilevers are miniature structures with dimensions typically varying between a few microns and a centimeter. The frequency of the vibrations of the structure at resonance are extremely stable, enabling the cantilever to be used as the sensing element of a resonant sensor. In each application the behaviour of the cantilever is of fundamental importance to the performance of the device.

The properties of a cantilever sensor are modified by the material adhered to it [35]. This typically alters the stiffness, or mass of the cantilever, causing a change in its resonant frequency. The other major components of a cantilever sensor are the vibration drive and detection mechanism. The drive mechanism excites the vibrations in the structure, while the detection mechanism monitors these vibrations. The frequency of the detected vibrations forms the output of the sensor, and this signal is also fed back to the drive mechanism via an amplifier maintaining the cantilever at resonance over the entire measurand range. Fig. 1.3 shows the diagram of a typical sensing components.

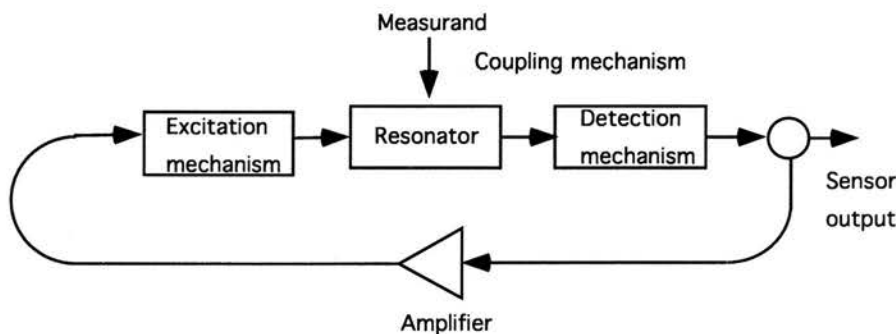


Figure 1.3: Block diagram of resonant layout showing essential device components [36].

There are many potential excitation and detection mechanisms possible in silicon. Many of these mechanisms can be used both to excite and to detect a cantilever vibration, either simultaneously or in conjunction with another mechanism [37]. The mechanisms best suited

for driving or detecting depend on a number of factors. These include the drive forces generated, the coupling factor, sensitivity of the detection mechanism, the effects of the chosen mechanism on the performance and behaviour of the cantilever, and practical considerations related with the fabrication of the cantilever and the sensor's final environment [38, 36].

1.4.1 Electrostatic Excitation

The electrostatic excitation of a resonator relies upon electrostatic forces between two electrodes. These electrodes can either be separated by an air gap, with one electrode being located on the cantilever and the other one on the surrounding structure, or by a three layer sandwich, consisting of two electrodes separated by a dielectric layer. The associated vibration detection mechanism relies on the change of capacitance between the electrodes as the cantilever deflects.

A useful analysis of the relationship of applied drive voltage and deflection in a micromachined cantilever was worked out by Petersen [39]. From his work it was deduced that the normalised load versus the normalised deflection shows a nonlinearity between the cantilever deflection and applied voltage. It was also demonstrated that once the voltage produced by deflection exceeds a threshold, the position of the cantilever is unstable, and the beam spontaneously deflects all the way down. This makes electrostatic actuation rather unsuitable.

1.4.2 Magnetic Excitation

The force resulting from the interaction between a magnetic particle placed on the structure and a magnetic field has been used for resonator excitation [40]. Applying an alternating current to the resonator results in alternating forces, and hence vibrations are induced in the resonator. A magnetically driven system allows high performance actuation within a variety

of environments.

1.4.3 Thermal Excitation

A current passing through a patterned resistor located on the surface of the cantilever creates a temperature gradient across the cantilever's thickness, with the top surface at a higher temperature than the bottom. The induced thermal expansion of the material results in a bending moment on the cantilever, deforming the structure. By modulating the current through the resistor vibrations can thus be created.

This approach will result in localised periodic heating and a rise in the temperature of the cantilever as a whole. None of these heating effects are desirable. Nevertheless, electrothermal excitation is widely used and can be found in different resonant devices [41, 42].

The thermal drive technique described previously can also be achieved using the heating effect resulting from a light source incident on the cantilever. A modulated light source will induce a periodic thermal expansion on the surface of the cantilever, inducing vibration in the structure. This method can conveniently be combined with optical detection techniques.

Optical excitation techniques are attractive since no integrated vibration mechanism is required. Optothermal techniques are immune to electromagnetic interference and their use with passive resonators can allow cantilevers to be used in harsh environments. However, the accurate integration and alignment of the optical system onto the cantilever is difficult to achieve.

1.4.4 Piezoelectric Excitation and Detection

This approach uses a deposited layer of piezoelectric material both to excite and detect the resonator's vibrations [43]. The piezoelectric material, typically zinc oxide (ZnO), is formed in a sandwich between two electrodes, creating a piezoelectric bimorph. An oscillating voltage on the bimorph causes a periodic deformation, exciting the cantilever. Detection is provided by the corresponding potential generated by the deformation of the bimorph.

Due to the very strong piezoelectric coupling efficiency of the ZnO, it is a very attractive material for excitation and detection of the vibrational motion of a cantilever. Nevertheless, the high d.c. conductivity preventing the build-up of an electric field means that special configurations are needed at low frequencies, complicating the fabrication process and making the composite resonator more susceptible to temperature fluctuations as a result of differential thermal expansion effects [44]. Furthermore, ZnO is not an IC-compatible material and therefore especial precautions need to be taken.

1.4.5 Optical Detection

There are several techniques for monitoring the vibrations of a cantilever using optical detection, such as intensity modulation by means of a shutter controlled by the resonator [45], use of an optical proximity or displacement sensor [46], or interferometric techniques [47, 48].

The interferometric techniques rely on two interfering reflections, one from a fixed arm and the other from the vibrating cantilever. The combination of the reflected light results in interference fringes, which give a direct measure of the amplitude of the displacement.

In intensity modulation techniques, the intensity of the reflected light varies as a function of the amplitude of the cantilever vibrations.

There are some disadvantages inherent to the optical detection techniques. On one

hand, the cantilever needs to be coated with a reflecting material in order to reflect back the beam from the cantilever to the photodiode. This problem can be avoided using optical fibre systems. However, the accurate integration of the optical fibre onto the sensor chip is difficult to achieve. On the other hand, depending on the environment the laser beam possibly has to pass several interfaces and different media, which can cause significant loss of intensity. The laser probe can also cause an important heating of the cantilever and induce unwanted bending due to the temperature gradient.

1.4.6 Piezoresistive Detection

Piezoresistive detection in silicon is very attractive from a technological point of view, since it uses the inherent piezoresistive nature of silicon. Standard IC processing technologies can be used to fabricate the resistors, either by diffusing or implanting them or by depositing polysilicon resistors on the top surface of the cantilever. The value of the resistor will change sinusoidally with the vibration of the cantilever. The frequency change of the changing resistance forms the output of the sensor and hence, the actual value of the resistance and the behaviour of the resistor becomes largely unimportant. Furthermore, the resistor only needs to be connected in a Wheatstone bridge circuit to read the output.

This approach is simple to achieve and is widely used in many resonant sensors [42] and can easily be used with other excitation techniques.

1.4.7 Capacitive Detection

Capacitive detection is based on the fact that an a.c. current will flow through a d.c. biased capacitor if the distance between the capacitor plates, and therefore the capacitance, fluctuates. This scheme is very attractive from the technological point of view as it is relatively easy to fabricate [49, 50, 51]. However, if the electrical feedthrough and/or parasitic

loads are too large, these effects will mask the detection signal of the cantilever. To overcome this problem, an on-chip buffering and amplification is used, along with a polarised d.c. voltage for proper operation. This voltage will reduce the dynamic stiffness of the structure and will therefore result in a lowering of the resonance frequency [52].

1.5 Conclusions

There is an impending need for novel actuators and sensors to be used in μ TAS context, since it will both reduce cost of diagnosis and increase throughput.

With the current technology two major disadvantages are encountered. On the one hand, until very recently, most methods in the biochemical analysis field are concerned with end-point determination. On the other hand, dyes and fluorescent labels directly attached to the analytes are widely used to activate specific chemical reactions. These dyes not only modify the analytes, but can also denaturalise them.

Different MEMS sensors have up to date already been used as biochips. Examples of proven utility are the QCM, SAW or APM. Nevertheless, the frequency of these acoustic devices is typically of the order of several hundreds of MHz, which requires sophisticated electronics. The sensing area of such devices is macroscopic, comprising a few mm^2 up to cm^2 in order to achieve measurable frequency shifts and to avoid problems in densely packed resonating systems. Furthermore, viscoelasticity and acoustic coupling effects can cause significant difficulties in data interpretation for measurements under liquids and response is complicated in a complex way to mass changes under solution in general.

It is therefore tempting to use oscillating cantilevers similarly to QCM devices, i.e., to monitor the analytes on a cantilever by following the change of its resonant frequency. One of the advantages in using cantilevers is the simplification of the electronics and experimental

arrangement, since they operate at lower frequencies of the order of a few KHz. Such a small and simple setup is of high interest for practical applications as well as for economic reasons.

A crucial point in the case of dynamic monitoring of reactions is the driving mechanism required to oscillate the cantilever. Cantilevers are most commonly driven acoustically or thermally. Nevertheless, acoustically driven cantilevers have several modes excited at once. If the driving force is directly applied to the cantilever a single mode can be excited. This can be achieved by applying a magnetic field to a magnetic coating or a magnetic particle fixed at the end of the cantilever. Such magnetically driven cantilevers display several advantages compared to other driving mechanisms. The response of the cantilever is simpler, and there is a substantial improvement of the signal-to-noise ratio for operation in a dynamic mode.

Another important point is the sensing mechanism. Optical detection is predominantly used to detect cantilever deflection. There are some inherent disadvantages to the optical detection. Piezoresistors are an alternative sensing technique which do not show the drawbacks of the optical detection system. Having piezoresistors incorporated in the cantilevers legs, the whole device can be operated in a complete opaque environment or in diffuse scattering liquids. Due to its small dimensions it could also be integrated into a larger system.

References

- [1] A. Robinson, *Clin. Microbiol. Rev.*, **7**, 185-199, (1994).
- [2] E.I. Bluth, *et al.*, *Arch. Internal Med.*, **152**, 837-840, (1992).
- [3] M. Madou and M.J. Tierney, *Appl. Biochem. Biotechnol.*, **41**, 109-128, 91993).
- [4] K.D. Wise and K. Najafi, *Science*, **254**, 1335-1342, (1991).
- [5] P. Wilding, *et al.*, *Clin. Chem.*, **40**, 43-47, (1994).
- [6] K.A. Erickson and P. Wilding, *Clin. Chem.*, **39**, 283-287, (1993).
- [7] A.T. Woolley and R.A. Mathies, *Proc. Natl. Acad. Sci. USA*, **91**, 11348-11352, (1994).
- [8] D.J. Harrison, *et al.*, *Science*, **261**, 895-897, (1993).
- [9] S. Shoji and M. Esashi, *Appl. Biochem. Biotechnol.*, **41**, 21-34, (1993).
- [10] R.F. ReferencesService, *Science*, **268**, 26-27, (1995).
- [11] P. Bergveld, *et al.*, *Micro Total Analysis Systems*. Kluwer, Dordrecht, The Netherlands, (1994).
- [12] J. Branbjerg, *et al.*, *Proc. 9th IEEE Icro Electro Mechanical Systems Workshop (San Diego)*, 441, (1996).
- [13] L. Stryers, *Biochemistry*, W.H. Freeman and Company, New York (1995).

- [14] C.T. Wittwer, *et al.*, *Bio Techniques*, **22**, 176, (1997).
- [15] M. Malmqvist, *Nanofabrication and Biosystems*, H.C. Hoch, L.W. Jelinski and H.G. Craighead, Cambridge University Press (1996).
- [16] R.C. McGlennen, *Clin. Chem.*, **47:3**, 393-402, (2001).
- [17] C. Henke, DNA-chip technologies. Part 3. What does the future hold? *IVD Technology.*, **7**, 37-42, (1999).
- [18] T. Thundat, *et al.*, Microcantilever Sensors [Review], *microscale Thermophys. Eng.*, **1**, 185-199, (1997).
- [19] H.L. Tuller, *et al.*, Inorganic sensors utilizing MEMS and microelectronic technologies. *Curr. Opin. Solid State Mater Sci.*, **3**, 501-504, (1998).
- [20] J.W. Grate, *et al.*, *Anal. Chem.*, **65**, 940A, (1993).
- [21] J.W. Grate, *et al.*, *Anal. Chem.*, **65**, 987A, (1993).
- [22] M. D. Ward and D.A. Buttry, *Science*, **249**, 1000, (1990).
- [23] G. Sauerbrey, *Z. Phys.*, **155**, 206, (1959).
- [24] K. Bizet, *et al.*, *Biosensors and Bioelec.*, **13**, 259-269, (1998).
- [25] J. Zhai, *et al.*, *Biotechn. Adv.*, **15**, 43-58, (1997).
- [26] S.W. Wenzel and R. White, *IEEE Trans. Electron. Dev.*, **35**, 735, (1988).
- [27] S.W. Wenzel, *Appl. Phys. Lett.*, **54**, 1976, (1989).
- [28] A.J. Ricco, *et al.*, *ACS Symp. Ser.*, **403**, 191, (1989).
- [29] A.W. Wang, *et al.*, *Trans. 97, 7th Internat. Conf. on Solid-state Sens. and Actu.*, 191-194, IEEE 97.

- [30] P.G. Datskos and I. Sauers, 'Detection of 2-mercaptoethanol Using Gold-Coated Micro-machined Cantilevers', *Sensors and Actuators B*, **61**, 75-82, (1999).
- [31] G.Y. Chen *et al.*, 'Adsorption-Induced Surface Stress and Its Effects on resonance Frequency of Microcantilevers', *J. Appl. Phys.* **77**(8), 3618-3622, (1995).
- [32] J. Fritz *et al.*, 'Translating Biomolecular Recognition Into Nanomechanics', *Science*, **288**, 316-318, (2000).
- [33] N. Geddes, *et al.*, *Sens. Actuators B*, **17**, 125-131, (1994).
- [34] M. Muratsugu, *et al.*, *Anal. Chem.*, **65**, 2933-2937, (1993).
- [35] R.M. Langdon, 'Resonator Sensors—a review', *J. Phys. E. Sci. Instrum.*, **18**, 103-115. (1985).
- [36] S.P. Beeby, and M.J. Tudor, 'Micromechanical Devices and Fabrication', *Enciclop. of Elect. and Electro. Eng.*, Wiley and Sons, **12**, 665-676, (1999).
- [37] H.A.C. Tlmans, *et al.*, 'Single Element Excitation and Detection Mechanisms for Micromechanical Resonators', *Tech. Digest of the Int. Conf. on Solid-State Sensors and Actuators (Transducers '91)*, 533-537, (1991).
- [38] A. Prak, *et al.*, *Review of Excitation and Detection Mechanisms for Micromechanical Resonators, Sensors and Materials*, **5** (3), 143-181, (1993).
- [39] K.E. Petersen, 'Dynamic Micromechanics on Silicon: Techniques and Devices', *IEEE Trans. on Electron Devices*, **25**, (10), 1241-1250, (1978).
- [40] J. A. Sidles *et al.*, 'Magnetic Resonance Force Microscopy', *Rev. Mod. Phys.* **67**, (1), (January 1995).
- [41] T.S.J. Lammerink, *et al.*, 'Performance of thermally Excited Resonators', *Sensors and Actuators A*, **21-23**, 352-356, (1990).

- [42] M.B. Othman and A. Brunnschweiler, 'Electrothermally Excited Silicon Beam Mechanical Resonator', *Electron. Lett.*, **23**, 728-730, (1987).
- [43] T. Fabula, *et al.*, 'Triple Beam Resonant Silicon Force Sensor Based Piezoelectric Thin Films', *Sensors and Actuators A*, **41-42**, 375-380, (1994).
- [44] F.R. Blom, *et al.*, 'Thin Film ZnO as Micromechanical Actuator at Low Frequencies', *Sensors and Actuators A*, **21-23**, 226-228, (1990).
- [45] T.S.J. Lammerink and S.J. Gerritsen, 'Fibre Optic Sensor Based on Resonating Mechanical Structures', *SPIE*, **798**, 67-71, (1987).
- [46] J.G. Smits, *et al.*, 'Frequency Dependence of Resonant Diaphragm Pressure Sensor', *Proc. 3rd Int. Conf. Solid-State Sensors and Actuators, (Transducers '85)*, Philadelphia, USA, 93-96, (1985).
- [47] M.J. Tudor, *et al.*, 'Silicon Resonator Sensors: interrogation Techniques and Characteristics', *IEEE Proc.*, **135**, D:364-368, (1998).
- [48] K.E.B. Thornton, *et al.*, 'A Sensitive Optically Excited Resonator Pressure Sensor', *Sensors and Actuators A*, **24**, 15-19, (1990).
- [49] R.T. Howe and R.S. Muller, 'Resonant Microbridge Vapor Sensor', *IEEE Trans. on Electron Devices*, **33**, 499-506, (1986).
- [50] M.W. Putty, *et al.*, 'One Port Active Polysilicon Resonant Microstructures', *Proc. Micro. Electro. Mechanical Systems (MEMS 89)*, 60-65, (1989).
- [51] C. Linder, *et al.*, 'Capacitive Polysilicon Resonator with MOS Detection Circuit', *Sensors and Actuators A*, **25-27**, 591-595, (1991).
- [52] H.C. Nathanson, *et al.*, 'The Resonant Gate Transistor', *IEEE Trans. Electron. Devices*, **14**, 117-133, (1967).

Chapter 2

Cantilevers Design Criteria and Selection

2.1 Introduction

The cantilevers should meet some criteria in order to achieve a maximum sensitivity. For a resonating cantilever to work with high sensitivity needs a low force constant, high resonant frequency, high lateral stiffness and high mechanical quality factor Q .

At low frequencies the effects of thermal drift are more pronounced. Furthermore, as the ultimate aim for these cantilevers is to use them in a liquid, which due to its high density will reduce the natural frequency, a relatively high frequency is desirable.

The cantilevers must possess high lateral stiffness so that they cannot move in the transverse direction. All the strain will then be flexural and there will only be normal modes.

The resolution of a frequency output is mainly determined by the mechanical quality factor. The higher the quality factor, the sharper the resonance peak, and thus the higher the resolution of the frequency output.

These criteria are studied in this chapter with the aim to determine the optimal features of the cantilever for its best performance.

2.2 Geometrical Design

In the past, the piezoresistive cantilevers used in the literature were usually designed with two parallel legs [1, 2] or even by a single beam [3, 4]. In order to improve the stability of the cantilevers and to prevent it from swinging laterally and/or torsionally during measurements in dense surroundings a V-shaped cantilever paddle is used [5]. As described in chapter 3 this will also have an effect on the frequencies of the normal modes, making them more difficult to mix. Depending on the angle, the lateral stiffness will change, the bigger the angle the higher the lateral stiffness, but at the same time, sensitivity in the device is lost when increasing the angle of the arm, as the piezoresistive coefficient decreases (see Section 2.5.2).

As will be demonstrated later in this chapter, the width of the legs should be as small as possible, but always wide enough to integrate the strain gauge resistor at the root of the cantilever. The thickness of the cantilever is fixed in the process, as it is determined by the type of wafer being used. Therefore, the only remaining parameter is the length of the cantilever paddle.

2.3 Mechanical Properties of the Cantilevers

The resonant frequency and the force constant affects the response of the cantilevers. Both are defined by the mechanical properties of the material, the geometry of the cantilever and the forces exerted on them. V-shaped cantilevers have usually been treated as two rectangular beams in parallel to estimate their mechanical properties [6], but this only leads to an approximate solution.

The force constant of a V-shaped microcantilever paddle is derived from basic mechanics theory. The maximum deflection of the cantilever is determined from the differential equation which describes the deflection. Once the maximum deflection is known the force constant can be determined by definition. These calculations assume that there is no lateral twist, *i.e.* that the cantilever only bends in the direction of the force. This approximation is the so called zeroth order approximation [7], which can be applied since the width is far smaller in magnitude than the length.

2.3.1 Force Constant of a V-shaped Microcantilever Paddle

Based on basic mechanics theory [8], the differential equation of a cantilever beam under a single force at the free end is given in Appendix A.1 (Eq. A.1) as:

$$EI_z \frac{d^2y}{dx^2} = Fx \quad (2.1)$$

with the following boundary conditions (see Fig. 2.1):

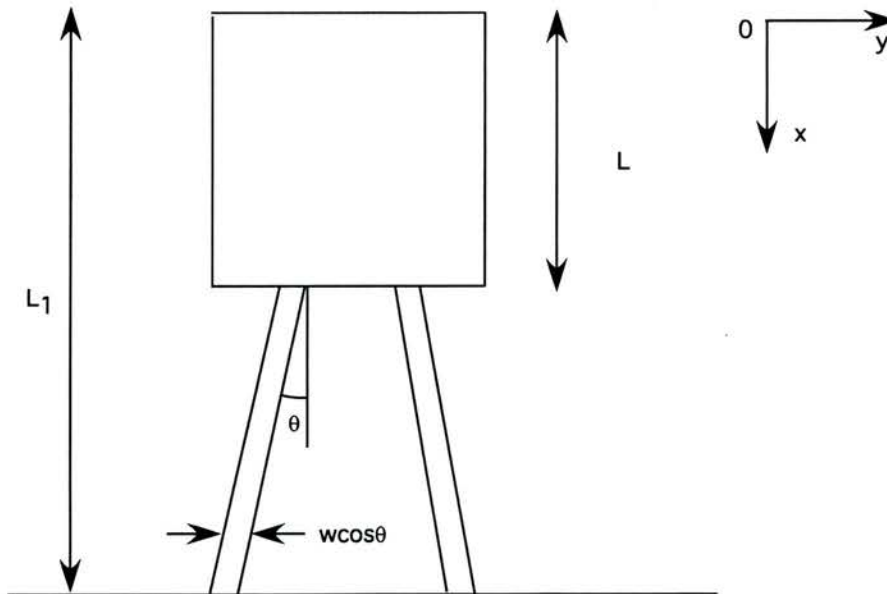


Figure 2.1: A sketch of the cantilever paddle.

$$\begin{aligned} x = L_1, \quad \frac{dy}{dz} &= 0 \\ x = L_1, \quad y &= 0 \end{aligned} \tag{2.2}$$

where E is the Young's modulus; I_z the second moment of area with respect to the neutral axis Z ; L_1 the total length of the cantilever paddle and F a single force at the end of the cantilever. A V-shaped cantilever paddle structure is shown in Fig. 2.1.

The second moment of area of the cantilever is defined by,

$$I_z = \int_{-\frac{t}{2}}^{\frac{t}{2}} \left[\int_{-\frac{w}{2}}^{\frac{w}{2}} y^2 dy \right] dz. \tag{2.3}$$

This integral should be solved for the two different geometries, when x goes from 0 to L (square paddle), and for when x goes from L to L_1 (cantilever legs). Therefore we have,

$$I_z = \begin{cases} \frac{1}{12}Lt^3, & x \in (0, L) \\ \frac{1}{6}\omega t^3, & x \in (L, L_1) \end{cases} \tag{2.4}$$

where L , t , and ω , are the size of the paddle, the thickness and the width of the cantilever respectively.

Therefore, Eq. A.1, is also solved considering these two regions. The maximum end deflection of the cantilever paddle under a single force at the free end of the cantilever is then given by Eq. 2.5, the detailed derivation can be found in Appendix A.1,

$$y(0) = \frac{2F(2\omega L^2 + L_1^3 - L^3)}{\omega Et^3}. \tag{2.5}$$

Now, by definition,

$$K = \frac{F}{y(0)} \quad (2.6)$$

Therefore, the force constant k is given by Eq. 2.7,

$$K = \frac{Et^3\omega}{2(L_1^3 - L^3 + 2\omega L^2)} \quad (2.7)$$

From this it can be seen how the force constant depends on the cube of the thickness and on the width of the arms. Furthermore, it is inversely proportional to the cube of the length of the cantilever and the paddle. Therefore, the longer and thinner the cantilever, the smaller the spring constant and therefore the more sensitivity the devices will have. Nevertheless, it should be highlighted that the longer the cantilever the heavier it will become, and therefore the relative change $\Delta m/m$ is smaller. Hence, it is needed to achieve a compromise between all the different parameters defining the sensitivity of the cantilevers.

2.4 Natural Frequencies

A mechanical wave may be defined as the propagation of a physical quantity (e.g. energy or strain) through a medium (solid or fluid) without the net movement of the medium. The form of wave will depend upon the nature of its source and the material through which it travels. The speed of a wave in a solid depends upon the mechanical properties of the material, and its wavelength is a function of the frequency of the wave source.

When studying the phenomena of natural frequencies, reflection of a mechanical wave at a system boundary becomes important. If the reflected wave coincides exactly with the incoming wave, then a standing wave is created. The superposition of these waves results in the amplitude of each wave combining to become twice that of the initial wave, assuming

perfect reflection. The standing wave phenomena will occur at specific frequencies known as the natural, or mode, frequencies. In the case of a string, for each natural frequency there will be a characteristic distorted form, or mode shape as shown in Fig. 2.2.

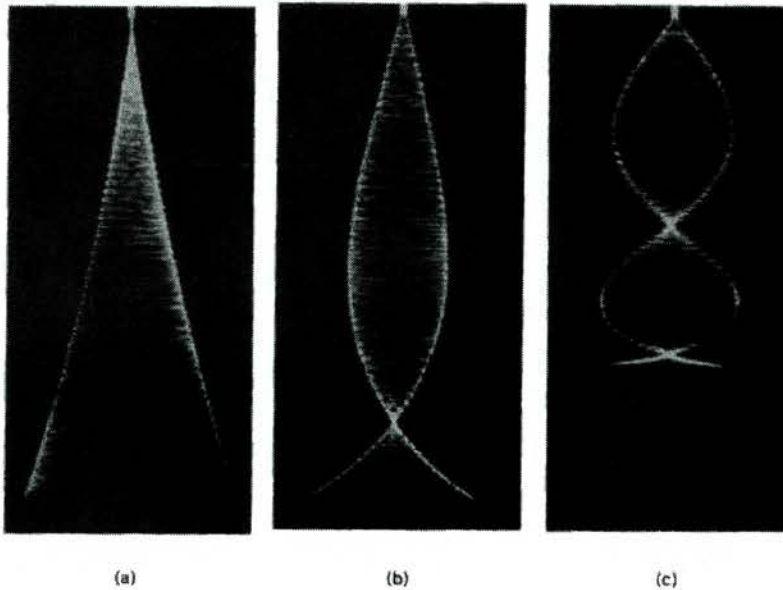


Figure 2.2: First three normal modes of vertical string with upper end fixed [9].

Points of zero displacements are called nodes, and the points of maximum displacements as known as antinodes.

2.4.1 Harmonic Oscillation Theory

The cantilever can be treated as a one dimensional oscillator. Therefore the equation which describes the motion of a cantilever with damping in the system and actuated by an external force, will be that of a forced damped oscillator Eq. 2.8. The most striking feature of a driven oscillator is the way in which a periodic force of a fixed size produces very different results depending on its frequency. In particular, if the driving frequency is made close to the natural frequency, then the amplitude of oscillation can be made very large by repeated applications

of a quite small force. This is the phenomenon of resonance. A force of about the same size at frequencies well above or well below the resonant frequency is much less effective; the amplitude produced by it remains quite small. It is typical of this type of motion that the driven system is compelled to accept whatever frequency the driving force has. Its tendency to vibrate at its natural frequency may be in evidence at first, but ultimately gives way to the external influence. These are the so called, transient and steady state motions and are described by,

$$m \frac{d^2 z}{dt^2} = -kz - b \frac{dz}{dt} + F_0 \cos \omega t. \quad (2.8)$$

Before trying to solve and interpret Eq. 2.8, it would be helpful to understand the problem when no damping is in the system. In this case the motion equation becomes Eq. 2.9.

$$m \frac{d^2 z}{dt^2} = -kz + F_0 \cos \omega t. \quad (2.9)$$

Or written in complex notation,

$$m \frac{d^2 z}{dt^2} + kz = F_0 e^{j\omega t} \quad (2.10)$$

Assuming that the motion is harmonic, and that the natural oscillations of the system are not present (*i.e.* steady state solution), the solution can be of the form,

$$z = A e^{j\omega t + \alpha}. \quad (2.11)$$

Differentiating Eq. 2.11 twice with respect to t , and substituting in Eq. 2.10, gives,

$$(-m\omega^2 A + kA) e^{j\omega t + \alpha} = F_0 e^{j\omega t} \quad (2.12)$$

which can also be written as,

$$\begin{aligned}(\omega_0^2 - \omega^2)A &= \frac{F_0}{m}e^{-j\alpha} \\ &= \frac{F_0}{m}\cos\alpha - j\frac{F_0}{m}\sin\alpha\end{aligned}\quad (2.13)$$

This contains two conditions corresponding to the real and the imaginary parts on the two sides of the equation,

$$\begin{aligned}(\omega_0^2 - \omega^2)A &= \frac{F_0}{m}\cos\alpha \\ 0 &= -\frac{F_0}{m}\sin\alpha\end{aligned}\quad (2.14)$$

These two equations shows a dependence which is shown graphically in Fig. 2.3

The amplitude, A, switches abruptly from large positive to large negative value as ω passes through ω_0 . The resonance phenomenon itself is represented by the result that the magnitude of A, without regard to sign, becomes infinitely large at $\omega = \omega_0$ exactly. It can also be deduced that α can only be either 0, or π , with the discontinuous jump at $\omega = \omega_0$.

The result of a system like the one described but with damping shall now be considered . In this case if we rewrite Eq. 2.8 changing the notation to complex, the it becomes,

$$\frac{d^2z}{dt^2} + \gamma\frac{dz}{dt} + \omega_0^2z = \frac{F_0}{m}e^{j\omega t}\quad (2.15)$$

where γ is b/m , the reciprocal of the time required for the energy to decrease to $1/e$ of its initial value.

Now, assuming the following solution,

$$z = Ae^{\omega t - \delta}\quad (2.16)$$

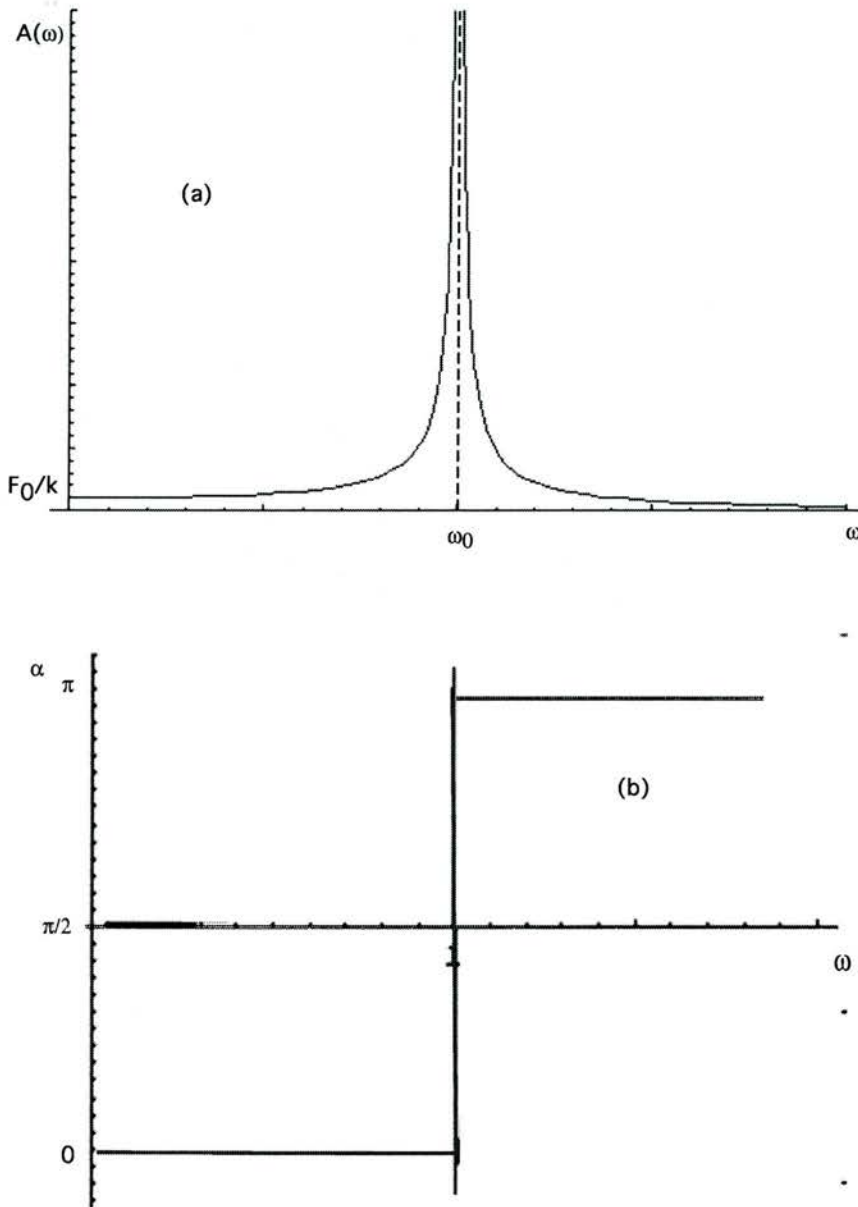


Figure 2.3: (a) Absolute amplitude of forced oscillations as a function of the driving frequency, for zero damping. (b) Phase lag of the displacement with respect to the driving force as a function of frequency.

where δ is a positive phase angle by which the driving force leads the displacement. Solving Eq. 2.15 in the same way as for the previous case, the following conditions can be obtained,

$$\begin{aligned}(\omega_0^2 - \omega^2)A &= \frac{F_0}{m} \cos \delta \\ \gamma\omega A &= -\frac{F_0}{m} \sin \delta\end{aligned}\tag{2.17}$$

Therefore,

$$\begin{aligned}A(\omega) &= \frac{\frac{F_0}{m}}{[(\omega_0^2 - \omega^2)^2 + (\gamma\omega)^2]^{\frac{1}{2}}} \\ \tan \delta(\omega) &= \frac{\gamma\omega}{\omega_0^2 - \omega^2}\end{aligned}\tag{2.18}$$

The interpretation of which is the same as before, as it is shown in Fig. 2.4. These curves have a clear resemblance to those in Fig. 2.3 for the undamped oscillator. As can be seen for $\tan \delta$ in Eq. 2.18, the phase lag increases continuously from zero (at $\omega = 0$) to 180° (in the limit $\omega \rightarrow \infty$); it passes through 90° at precisely ω_0 . Less obvious is the fact that the maximum amplitude is attained at a frequency ω_n somewhat less than ω_0 . However, in most cases the difference between ω_m and ω_0 is negligible.

2.4.1.1 Effect of Varying the Damping Term

From the foregoing analysis, it is clear that the damped oscillator is characterised by two parameters, ω_0 and γ . It is useful to define a parameter called the quality factor (Q -factor) which is given by,

$$Q = 2\pi \left(\frac{\text{maximum stored energy}}{\text{energy lost per cycle}} \right).\tag{2.19}$$

Substituting the maximum stored energy, which is the elastic potential energy, and the

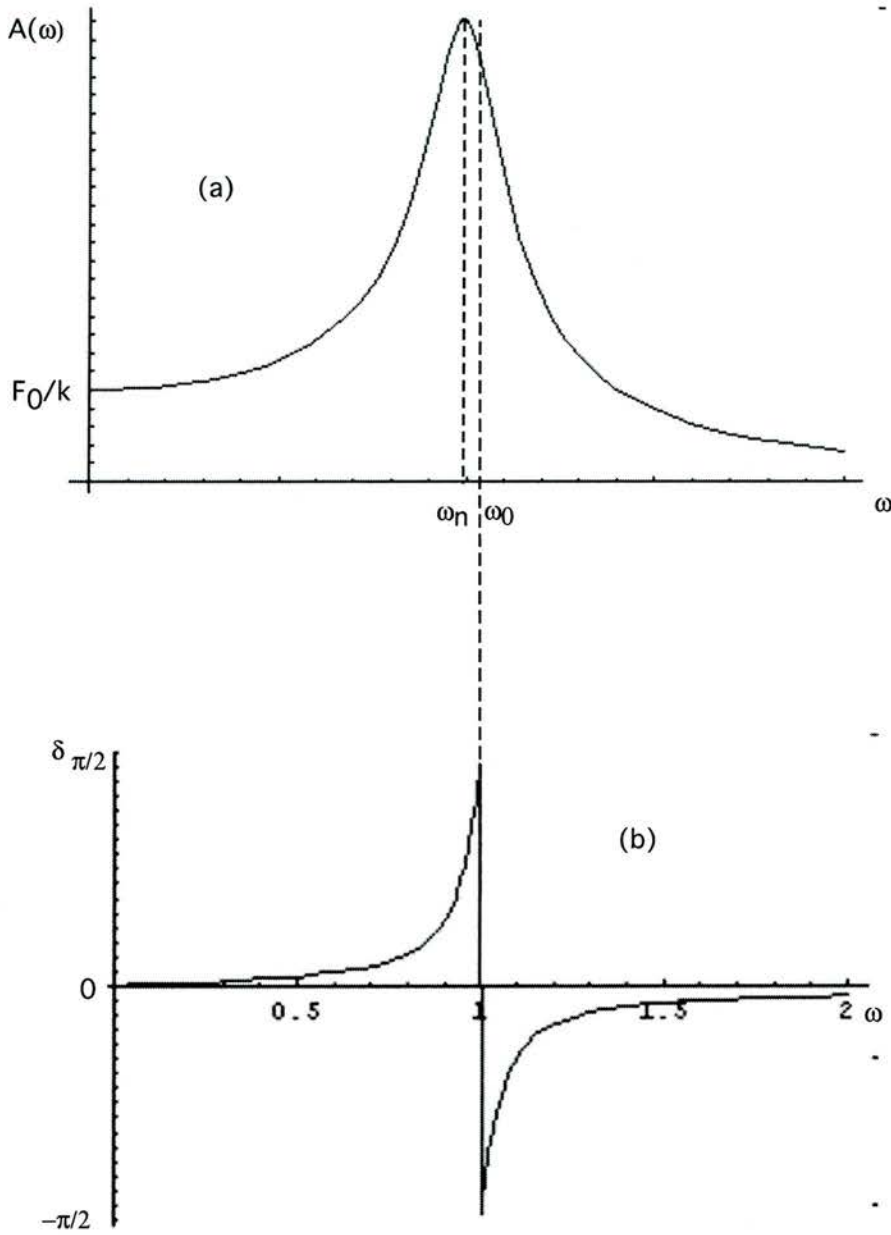


Figure 2.4: (a) Dependence of amplitude upon driving frequency for forced oscillations with damping. (b) Phase of displacement with respect to driving force as function of the driving frequency.

energy lost per cycle, which is the dissipated energy, in terms of frequency and displacement, the Q factor can be also described as $Q = \omega_0 / \gamma$. The larger the value of Q , the less the dissipative effect. Therefore, studying the dependence of the system on damping is equivalent to determining the Q dependence. The Eq. 2.18 can then be rewritten in terms of Q and using the ratio ω/ω_0 as a variable,

$$\begin{aligned} A &= \frac{F_0}{m\omega_0^2} \frac{\frac{\omega_0}{\omega}}{\left[\left(\frac{\omega_0}{\omega} - \frac{\omega}{\omega_0}\right)^2 + \frac{1}{Q^2}\right]^{\frac{1}{2}}} \\ \tan \delta &= \frac{\frac{1}{Q}}{\frac{\omega_0}{\omega} - \frac{\omega}{\omega_0}} \end{aligned} \quad (2.20)$$

The Q -factor is particularly useful since it can be directly related to the width of the resonance curve, via $Q \omega_0 / \Delta\omega$. To illustrate this we plot the curves in Fig. 2.5, which represent the Eq. 2.20 and shows the variations with frequency of amplitude and phase for different values of Q . Most of the change of δ takes place over a range of frequencies from $\omega_0(1 - 1/Q)$ to $\omega_0(1 + 1/Q)$, *i.e.* in a band width $2\omega_0/Q$ centred in ω_0 . In the limit $Q \rightarrow \infty$ the phase lag jumps from zero to π at ω_0 , *i.e.* no damping.

The amplitude has a maximum for any value of Q greater than $1/\sqrt{2}$, *i.e.* for all values of Q except for the most heavily damped systems. This maximum amplitude A_n occurs, as mentioned before, at a frequency ω_n which is less than ω_0 . Fig. 2.5 demonstrates how the sharpness of tuning of a resonant system varies with Q , which shows the importance of this parameter.

2.4.1.2 Frequency Shift

As it is explained in the previous section, even if the resonant frequency is somewhat less than ω_0 in most cases the difference is negligible. Therefore, from solving Eq. 2.9 in the case of free vibration, the resonant frequency of an oscillating cantilever can be expressed as

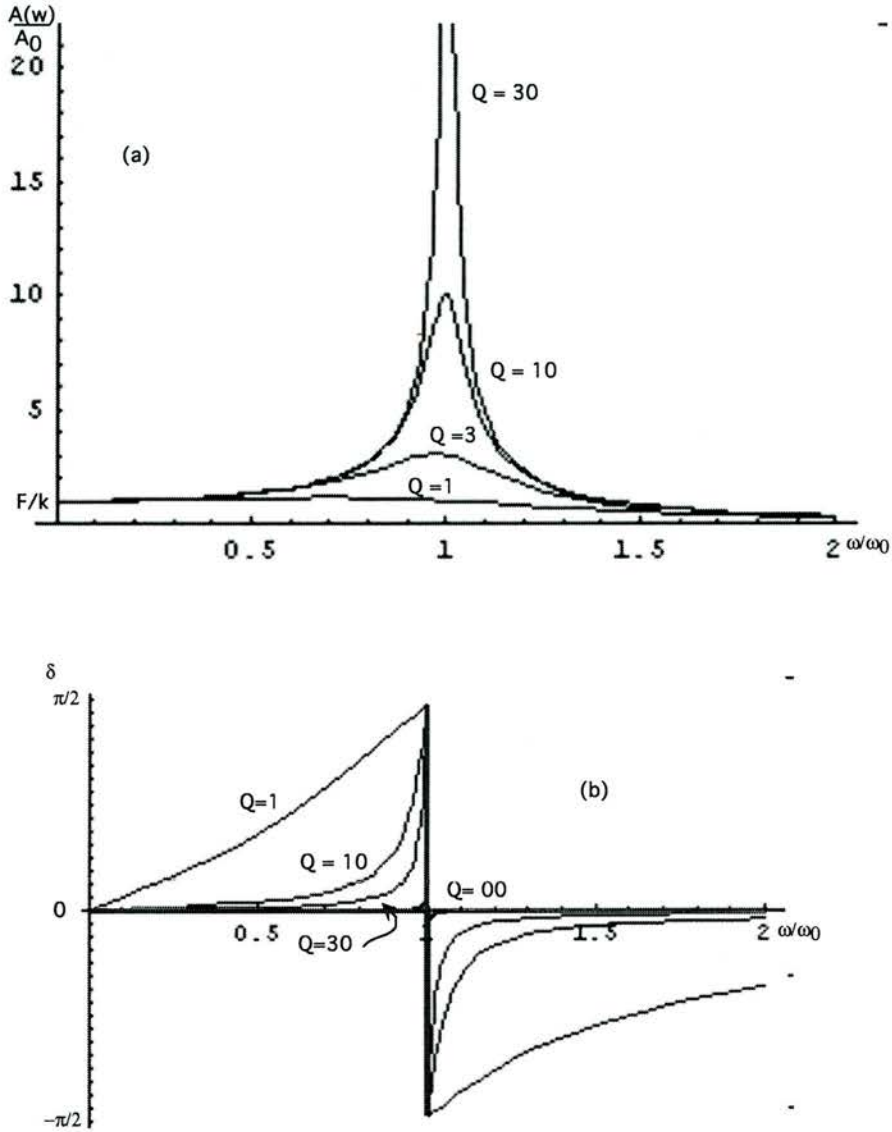


Figure 2.5: (a) Amplitude as function of driving frequency for different values of Q , assuming driving force of constant magnitude but variable frequency. (b) Phase difference δ as function of driving frequency for different values of Q .

$$\omega_0 = n\sqrt{\frac{k}{m}}, \quad (2.21)$$

where n is the modification factor needed to represent the specific geometry of the cantilever in used, which for a v-shaped cantilever with a paddle at the end, $n=1.412$.

When mass is uniformly added on the cantilever paddle surface, the resultant frequency change can be expressed as

$$\omega_1 = n\sqrt{\frac{k}{m + \delta m}}, \quad (2.22)$$

where δm is the mass change. This interpretation of frequency shift assumes that changes in spring constant, δk , are negligible since the mass is added on the paddle.

When changes in mass are very small, the resonant frequency after the mass has been added can be approximated by,

$$\omega_1 = \omega_0\left(1 - \frac{1}{2} \frac{\delta m}{m}\right) \quad (2.23)$$

which can be rewritten as,

$$\frac{\Delta\omega}{\omega_0} = -\frac{1}{2} \frac{\delta m}{m} \quad (2.24)$$

Eq. 2.24 is only valid as long as $\delta m \ll m$. This shows that the frequency shift over this limited range is linear.

2.4.2 Q Factor

As explained before, the point of maximum amplitude is at the resonant frequency, therefore as a structure approaches the resonance frequency, the amplitude of vibration will increase. This maximum will always be limited by the surroundings, *i.e.* the damping. These damping effects need to be minimised, to maximise the amplitude of the resonance frequency.

The Quality Factor (Q -factor) represents the amount of damping present in a system. It is defined as the ratio of the total energy stored in the system to the energy lost per cycle due to damping effects, as described in Eq. 2.25. Assuming there is no driving force for the system, the amplitude of the oscillations will eventually reduce to zero. The higher the Q -factor, the less the damping effects, and therefore the longer the oscillations will last.

$$Q = 2\pi \left(\frac{\text{maximum stored energy}}{\text{energy lost per cycle}} \right) \quad (2.25)$$

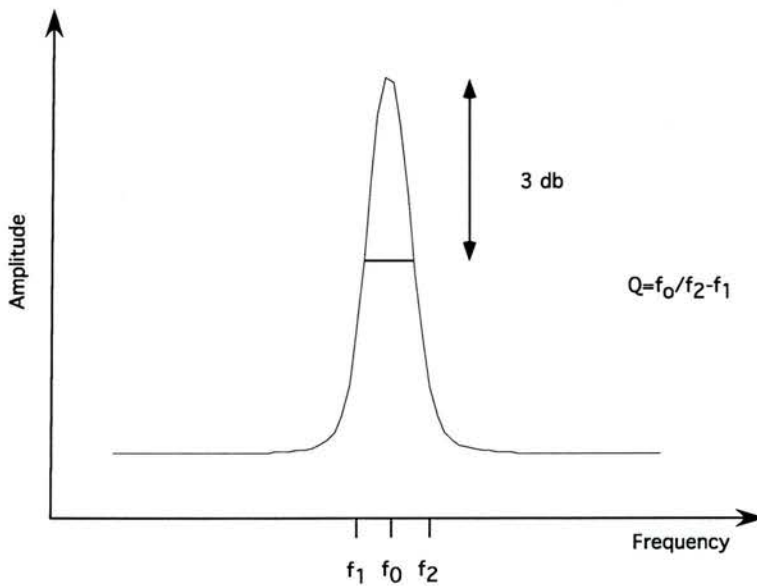


Figure 2.6: Typical amplitude frequency relationship.

As can be seen in Fig. 2.6 a high Q -factor represents a well defined and sharp resonance, which is easily distinguishable from the non-resonant vibrations. The sharper the resonance

amplitude, the easier it becomes to define the resonant frequency, and the more sensitive the sensor will become. It will also simplify the electronics since the signal to noise ratio will be greater. A high Q -factor means that little energy is required to maintain the resonance at a constant amplitude, therefore weaker driving mechanism techniques can be used. Nevertheless, if the Q -factor would be too high, it could introduce problems.

The Q -factor can also be calculated from Fig. 2.6 using Eq. 2.26.

$$Q = \frac{f_0}{\Delta f} \quad (2.26)$$

where the resonant frequency f_0 corresponds to the maximum amplitude, A_{max} , and Δf is the difference between frequencies f_1 and f_2 . Frequencies f_1 and f_2 are measured at points where the amplitude of vibration at which the stored energy within the resonator is equal to half the energy stored at A_{max} . In other words, f_1 and f_2 are found at the amplitude of $A_{max}/\sqrt{2}$ or 3dB lower than A_{max} .

From Eq. 2.25 it is clear that the Q -factor depends upon various mechanisms by which the resonator loses energy. These mechanisms arise mainly from three sources, [10].

1. The energy lost to the surroundings ($1/Q_a$).
2. The energy lost through the support of the resonator ($1/Q_s$).
3. The energy dissipated internally within the material ($1/Q_i$).

Minimising these effects will maximise the Q -factor, Eq. 2.27, [11].

$$\frac{1}{Q} = \frac{1}{Q_a} + \frac{1}{Q_s} + \frac{1}{Q_i} \quad (2.27)$$

2.4.3 Surroundings Damping Mechanisms

The largest energy losses in a resonator are due to the surrounding damping, making this mechanism the most important of the loss mechanisms. There are different factors which contribute to this effect [11]. The most relevant factors are the viscous damping, the acoustic radiation and the squeezed film damping, which depend upon the nature of the surrounding fluid, the pressure, and size and shape of the resonator.

2.4.3.1 Viscous Damping

At ambient, *i.e.* at pressures above 100 Pa, the surrounding must be considered as a viscous fluid. The viscosity of the surrounding gas (fluid) introduces two separate damping mechanisms [12, 3]. The first mechanism is related purely to the viscosity of the surroundings fluid, that is, the resistance of one fluid layer to movement over another layer. The vibrations of a resonator will therefore be subject to a similar resistance as the fluid travels over its surface. This has an inertial effect on the resonator since it is related to the acceleration of the surface of the resonator. This inertial effect reduces the resonant frequency.

The second damping mechanism arises from the formation of a boundary layer around the structure. A transverse wave will be created from the vibrational motion. The amplitude of this wave decreases with distance as it travels through the fluid. The penetration depth of the wave defines the distance over which the amplitude falls by e . This depth decreases with viscosity [13], therefore making this effect more important when working in liquids.

2.4.3.2 Acoustic Damping

The motion of the resonator as it vibrates, will cause a displacement of the surrounding gas in the direction of the vibration. The oscillatory motion of the gas particles can form an acoustic wave, which will depend on the size and geometry of the resonator, as well as on

the frequency of operation, wavelength of vibration and properties of the surroundings. This is the so called acoustic radiation. When the width of the resonator is much smaller than the acoustic wavelength, the fluid has time to slip around the edges of it [14]. Therefore, the fluid avoids being compressed and the acoustic wave is not formed. It has also been shown that when the standing wave forming the resonator vibrations are of a wavelength less than the acoustic wavelength, the acoustic radiation is reduced almost to zero [15]. Given the inherently small size of micromachined silicon resonators, acoustic losses can be ignored in the vast majority of cases [11].

The surrounding fluid also has an effect on the natural frequency of the resonator. The mass of the surrounding particles is effectively added to the resonator and hence the natural frequency is reduced. The order of magnitude of the added mass depends on the density of the surrounding and of the material.

2.4.3.3 Squeezed Film Damping

When a resonator is placed close to an adjacent surface and vibrates in the direction perpendicular to the surface, the fluid between the two surfaces is displaced and drawn back. This effect is the so called squeezed film damping, which can become the major damping mechanism.

2.4.4 Structural Damping

The energy coupled from the resonator through its supports to the surrounding structure is related to the structural damping, $1/Q_s$. This damping can be minimised by carefully designing the resonator or by employing a decoupling system between the resonator and its support.

The term $1/Q_s$ is of fundamental importance since it not only affects the Q-factor of the

resonator, but it also provides a key to the performance of the resonator. A dynamically balanced resonator design that minimises the structural damping, provides many benefits:

- High Q-factor, and hence good resolution of frequency.
- A high degree of immunity to environmental vibrations.
- Improved long-term performance, since the influence of the surrounding structure on the resonator is minimised.

2.4.5 Internal Loss Mechanism

In the hypothetical case that the external damping mechanisms, discussed above, were completely removed, the amplitude of the vibrations will still decay with time. This is due to the fact that there is an energy loss mechanism within the resonator material. There are several internal mechanism by which vibrations can be attenuated. However, it has to be stressed that this effect is negligible.

Movement of dislocations and scattering of impurities affect the natural frequency, but only at high temperatures, above 130 °C and 200 °C respectively [16]. Therefore, given the likely operating temperature ranges this form of internal damping can effectively be ignored in silicon resonators.

Thermoelastic effects are also part of the internal mechanism damping process. The flexural vibrations of silicon beam resonators lead to cyclic stressing of the top and bottom surfaces. The majority of the energy employed in displacing the beam is stored elasticity but some of the work is also converted into thermal energy. Material on the surface in compression will rise in temperature whilst the surface in tension falls in temperature. Hence, a temperature gradient is formed across the thickness of the beam. If the deformation of the beam is maintained for a sufficient length of time, heat energy will flow across the gradient

in order to equilibrate the system. Any thermal energy transferred in this way is loss of entropy, and therefore, the vibrations are attenuated.

2.4.6 Summary of the Q Factor

When designing a resonator, it is important to maximise the Q -factor since it simplifies the operation of the resonator and improves the performance of the sensor. The Q -factor is limited by damping effects of surrounding fluids (Q_a), losses from the resonator to the surroundings (Q_s), and internal losses (Q_i), and these should be minimised in order to maximised the Q -factor.

The largest effect Q_a implies that micromechanical resonators will have problems to operate in a dense surrounding. Q_a can be maximised either by the design of the resonator or externally with an electronic control.

In micromachined silicon resonators Q_i is almost negligible, therefore the key is to design a balanced resonant structure (to maximise Q_s) and to optimise Q_a .

2.5 Silicon Properties

Silicon is used for mechanical sensors because it combines well established electronic properties with excellent mechanical properties [17], some of which are listed here,

- High strength to weight ratio (850 Kg/mm²)
- High stiffness (190 GPa)
- No inherent hysteresis and yield
- Good conductor of heat, approximately comparable to Al at room temperature (1.57

W/cm.K)

- Low coefficient of expansion, close to pyrex glass ($2.33 \cdot 10^{-6} \text{ K}^{-1}$)
- Large gauge factor, typically from 50 to 200
- Electrical properties controlled by doping impurities.

Other advantages of silicon include reduced dimensions and mass of the device, batch fabrication, and the fact that it is highly developed for IC technology. The discovery of the high piezoresistivity in silicon in 1954 [18] prompted its use for sensors. The first mechanical sensor was the piezoresistive pressure sensor, but since then an extensive variety of sensors have been designed and produced [19].

The strength of silicon is as high as steel but it cannot be deformed plastically, *i.e.* it is brittle. Hence phenomena such as hysteresis and creep do not exist in silicon. As consequence, a well designed silicon sensor submitted to a high overload will either fail or continue to function with the same response as before.

2.5.1 Piezoresistivity

The piezoresistive effect was discovered in 1856 by Lord Kelvin while examining the effects of induced mechanical strain on conductors. In general metals do not demonstrate a very large piezoresistive effect, therefore, their usefulness for application as sensors is limited. In 1954 Smith reported the piezoresistive effect in silicon to be about 100 times larger than in a typical metal [18].

Piezoresistivity is a material property where the bulk resistivity is influenced by the mechanical stresses applied to the material. Many materials show stress dependence through the mobility or the number of charge carriers as a function of the volume of the material [20]. Volume changes affect the energy gap between the valance and the conduction bands.

This affects the number of charge carriers and, thus the resistivity changes. However, the observed piezoresistance effect is much larger than the predicted by these mechanisms. This has been explained by means of the many-valley model.

For a three dimensional anisotropic crystal, the electric field vector $\bar{\mathbf{E}}$ is related to the current $\bar{\mathbf{i}}$ by a three by three resistivity tensor [21]. Experimentally, the nine coefficients are always found to reduce to six and the tensor is symmetrical,

$$\begin{pmatrix} E_1 \\ E_2 \\ E_3 \end{pmatrix} = \begin{pmatrix} \rho_1 & \rho_6 & \rho_5 \\ \rho_6 & \rho_2 & \rho_4 \\ \rho_5 & \rho_4 & \rho_3 \end{pmatrix} \cdot \begin{pmatrix} i_1 \\ i_2 \\ i_3 \end{pmatrix} \quad (2.28)$$

If the system axis is aligned along the $\langle 100 \rangle$ crystal directions, the normal resistivity components ρ_1 , ρ_2 and ρ_3 define the dependence of the electric field along one of the $\langle 100 \rangle$ crystal axis on the current in the same direction. The cross-resistivity components ρ_4 , ρ_5 and ρ_6 relate the electric field to the current in a perpendicular direction. For an isotropic conductor, for example unstressed silicon, the normal components have the same magnitude ρ , and the cross components are equal to zero. Resulting in the following isotropic relationship,

$$E = \rho i \quad (2.29)$$

In a piezoresistive material, the resistivity depends on the stress in the material. This stress can be decomposed into six components, three normal stresses, σ_1 , σ_2 and σ_3 , along the cubic crystal axis, and three shear stresses, τ_1 , τ_2 and τ_3 , as defined in Fig. 2.7

When the crystal is under stress, the resistivity components change as,

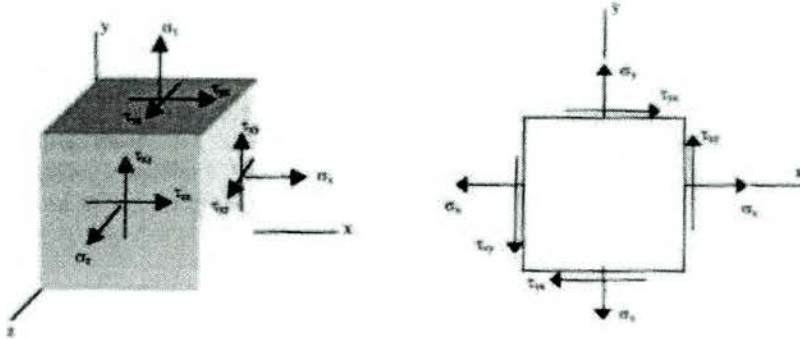


Figure 2.7: Definition of the normal stresses σ_i and the shear stresses τ_i ($i=1,2,3$).

$$\begin{pmatrix} \rho_1 \\ \rho_2 \\ \rho_3 \\ \rho_4 \\ \rho_5 \\ \rho_6 \end{pmatrix} = \begin{pmatrix} \rho \\ \rho \\ \rho \\ 0 \\ 0 \\ 0 \end{pmatrix} + \begin{pmatrix} \Delta\rho_1 \\ \Delta\rho_2 \\ \Delta\rho_3 \\ \Delta\rho_4 \\ \Delta\rho_5 \\ \Delta\rho_6 \end{pmatrix}. \tag{2.30}$$

The piezoresistive effect can be described by relating each of these six fractional resistivity changes $\Delta\rho_i/\rho$, to each of the six stress components. By definition the elements of the matrix are called piezoresistive coefficients, π_{ij} , expressed in Pa^{-1} . Mathematically this yields a matrix of 36 coefficients. However, since the matrix represents properties of a crystal, it must be invariant under the symmetry operations of the crystal lattice under study. The symmetry conditions lead to certain relations between the different matrix components, which reduce the number of independent, non-vanishing components to considerably less than 36. For silicon, which has a cubic crystal structure, the matrix reduces to three independent coefficients, π_{11} , π_{12} and π_{44} , and the matrix takes the following form,

Material	ρ (Ω cm)	π_{11}	π_{12}	π_{44}
		(10 ⁻¹¹ Pa ⁻¹)		
p-Si	7.8	+6.6	-1.1	+138.1
n-Si	11.7	-102.2	+53.4	-13.6

Table 2.1: Adiabatic Piezoresistive coefficients for silicon at room temperature.

$$\frac{1}{\rho} \begin{pmatrix} \Delta\rho_1 \\ \Delta\rho_2 \\ \Delta\rho_3 \\ \Delta\rho_4 \\ \Delta\rho_5 \\ \Delta\rho_6 \end{pmatrix} = \begin{pmatrix} \pi_{11} & \pi_{12} & \pi_{12} & 0 & 0 & 0 \\ \pi_{12} & \pi_{11} & \pi_{12} & 0 & 0 & 0 \\ \pi_{12} & \pi_{12} & \pi_{11} & 0 & 0 & 0 \\ 0 & 0 & 0 & \pi_{44} & 0 & 0 \\ 0 & 0 & 0 & 0 & \pi_{44} & 0 \\ 0 & 0 & 0 & 0 & 0 & \pi_{44} \end{pmatrix} \cdot \begin{pmatrix} \sigma_1 \\ \sigma_2 \\ \sigma_3 \\ \tau_1 \\ \tau_2 \\ \tau_3 \end{pmatrix} \quad (2.31)$$

The stress components are also referenced with the system axis oriented in the $\langle 100 \rangle$ directions. Smith [18] initiated the investigations of these piezoresistive coefficients and found the following values for silicon at room temperature displayed in Table 2.1 [18, 19].

With the values from Table 2.1 π_l and π_t can numerically be calculated for any orientation with the right change of bases. Fig. 2.8 shows the different values of the piezoresistive coefficients depending on the orientation, for both p-type and n-type silicon..

The piezoresistive coefficients are also dependent on dopant concentration and temperature, they decrease as the temperature increases and/or the dopant concentration increases.

The accepted explanation for this phenomenon is the many-valley model, [23, 24]. The many valley model is based on the constant energy surface near the conduction band minimum. In the case of silicon, there are six symmetry related ellipsoidal pockets in the $\langle 100 \rangle$ directions [21]. The origin of the piezoresistive effect is illustrated qualitatively for simplification in 2 dimensions in Fig. 2.10, which shows a constant energy surface which could occur in a two dimensional square lattice.

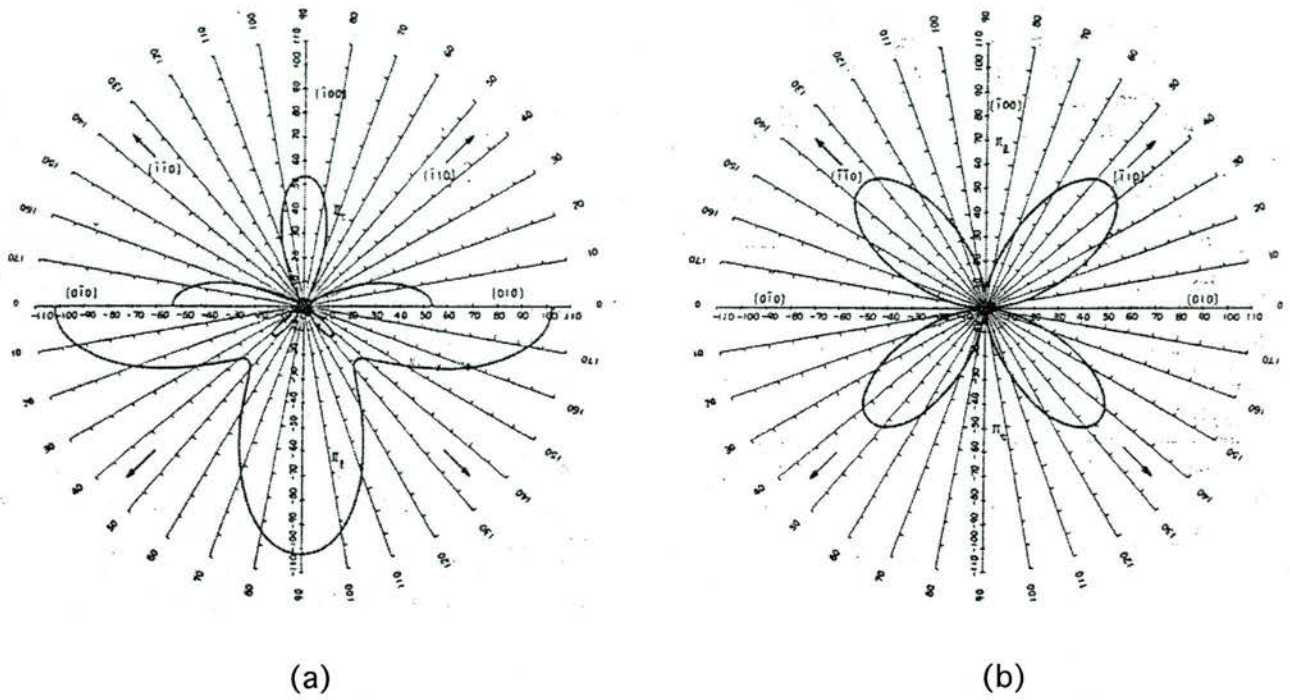


Figure 2.8: Room temperature piezoresistance coefficients (a) In the (001) plane of n-silicon ($10^{-12} \text{ cm}^2/\text{dyne}$). (b) In the (001) plane of p-silicon ($10^{-12} \text{ cm}^2/\text{dyne}$). [22]

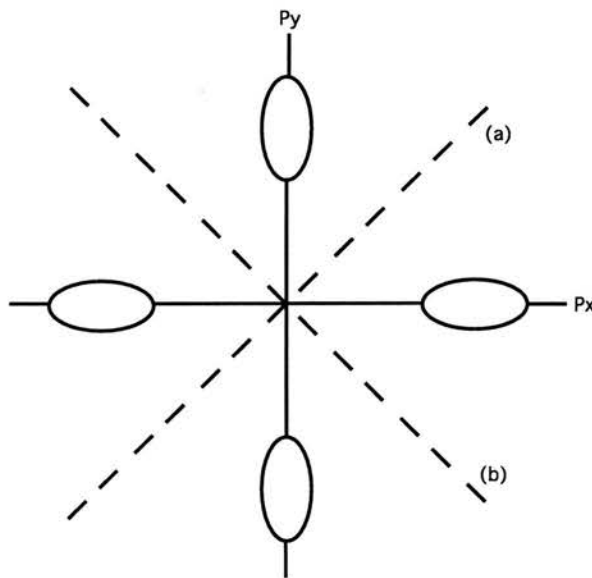


Figure 2.9: A constant energy surface of a multivalley semiconductor with an axis of fourfold symmetry.

There are two types of symmetry in this k space which allow any of the valleys to be transformed into another, the reflection σ_a and σ_b and the rotation C_4 , which is a rotation by $\pi/2$ around the origin, as seen in Fig. 2.9. Thus, the minima are degenerate in the unstrained state, and are occupied by the same number of electrons, and the conductivity is isotropic in the plane [24].

Anisotropic conditions exist when the mobility in one crystal direction is different from the mobility in other crystal directions. This results when the semiconductor is in a stressed state. If the crystal is stressed in the x direction, the x axis is no longer equivalent to the y axis, and the symmetry elements are destroyed. The degeneracy of the minima is therefore removed. The stress distorts the conduction energy bands of the unstressed semiconductor by different magnitudes depending on the direction. The energy levels and curvatures of the energy bands which correspond to the perpendicular directions of the stress, are influenced differently by the applied strain, as can be schematically seen in Fig. 2.10.

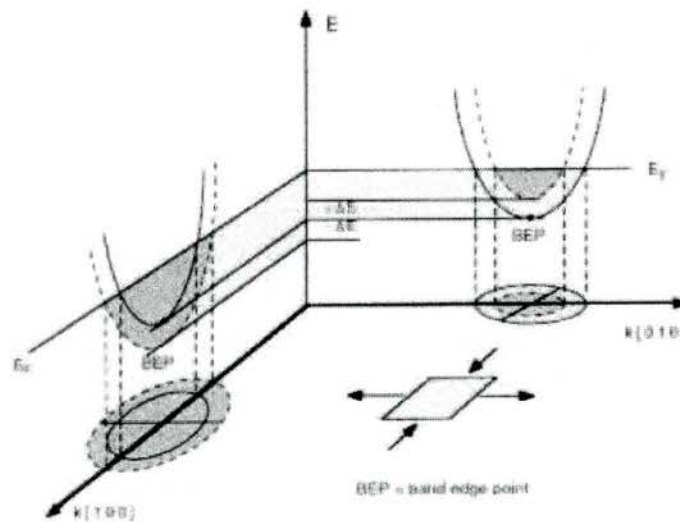


Figure 2.10: Two n-type silicon valleys in k -space, aligned with the $[100]$ axes. E_F is the Fermi level. $+\Delta E$ an energy decrease [19].

The effective masses of the carriers are inversely proportional to the curvature of the energy band in reciprocal k space. Since the carriers mobility is a function of the carriers

effective masses, the strain influence on the energy band curvatures results in directionally dependent influences on the carriers mobility and therefore, the resistivity of the semiconductor. The energy band shifts are also influenced by dopant concentration and temperature. Therefore the energy band sensitivity to stress will also be dependent on these influences.

2.5.2 The Piezoresistive Sensitivity

Based on the theory, the resistance change can be calculated as a function of the cantilever stress. It has been shown that there is a contribution to resistance change from stresses that are longitudinal (σ_l) and transverse (σ_t) with respect to the current flow. Assuming that the mechanical stresses are constant over the resistors, the total resistance change ΔR , neglecting the dimensional changes, is given by,

$$\frac{\Delta R}{R} = \pi_l \sigma_l + \pi_t \sigma_t \quad (2.32)$$

where π_l and π_t are the longitudinal and transverse piezoresistive coefficients respectively; and σ_l and σ_t the longitudinal and transverse stresses.

Since in semiconductors, the change in resistivity in the longitudinal direction is much larger than in the transverse direction [25], the longitudinal piezoresistive coefficient is dominant, and therefore the dimensional change and the transverse piezoresistive effect can be neglected in the following calculations.

Based on the mechanical theory [26], the stress σ on the cantilever can be expressed by,

$$\sigma = \frac{Mz}{I_z} \quad (2.33)$$

where, I_z is the second moment of area, M is the bending moment, and z is the distance away from the central axis of the cross section of the cantilever.

If t is the thickness of the cantilever, then $z \rightarrow t/2$, and the maximum stress will be given by,

$$\begin{aligned}\sigma_{max} &= \frac{Mt}{2I_z} \\ &= \frac{FLt}{2I_z}\end{aligned}\quad (2.34)$$

where I_z is given by,

$$I_z = \frac{\omega t^3}{6}\quad (2.35)$$

Thus, the fractional change of $\Delta R/R$ is given by,

$$\frac{\Delta R}{R} = \frac{3\pi_l FL}{\omega t^2}\quad (2.36)$$

Eq. 2.36 is the fractional change assuming that the piezoresistors located at the maximum stress point. However, the piezoresistor has a profile not only within the plane, but also as function of depth. This factor should be considered if an accurate study is to be undertaken.

Assuming that the profile of the implanted impurity is uniform in depth, the correction factor β is [5]

$$\beta = \frac{R_1}{R_1 + R_2} \frac{2x_j(1 - \frac{L_{R1}}{2L_1})}{t \ln(\frac{t}{t-2x_j})}\quad (2.37)$$

where x_j is the junction depth, L_{R1} the length of the resistor R_1 along the cantilever, t the thickness of the cantilever and L_1 the length of the cantilever, as can be seen in Fig. 2.11. The detailed derivation of the β correction factor can be found in Appendix A.1.

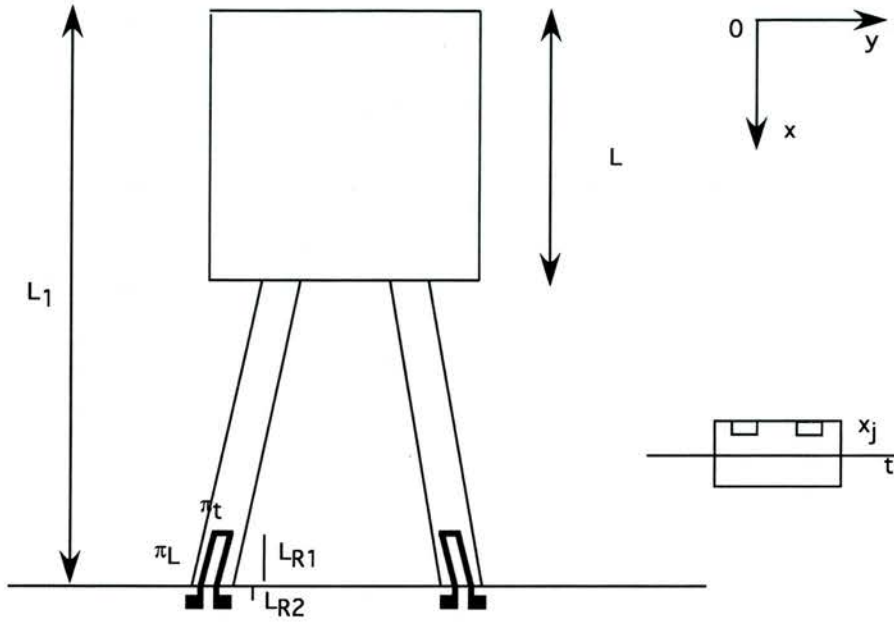


Figure 2.11: A schematic top view of the piezoresistors distribution.

Therefore, the fractional change of $\Delta R/R$ is given by,

$$\frac{\Delta R}{R} = \beta \frac{3\pi_1 F L}{\omega t^2} \quad (2.38)$$

When a single force is loaded at the end of the paddle, introducing Eq. 2.6 and Eq. 2.7 in Eq. 2.38, then, the fractional change of the piezoresistors is,

$$\frac{\Delta R}{R} = \beta \frac{3\pi_1 E t L_1}{2(L_1^3 - L^3 + 2\omega L^2)} y(0). \quad (2.39)$$

From Eq. 2.5 it was concluded that to achieve the maximum deflection long and thin cantilevers with a large paddle area were needed.

To simplify the calculation of the sensitivity of the piezoresistors, the approximation that the piezoresistors are located only on the root (on the base) is needed. The derived sensitivity S_p is then,

$$\begin{aligned}
S_p &= \frac{\frac{\Delta R}{R}}{y(0)} \\
&= \beta \frac{3\pi_l EtL_1}{2(L_1^3 - L^3 + 2\omega L^2)}.
\end{aligned} \tag{2.40}$$

From Eq. 2.40 it can be deduced that the sensitivity of the piezoresistor is proportional to the thickness and inversely proportional to the square of the length.

The minimum detectable force will therefore be determined by the sensitivity of the piezoresistors. Therefore, using Eq. 2.38, it can be seen that the minimum detectable force is proportional to the square of the thickness and inversely proportional to the length of the cantilever.

2.6 Conclusions

From basic mechanics theory first the expression relating deflection to force for the cantilever was determined, and using the force constant definition, the latter was deduced. For maximum sensitivity, a low force constant is needed, which from its ‘unique’ dependence on the dimensions of the cantilever, it was concluded that the longer and thinner the cantilever are, the lower the spring constant is and hence, higher the sensitivity. Nevertheless, as the ultimate use of these cantilevers is the detection of mass, the relative change $\Delta m/m$ should also be considered when designing the cantilevers.

It was shown that the quality factor Q is a key factor when sensitivity is considered. The different mechanisms by which the resonator losses energy were discussed. From which was concluded that a balanced cantilever is needed.

The silicon properties were also studied, particularly the high piezoresistivity, since it can

be used as integrated detection system. Accordingly, the fractional change of the piezoresistivity was deduced, and the theoretical minimum detectable force was calculated. From these calculations it was again deduced that a thin long cantilevers are required with the largest possible piezoresistive longitudinal coefficient.

References

- [1] M. Willemin, *et al.*, 'Piezoresistive Cantilever Design for Torque Magnetometry', *J. Appl. Phys.* **83** (3), 1163-1170, (1998).
- [2] M. Tortonese, *et al.*, 'Atomic Resolution With an Atomic Force Microscope Using Piezoresistive Detection', *Appl. Phys. Lett.*, **62** (8), 834-836, (1993).
- [3] F.R. Blom *et al.*, 'Dependence of the Quality Factor of Micromachined Silicon Beam Resonators on Pressure and Geometry', *J. Vac. Sci. Tech.* **B 10**, (1), (Jan/Feb 1992).
- [4] J. Brugger, *et al.*, 'Lateral Force Measurements in a Scanning Force Microscope With Piezoresistive Sensors', *Transducers'95, Eorosensors IX*, Sweeden, (1995).
- [5] Y. Su, *et al.*, 'Fabrication of Improved Piezoresistive Silicon Cantilever Probes for the Atomic Force Microscope', *Sensors and Actuators A*, **60**, 163-167, (1997).
- [6] J.P. Cleveland *et al.*, 'A Nondestructive Method for Determining the Spring Constant of Cantilevers for Scanning Force Microscopy', *Rev. Sci. Instrum.* **64**(2), 403-405, (1993).
- [7] J.E. Sader and L. White, 'Theoretical Analysis of the Static Deflection of Plates for Atomic Force Microscope Applications', *J. Appl. Phys.* **74** (1), 1-9, (1993).
- [8] S.P. Timoshenko, *Strength of Materials*, Kireger, Malabar, FL (1984).
- [9] A.P. French, *Vibrations and Waves*, Fletcher and Sons, Norwich, GB, (1971).

- [10] M.J. Tudor, *et al.*, 'Silicon Resonator Sensors: interrogation Techniques and Characteristics', IEEE Proc., **135**, D:364-368, (1998).
- [11] M. J. Tudor, and S. P. Beeby, 'Fundamentals and State of the Art', Sensors and Materials, **9** (81), 457-471, (1997).
- [12] Y.H. Cho, A.P. Pisano and R.T. Howe, 'Viscous Damping Model for Laterally Oscillating Microstructure', J. Microelectromechanical Systems, Vol.3, **2**, 81-86, (1994).
- [13] L.D. Landau and E.M. Lifshitz, *Fluid Mechanics*, Pergamon Press, (1959).
- [14] F. Fahy, *Sound and Structural Vibration*, chapter 3, London: Academic Press, (1985).
- [15] R.A. Johnston and A. D. S. Barr, 'Acoustic and Internal Damping in Uniform beams', J. Mech. Eng. Sci., **11** (2), 117-127, (1969).
- [16] W. P. Mason, *Physical Acoustic*, Volume III-part B, Academic Press INC., (1965).
- [17] K.E. Petersen , 'Silicon as a Mechanical Material', Proc. IEEE, **70**(5), 420-457, (1982).
- [18] C.S. Smith , 'Piezoresistive Effect in Germanium and Silicon', Phys. Rev. **94**, 42-49, (1954).
- [19] S.M. Sze , *Semiconductor Sensors*, Wiley Inter-Science, New York, (1994).
- [20] P.W. Bridgman, 'The Effect of Homogeneous Mechanical Stress on the Electrical Resistance of Crystals', Phys. Rev., **42**, 858-863, (1932).
- [21] N. W. Ashcroft and N. D. Mermin, *Solid state Physics*, Holt-Saunders International editions, (1976).
- [22] Y. Kanda , 'A Graphical Representation of the Piezoresistance Coefficients in Silicon', IEEE Trans. Electron. Devices, **ED-29**, 64-70, (1982).

- [23] W. G. Pfann and R. N. Thurston, 'Semiconducting Stress Transducers Utilizing the Transverse and Shear Piezoresistance Effects', *J. Appl. Phys.*, **32**, 2008-2019, (1961).
- [24] R. W. Keyes, 'The Effects of Elastic Deformation on the Electrical Conductivity of Semiconductors', *Solid State Phys.*, **11**, 149-221, (1960).
- [25] Y. Kanda, 'Piezoresistance Effect of Silicon', *Sensors and Actuators A*, **28**, 83-91, (1991).
- [26] S.P. Timoshenco, *Strength of Materials*, Kireger, Malabar, FL (1984).

Chapter 3

Finite Element Analysis of the Cantilevers

3.1 Introduction

Taking into account the design considerations discussed in Chapter 2, the geometries of the cantilevers were investigated. To do so, a flexible modelling tool, finite element analysis (FEA), was used. FEA is a very widely used design tool capable of accurate solutions to many engineering problems: structural, thermal, magnetic field, electric field, fluid and combinations of these such as thermal/stress problems. This chapter introduces the application of FEA to determine the appropriate design for an optimum performance of the devices. Models were validated by constructing simple structures that could be compared with the theory and then developed to represent the fabricated structures.

Given the expense incurred and time required to develop micromachined structures, finite element analysis techniques are becoming very important in ensuring competent designs prior to fabrication for many mechanical silicon devices. FEA can represent complex geometries

with a large number of simply shaped finite elements, with known predetermined properties. These elements are used to form the matrix equations of the structure relevant to the analysis type being performed.

Micromachined silicon cantilevers were evaluated by performing static and modal analysis. A static analysis determines where the maximum stress is created within the cantilever. The basic modal analysis calculates the natural frequencies of vibration and the associated modal displacement of the structure. A spectrum analysis combined with the modal analysis is performed to determine the degree of dynamic balance of the cantilever. The optimisation routine available within ANSYS finite element software package was applied to achieve the optimum dimensions for the cantilever paddles.

3.2 FEA Modelling

The FEA study has been carried out using the ANSYS finite element software package. The stages involved in the modelling process are essentially the same regardless of the type of model being performed. These may be summarised as:

- Build the model - define structural geometry, element types and material properties.
- Define loads and constraints - specify analysis type, structural constraints and applied factors.
- Enter solution phase - define solution parameters and solve.
- Review the results - enter post-processor. Results are available in plot, graph or tabular form.

This can be undertaken either using log files (command code) or a GUI (Graphic User Interface) input. The GUI input is very useful when manipulating the model once constructed

(changing dimensions, material properties and boundary conditions). Log files were used to build the model itself.

FEA uses a large number of elements to represent the structure being modelled. Each element is defined by a number of nodes. The number of nodes determines the accuracy of the solution. As well as the number of nodes, the arrangement of the elements (*i.e.* the finite element mesh) also determines the accuracy of the solution. The mesh density and the number of nodes should be enough to ensure a suitable degree of accuracy, but without wasting computer time. The mesh density should also increase around small features, areas of particular interest and regions of high stress, as larger resolution is needed in these regions. The elements can be defined either by defining the nodes or by defining keypoints in the structure. The geometry of the structure can easily be modified if the elements are defined by keypoints, which is generally a simpler approach.

3.2.1 Model Building

The cantilever structure that was studied is shown in Fig. 3.1. The full model for this structure can be found in Appendix C.

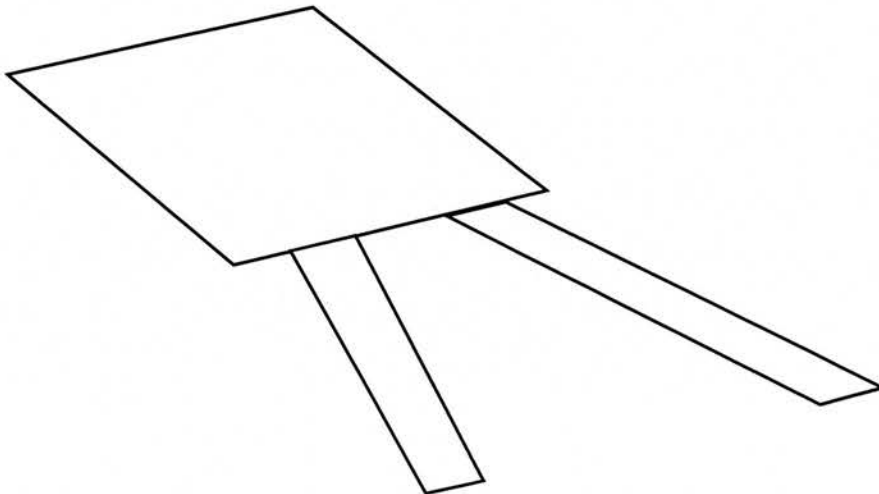


Figure 3.1: Structure of the cantilever model.

The first step in constructing a model is to enter the pre-processor by using the `/PREP7` command. Next, before defining the dimensional parameters, it is necessary to decide if the model is going to be 2D or 3D. In the model to be studied, the dimensions in x and y are much larger than in z direction, so it can be assumed that the stress and strain are only in the plane and thus a 2D model with a given thickness can be used. At the same time the element type should also be chosen. Parameters have been used to define the key dimensions of the structure since such parameterisation allows simple modification of the geometry and subsequent optimisation of the design.

In 2D models, the structure is split into areas which are then meshed. Keypoints are used to define these areas. The keypoint position is defined relative to the origin using Cartesian co-ordinates. The cantilever is symmetrical along the x axis and therefore it is only necessary to model half of the cantilever and reflect it about its line of symmetry.

Referring to Fig. 3.2 keypoints 1 to 10 were defined, and the distances specified using the `K` command and the parameters describing the key dimensions defined earlier. 10 keypoints were needed rather than 7, for the mesh not to go through any sharp corners. The area defined by these keypoints form half of the cantilever, which is done using the `A` command. The model is the reflected in the x axis to achieve the desired structure, this is achieved with the command `ARSYMM`. These areas comprising half of the structure, and the key-points defining these areas are shown in Fig. 3.2. When reflecting nodes and keypoints can overlap, coincident keypoints and nodes can be merged using the command `NUMM`. These compression and merge steps are important since they improve the speed of the analysis.

The next step is to define the nodes where the cantilever is attached, and fixed them. This is done selecting the nodes at the required location using the command `NSEL` and fixing all the degrees of freedom with the command `D`. It is very important to re-select all the nodes in the model after the required ones have been fixed.

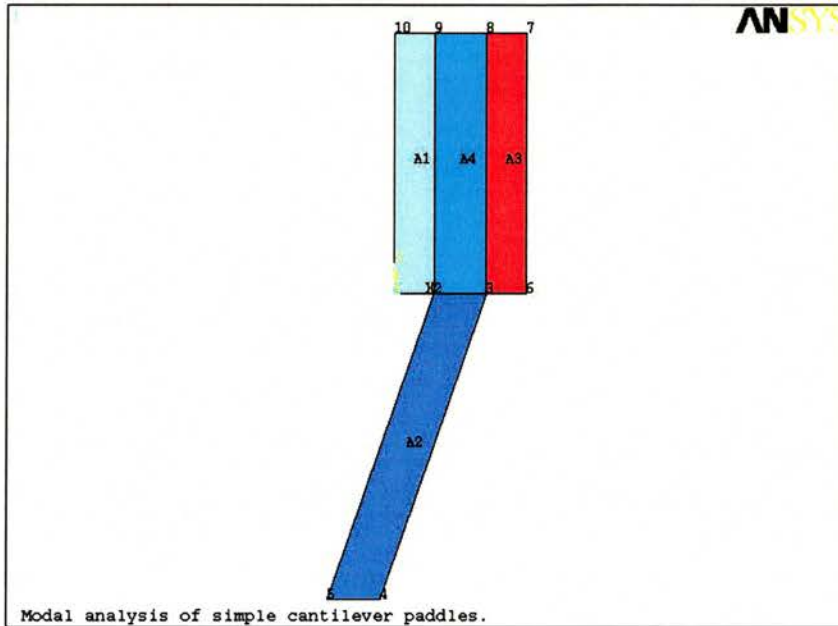


Figure 3.2: Areas comprising half of the structure and the keypoints defining the areas.

The last step before solving the model, is to define the material properties. In the case of silicon, which is an anisotropic material, the properties would be defined by a matrix. The modelling stage is now complete and the structure can be viewed and checked for completeness.

3.2.2 Modal Analysis Theory

Once the structure has been defined, the solution phase is entered. Here the boundary conditions are applied and the analysis type specified, e.g. modal. During the solution phase the program extracts the stiffness matrix $[K]$ and the mass matrix $[M]$ from the model. The solution uses these matrices to determine the resonant frequencies and modal displacements in the following way [1]:

As explained before, the equation for simple harmonic oscillator is given by:

$$[M]\ddot{z} + [K]z = 0 \quad (3.1)$$

Where z is the displacement and K is the stiffness matrix. z is given by,

$$z = z_0 \cos \omega t \quad (3.2)$$

where z_0 is the maximum displacement. Substituting Eq. 3.2 in Eq. 3.1 the following eigenvalue equation is achieved:

$$([K] - \omega^2[M])z = 0 \quad (3.3)$$

which for non trivial solutions ($z \neq 0$) becomes:

$$|[K] - \omega^2[M]| = 0. \quad (3.4)$$

If the order of the matrices is n , then this results in an n^{th} order polynomial, with n roots; $\omega_1, \omega_2, \dots, \omega_n$. These are the eigenvalues of the equation and represent the square of the natural frequencies. The eigenvectors (z_i) can now be calculated from Eq. 3.3, which correspond to the modes.

ANSYS has a number of different ways to calculate the eigenvalues and eigenvectors. The fastest way to solve the equations is the reduce method using the Householder [2] algorithm. It works on a reduced set of degrees of freedom (DOF), called master degrees of freedom (MDOF). This results in an exact $[K]$ but an approximate $[M]$ matrix, which affects the accuracy of the results, so care must be taken in selecting the number and location of the MDOF. The second option to solve the equations is the subspace method which uses the subspace iterative approach based on the Jacobi iterative algorithm. It uses the full $[K]$

and $[M]$ matrices, therefore is accurate but very slow. Other ANSYS options are for cases where damping cannot be ignored, or where mass matrices are not symmetric, e.g. at a fluid structure interface.

The degree of dynamic balance can be determined from the level of stress at the point where the resonator is fixed to the surrounding structure. This approach is achieved by performing a basic FEA modal analysis, combined with the spectrum analysis, enabling the optimum mode for each structure to be found along with its natural frequency and mode shape. Therefore, the resonant frequencies can be predicted before testing the devices. Prior knowledge of the mode shape is also important for selecting the most suitable method of driving the desired mode.

To do the modal analysis, the solution phase is entered with the command `/SOLUTION`. If a modal analysis is to be done, modal analysis is defined, then the number of modes to be extracted and the method of extraction is defined. The solution phase should only be introduced in the modelling program when the model runs correctly.

3.2.3 Review of the Results

The review of the results given by the analysis is carried out in the postprocessor, which is entered using the `/POST1` or `/POST26` command, for reviewing results over the entire model at specific frequencies or `/POST26` command for reviewing results at specific points in the model over the entire frequency range. The output can be extracted in many different forms, from simple displacement plots to graphical plots of stress values along specified paths. For this analysis the displacement and stress contour plots were obtained. When modal analysis results are to be plotted, the desired mode must first be specified using `SET,,n`, where n is the mode number. `PLDISP` command plots the displacement. The strain contour plot is obtained with the `PLNSOL, EPTO,Z` command. The Z label selects the average nodal

Properties	Silicon
Young Modulus (GPa)	170
Poissons ratio	0.28
Density (kg/m ³)	2330
Thermal expansion coefficient (10 ⁻⁶ /k)	2.36

Table 3.1: Isotropic silicon material properties.

values of strain in the z direction to be displayed. The resonant frequencies are listed within the plots.

3.3 Model validation

In order to validate FEA modelling, analytical results are compared with the eigenvalues extracted from the equivalent finite element model for cantilevers. One important part of this process is the validation of the element type. Elastic shell elements were chosen, in particular SHELL63 which describes the element using 4 nodes. Shells have membrane and bending capabilities and are well suited for flexible structures. The shell model is a plan view of the beam, and a defined thickness gives the required third dimension. Moreover, their six degrees of freedom allow the boundary conditions to be modelled for the simply supported structure.

The most straight forward approach to validate the system is to compare the natural resonant frequencies calculated by the analytical methods used in Chapter 2, with the results gained from FE analysis. This validated the mesh densities, element type and material properties used for the detailed modelling. Mesh densities were set to be 1/4 of the cantilever's legs width using the ESIZE command. Since Shell63 is a 2D element type, where the thickness of the cantilever is defined with a real constant, the isotropic material properties of the silicon are used as listed in Table 3.1. The MP command was used to define them.

The natural frequencies calculated with ANSYS are compared with the analytical fre-

Thickness (μm)	FEA Natural Frequency (KHz)	Analytical Natural Frequency (KHz)
2	9.240	9.737
2.5	11.550	11.547
3	13.860	13.855
3.5	16.170	16.166

Table 3.2: FEA vs analytically calculated frequencies for different thicknesses.

quencies in Table 3.2. However, it should be pointed out that when solving the differential equations a modification factor needs to be introduced in the solution. This factor varies with the geometry of the studied cantilevers. For a simple beam the modification factor for the first mode is 3.516 [3, 4]. For the geometry under study, the modification factor was found to be 1.412.

The results showed here prove the element type and mesh densities to be adequate for this model. Nevertheless, the relative difference between values could result from the approximate mass matrix used in the FE analysis.

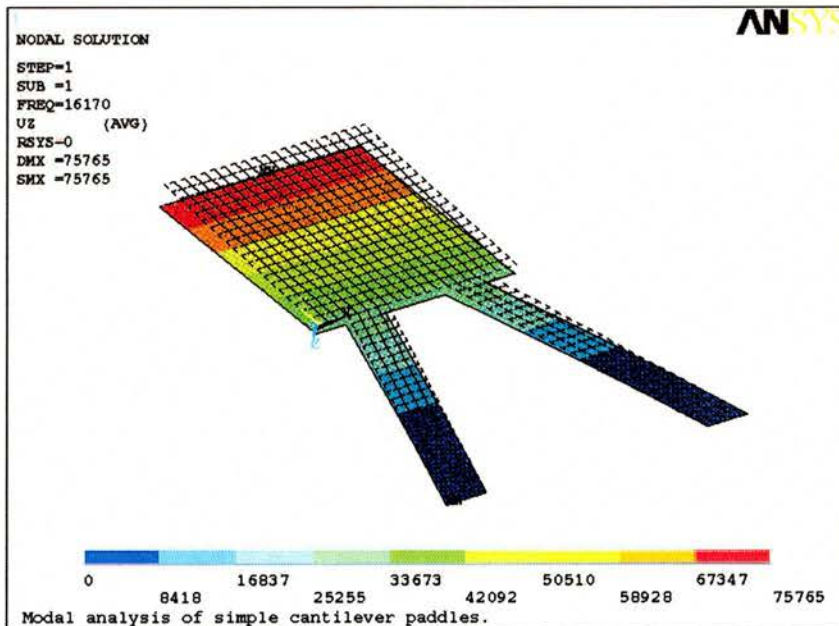


Figure 3.3: First mode calculated with the modal analysis.

It is not just the natural frequency which can be obtained from the modal analysis, but

θ	FEA Natural Frequency (KHz)	π_l
0	15.695	-20
10	15.806	-35
20	16.202	-58
30	17.012	-90
40	18.501	-110

Table 3.3: FEA natural frequencies for different angles of the legs and the respective longitudinal piezoresistive coefficients for n-type silicon.

also the modes related to it. Fig. 3.3 shows the first mode, which is the mode in which we are interested. The first five modes can be seen in Appendix C.

3.3.1 Determination of the right angle

As explained in Chapter 2, the higher the longitudinal piezoresistive coefficient, π_l , the greater the change in resistance. For n-type piezoresistor, the higher the angle of the cantilever arm with respect to the (110) direction, the larger is π_l . On the other hand, the larger the angle with respect to (110) the stiffer the cantilever will become. Therefore a compromise is needed to achieve the best performance.

Different angles for the same cantilever dimensions were studied. In Table 3.3 the different values of the natural frequencies for the different angles can be seen, along with the respective values of π_l . The increased in frequency with the angle reflects the higher stiffness at larger angles.

From these results, and the strain results explained in the following section, it was concluded that the optimal angle was 20° . The strain analysis shows that the strain distribution changes with the angle, see Fig. 3.5,3.6,3.7. Therefore, from now on all the FE analysis will be performed on 20° angled cantilevers.

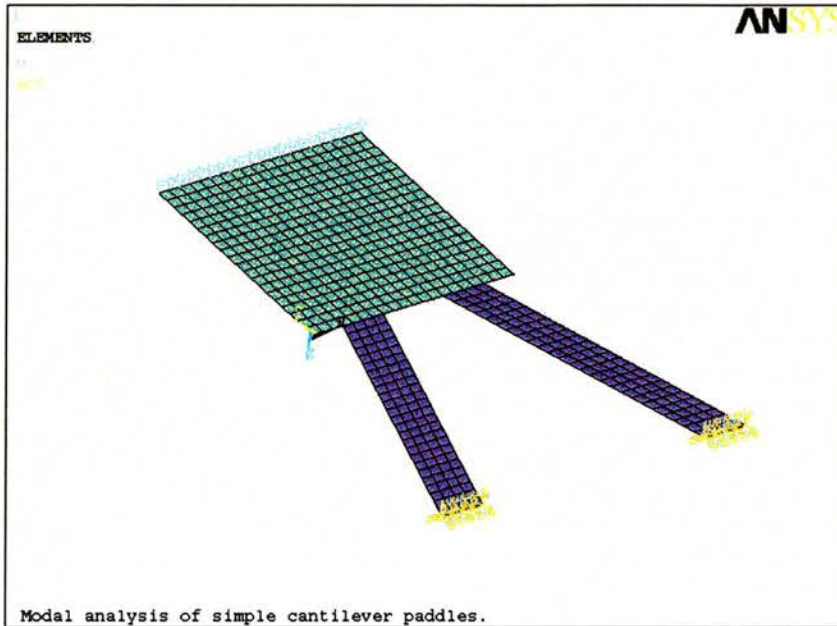


Figure 3.4: Strain distribution on a cantilever paddle.

3.3.2 Strain in the Cantilever Paddles

Having verified the element type and mesh density, and optimised the geometry, different studies on the cantilevers could then be performed. The first was undertaken to determine where the highest strain is located since that is where the piezoresistor should be placed. In this study the displacement of the cantilever was chosen to be equal to a typical amplitude of vibration during operation of the real device. The analysis used is a structural static analysis with the maximum displacement applied to the end of the paddle, as can be seen in Fig. 3.4.

Fig. 3.5 shows the strain distribution along a cantilever with legs orientated at 0° respect the (110) direction, where as expected the maximum strain is at the base of the cantilever. Fig. 3.6 also illustrates the strain when the angle of the legs is 20° , and Fig. 3.7 shows the strain for a cantilever with the legs at 40° .

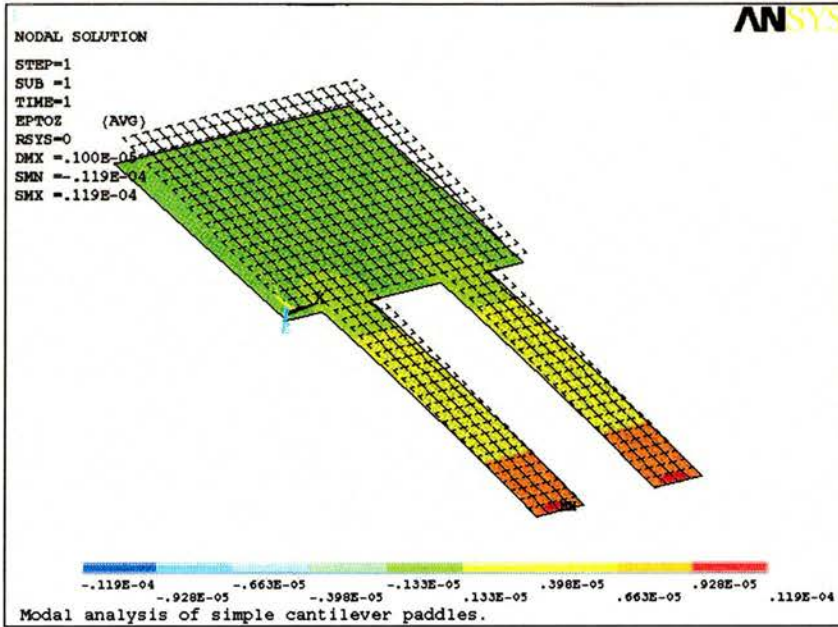


Figure 3.5: Strain distribution on a 0° cantilever paddle.

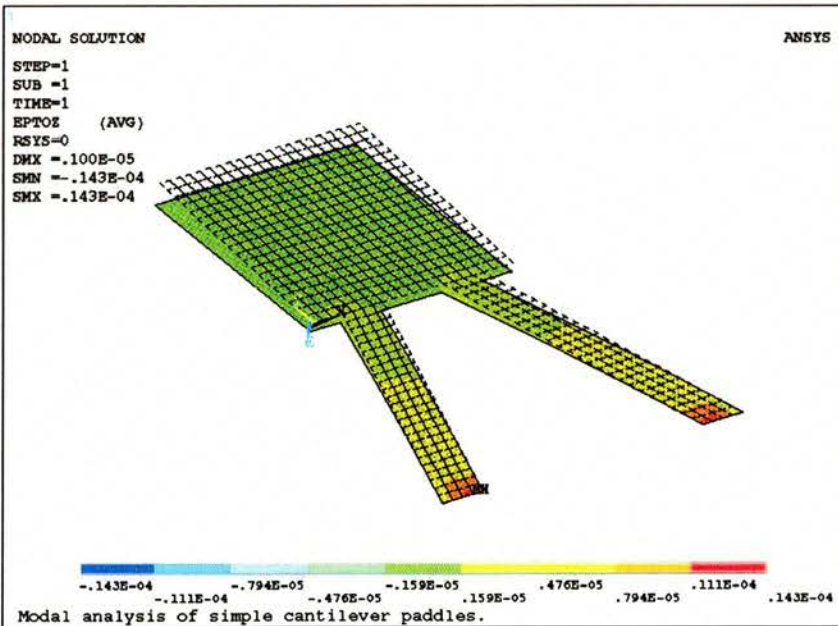


Figure 3.6: Strain distribution on a 20° cantilever paddle.

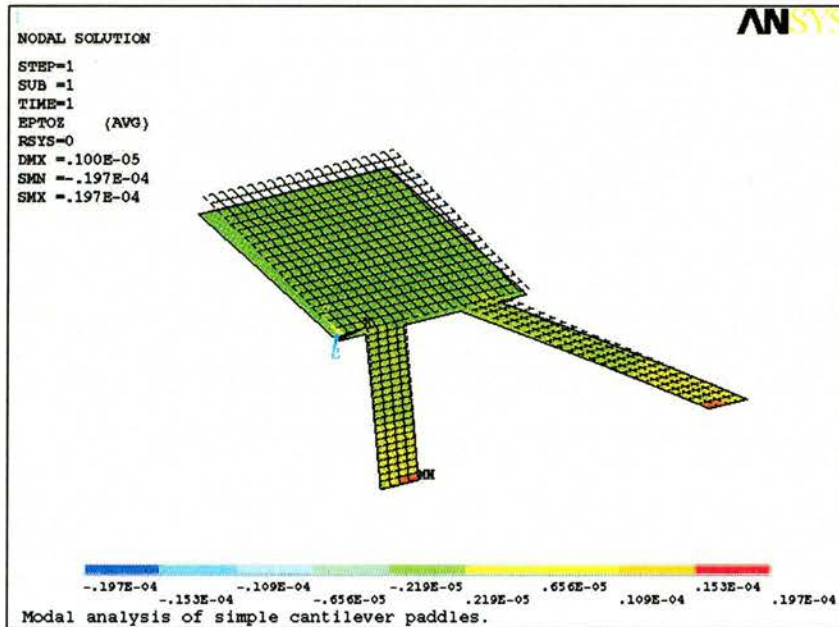


Figure 3.7: Strain distribution on 40° a cantilever paddle.

3.4 Cantilevers with a Long Iron Cylinder attached to the Paddle

As explained in Chapter 5, an iron small cylinder is attached to the paddle in order to be able to excite the cantilever magnetically. The following FE analysis was conducted with the aim of predicting the large natural frequency change. For this new model two different material types have to be simulated, silicon for the cantilever and iron for the magnetic particle. The element type SHELL63 does not allow different material types and cannot describe the interface between them. Therefore, SHELL99 is used for this model. SHELL99 has the same properties as SHELL63 (has 6 degrees of freedom), but it allows the possibility of defining many different layers. SHELL99 is also a 2D element type, so 2 real constants have to be defined, one for the cantilever and another one for the magnetic particle.

Fig. 3.8 show the system studied and its first mode. The cantilever paddle dimensions

First Mode	FEA (Hz)	Experimental (Hz)	% Difference Between Frequencies
Without Particle	12,000	11,700	2.5
With Particle	430.9	367.86	14

Table 3.4: FEA and experimental natural frequencies with and without the magnetic particle on the paddle, along with the difference percentages.

chosen were $250\mu\text{m}$ long arms at 20° , $200\mu\text{m}^2$ paddles, and $2.5\mu\text{m}$ thickness. As can be seen the resonant frequency is now of the order of 300 Hz, which is a much lower frequency compared with the natural frequency of the cantilever. Table 3.4 compiles the natural frequencies given by FE analysis with and without the magnetic particle, and the experimental frequencies, along with the difference percentages. The mass of a $100\mu\text{m}$ diameter and $500\mu\text{m}$ long iron particle is about $40\mu\text{g}$, which is a big mass relative to the cantilever mass producing a big change in the resonant frequency.

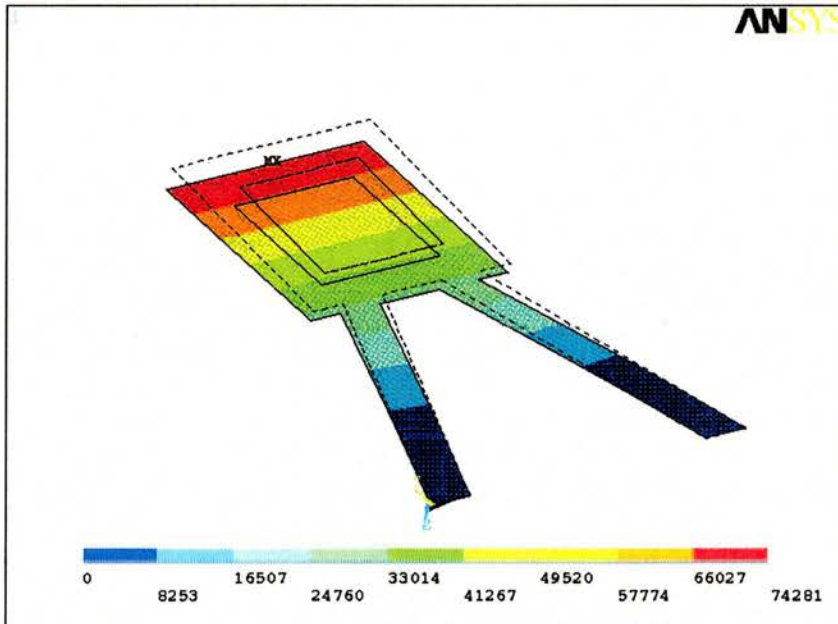


Figure 3.8: First mode of a cantilever with a $100*500\ \mu\text{m}$ magnetic particle on the paddle.

The ultimate application of these cantilevers is to measure very small changes of mass by means of the resonant frequency change. This was simulated by adding the equivalent

Mass (μm)	FEA Δf (Hz)	Experimental Δf (Hz)
0	430.907	367.86
1	426.665	356.86
2	422.291	351.00
5	410.318	342.00
10	392.202	320.00

Table 3.5: Change in frequency per μg for the FE analysis and experimental data.

of $1\mu\text{g}$, to the iron particle (increasing the thickness of the magnetic particle) and solving for the modal analysis. Table 3.5 shows the change in frequency per $1\mu\text{g}$, which it gives a sensitivity of 276 ng/Hz . The experimental sensitivity, as explained in Chapter 5, is of 240 ng/Hz .

3.5 Cantilevers with the Electroplated Nickel Pillars

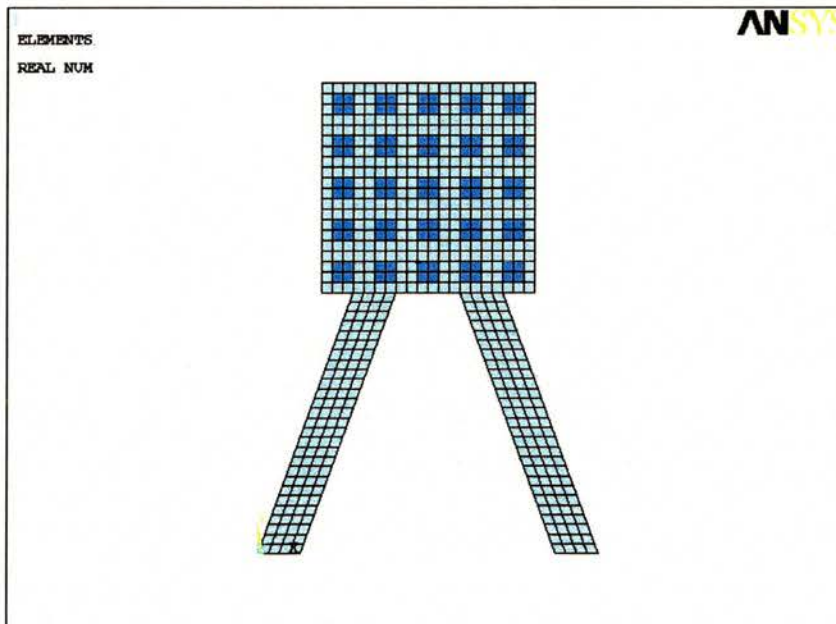


Figure 3.9: Simulated electroplated cantilever geometry.

As will be explained in Chapter 6 it was decided to include the magnetic particles within the microfabrication process, electroplating them. Due to the experimental limitation dis-

cussed in Chapter 6, it was decided to electroplate an array of particles. This new geometry is defined for FE analysis and the modal analysis was performed in order to see, once again, how the resonant frequency changes with the additional mass. Fig. 3.9 shows the cantilever containing the simulated electroplated particles. The element type SHELL99 was also used for this FE analysis, with the appropriate material properties. Fig. 3.10 shows the first mode of this new geometry, which is the same as in the previous cases. Since the total mass added to the cantilever is less than in the case of the iron cylinder, the resonant frequency is not as low as in the previous case, but 2035.70Hz.

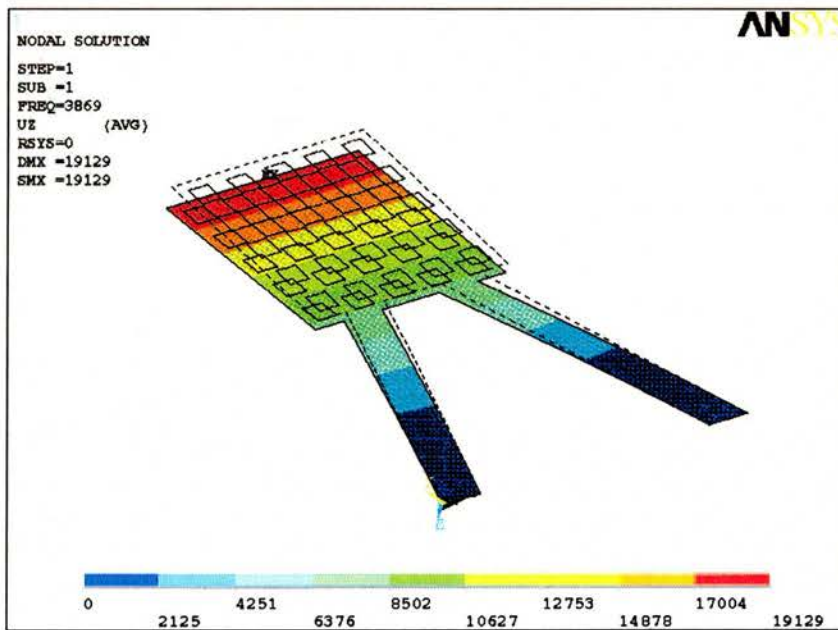


Figure 3.10: First mode and resonant frequency for the cantilever with the electroplated nickel pillars.

The initial mass of the cantilever is lower than in the previous case, therefore it is expected to have a larger sensitivity since the relative change $\Delta m/m$ is smaller. To prove this the same routine was used, adding the equivalent to 1ng and solving for the modal analysis. Fig. 3.11 contains the different frequency values for the different masses. From these values it can be obtained a sensitivity of 5ng/Hz is possible, which is fifty times more sensitive.

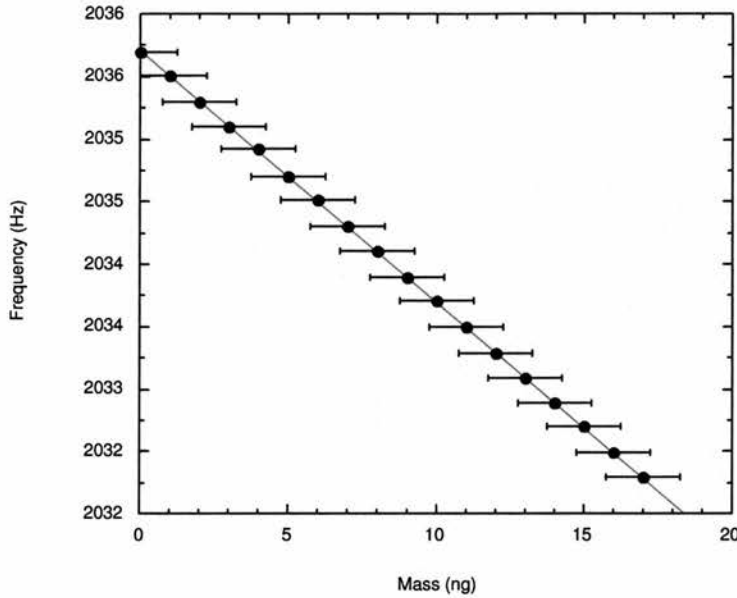


Figure 3.11: FEA frequency change vs. mass, for a cantilever with electroplated nickel pillars.

3.6 Conclusions

The good agreement between the FEA results and the analytical results proves the models useful in predicting the resonant frequencies of vibration of the cantilevers, validating the element type and the mesh density. It can also be deduced from this validation study that the mode in which we are interested is the first mode, since it is a clean vibrational mode.

In addition to selecting the current mode of vibration, it was also necessary to determine the correct angle of the legs and the right position for the piezoresistors. Static analysis of the model predicted, as expected, that the largest stress was produced at the base of the legs. The modal analysis showed that at higher angles the stiffness of the cantilevers was larger. This involves a compromise since the higher the stiffness the more difficult it will be to excite the cantilevers and also to detect the frequency change, but the devices will be mechanically more stable. This, coupled with the fact that the piezoresistive coefficient is larger at higher angles implied a choice of a 20° angle, as the optimal values for a mechanically stable system

with high piezoresistive response.

Experimental results were also compared with the FEA results. Not only did this predict correctly the frequency shift for the cantilever with the particle attached particle, but also the mass sensitivity. This is a very encouraging result, since the same study in the models of the final devices predicted a sensitivity of 5ng/Hz. This is in the regime of sensitivity required to compete with existing analytical techniques.

References

- [1] ANSYS User Manual, 4, Theory, Revision 5.0.
- [2] ANSYS User Manual, 1, Procedures, Revision 5.0.
- [3] P.M. Morse, *Vibration and Sound*, McGraw-Hill, New York, 119-120, (1936).
- [4] J. A. Siddles *et al.*, 'Magnetic Resonance Force Microscopy', *Rev. Mod. Phys.* **67**, (1), (January 1995).

Chapter 4

Batch Process

4.1 Introduction

The results of a review proved that the ideal mechanical and electrical properties of silicon, together with the highly developed IC technology and micromachining etching techniques, make it ideal for the fabrication of a great diversity of microsensors. It is important to note that Si is the only semiconductor whose oxide (SiO_2) is compatible with photolithographic masking, has excellent thermal stability, and has very low electronic defect densities at the Si/ SiO_2 interface. This is one of the reasons why historically silicon has been used more (than any other semiconductor) in IC development. Silicon micromachining techniques consist of bulk and surface micromachining. Bulk micromachining processes are those that form devices within the single crystal silicon wafer, or involve the removal of large parts of the silicon wafer. Surface micromachining on the other hand, involves processes whereby the devices are formed on top of the wafer by adding materials, often a layer of polysilicon or thin metal films.

In the first part of this chapter a review is given of the silicon microfabrication techniques

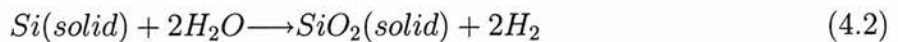
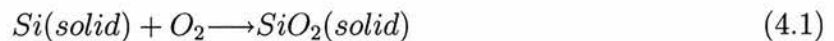
relevant to this project. This is followed by a discussion of how these techniques were used in designing and implementing the batch process for these devices, which included the design of the masks.

4.2 Silicon Microfabrication Techniques

4.2.1 Oxidation

The oxidation of silicon is necessary throughout the process of fabricating integrated circuits. It is used in several ways: as a mask for implant or diffusion of dopant into silicon, as surface passivation, as an insulator between devices, as a component in MOS structures, and as an electrical insulator in multilevel metallisation systems. There are also several techniques for forming the oxide layer, such as thermal oxidation (wet or dry), chemical vapour deposition (CVD), and rapid thermal oxidation (RTO).

Silicon has a high affinity for oxygen, which makes it very easy to form an oxide layer, since it is only necessary to expose the silicon to an oxidising ambient atmosphere. The chemical reactions describing the thermal oxidation in oxygen or water vapour are given by Eq. 4.1 and Eq. 4.2



While many materials oxidise by the metals diffusing to the oxide surface and reacting with oxygen, in the case of silicon, the oxygen diffuses through the oxide and reacts at

the silicon surface. The basic process involves shared valence electrons between silicon and oxygen. During the course of the oxidation process the Si-SiO₂ interface moves into the silicon. However, the volume expands, resulting in the external surface not being coplanar with the original silicon surface. Based on the densities (2.22 gr/cc for oxide and 2.33 gr/cc for silicon) and molecular weights (60 and 28 respectively), it can be shown that for growth of an oxide of thickness d , a layer of silicon $0.44d$ thick is consumed, as shown in Fig. 4.1.

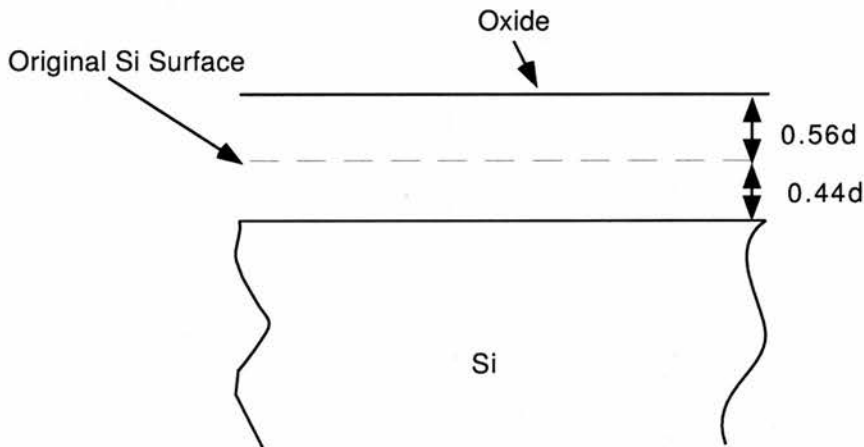


Figure 4.1: Consumption of silicon during thermal oxidation

The oxide occupies more space as it grows than does the silicon consumed, therefore an appreciable compressive stress in the oxide near the interface is generated. This stress associated with the film is important, since high stress levels can contribute to wafer warpage, film cracking, and defect formation in the underlying Si. However, above about 950°C, silicon dioxide has a low enough viscosity for the stress to relax, and little residual stress remains. Lower stress has been found in wafers oxidised in wet oxygen than in those oxidised in dry oxygen [1], [2]. This fact is consistent with a lowering of the silica viscosity when it contains H₂O [3].

4.2.1.1 Wet and Dry Oxidation

The oxidation technique chosen depends upon the thickness and oxide properties required. Oxides that are relatively thin and those that require low charge density at the interface are typically grown in dry oxygen. When thick oxides ($> 0.5\mu\text{m}$) are desired, steam is used. Higher pressure allows thick oxide growth to be achieved at moderate temperatures and in reasonable time. Wet oxidation occurs at a substantially greater rate than for dry oxidation. Since the masking oxide is generally removed, the rate at which it is grown becomes more important than the charge density, and wet oxidation is more commonly used. One-atmosphere oxide growth, the most commonly used technique, is carried out in a quartz or silicon carbide diffusion tube with the silicon wafers held vertically in a slotted quartz boat made of quartz or silicon carbide, see Fig. 4.2.

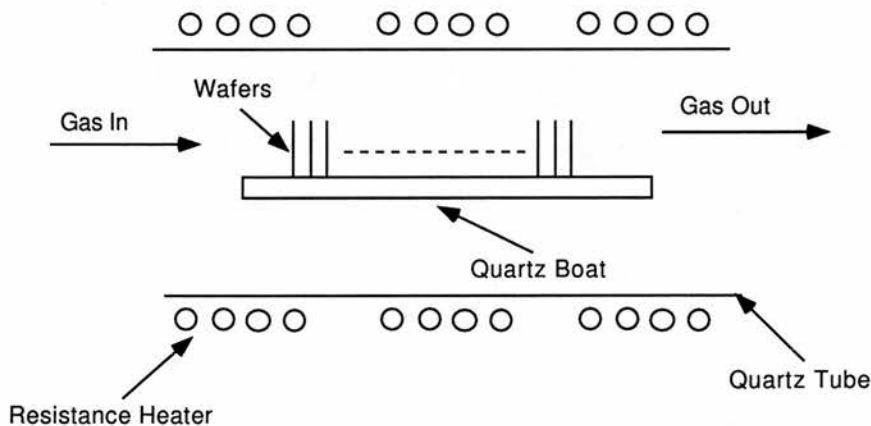


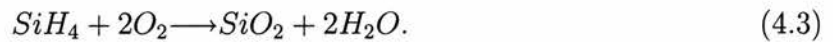
Figure 4.2: Schematic diagram of an oxidation furnace.

Typical oxidation temperatures range from 800 to 1200 °C and should be held to within $\pm 1^\circ\text{C}$ to ensure uniformity [4]. In a standard procedure the wafers are cleaned, dried, placed on the boat, and automatically inserted into a furnace, which is ramped up to the growth temperature. Ramping is used to prevent wafer warpage. Following oxidation the furnace is ramped down and the wafers are removed.

4.2.1.2 Low Temperature Oxidation (LTO)

Oxides used as insulators between conducting layers are firstly deposited, then densified by annealing, and finally plasma-etched to open any windows. The main difference between depositing the oxide and growing it, is that when growing oxide, the silicon is consumed, and when depositing oxide, no silicon is consumed.

Several deposition methods are used to produce silicon dioxide. They are characterised by different chemical reactions, reactors and temperatures. Films deposited at low temperatures, lower than 500°C, are formed by reacting silane, oxygen and, sometimes dopant gas, such as phosphine [5, 6, 7]. The use of silane to deposit SiO₂ at lower temperature was first reported in 1967 [8]. Using O₂, the reaction often assumed is,



However, when the temperature is below about 500°C and the silane concentration is low, no water is detected experimentally [9], thus leading to the reaction of Eq. 4.4 being more probable in that temperature range,



The main advantage of silane-oxygen reactions is the low deposition temperature, which allows films to be deposited over aluminium metallisation. Consequently, these films can be used for passivation coatings over the final device and for insulation between aluminium levels.

The main disadvantages of silane-oxygen reactions are poor step coverage and particles caused by loosely adhering deposits on the reactor walls [4].

4.2.1.3 Preoxidation Surface Cleaning

In discussing the technologies used and properties obtained, it should be emphasised that thin oxide growth is influenced by the cleaning techniques used and the purity of the gases used.

Before placing wafers in a high-temperature furnace they must be cleaned to eliminate both organic and inorganic contamination arising from previous processing steps and handling. Such contamination, if not removed, can degrade the electrical characteristics of the device as well as contribute to reliability problems.

A cleaning sequence should proceed in the following order:

1. Remove gross organic material and particles.
2. Remove organic films.
3. Remove surface oxide.
4. Remove surface-adsorbed ions and plated-metal contaminants.
5. Reform contamination-free native oxide.
6. Remove all traces of cleaning solutions and all particles from the surface of the reformed native oxide film.

An alternative cleaning cycle is the RCA clean:

1. Remove gross organics with perchloroethylene (tetrachloroethylene).
2. Remove residual organic films with an $\text{H}_2\text{O}_2\text{-NH}_4\text{O}$ (basic) solution.
3. Remove metallics with an $\text{H}_2\text{O}_2\text{-HCl}$ (acidic) solution.

4. Rinse thoroughly in deionised water.
5. Dry.

Depending on the final clean, substantial differences in the composition of the native oxide are observed. A hydrogen-peroxide-based cleaner will leave a thinner, cleaner, and apparently rather volatile oxide [10]. Presumably through the kind of oxide remaining, the clean affects the linear oxidation rate constant [1].

4.2.1.4 Oxide Charges

The Si-SiO₂ interface contains a transition region, both in terms of atomic position and stoichiometry, between the crystalline silicon and amorphous silica. Various charges and traps are associated with the thermally oxidised silicon, some of which are related to the transition region. A charge at the interface can induce a charge of the opposite polarity in the underlying silicon.

When the oxide is grown, it gets positively charged, which induces a negative charge in the silicon. In the case of p-type substrate, this accumulation of negative charge, can cause inversion and lead to the shorting of n-type contact windows.

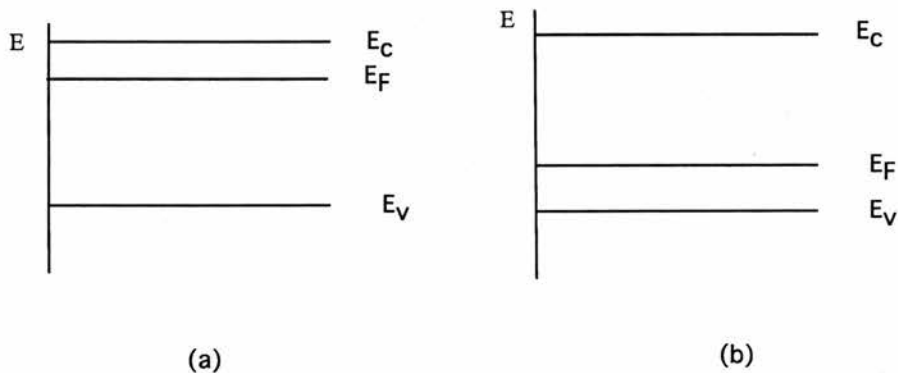


Figure 4.3: (a) The energy bands of a n-type semiconductor. (b) The energy bands of a p-type semiconductor.

Fig. 4.3(a) shows the valance and conduction energy band versus distance of a n-type semiconductor, where E_c is the conduction energy level, E_v is the valance energy level and E_F is the Fermi level. The fact that E_F is closer to the conduction band indicates that is a n-type semiconductor. Fig. 4.3(b) shows energy bands of a p-type semiconductors as is indicated by the Fermi level being closer to the valence band.

An excess of free electrons at the silicon surface, due to the induced negative charge, causes the energy bands to bend. In the case of a n-type silicon wafer, Fig. 4.4(a), the energy bands bend downwards, but as the majority carriers are electrons it makes no difference to the polarity.

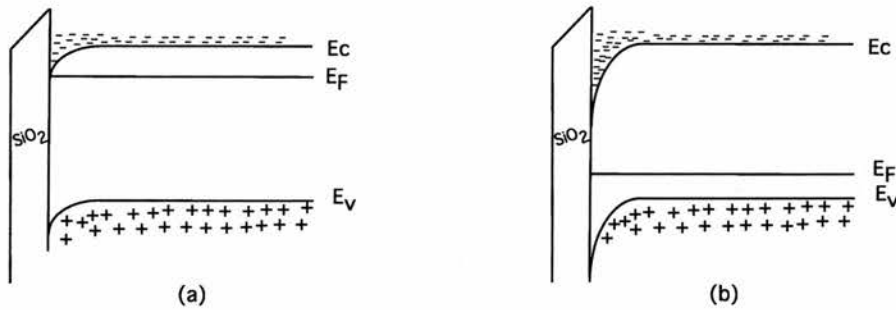


Figure 4.4: Energy band diagrams when the induced negative charges are present, for: (a) n-type silicon; (b) p-type silicon.

On the other hand, in a p-type silicon wafer, Fig. 4.4(b), measures to prevent this should be taken since the addition of free electrons to a p-type silicon surface could cause inversion to occur.

To avoid this the whole wafer can be implanted with p++ impurity so that there is an excess of majority carriers, such that when the oxide is grown and the silicon becomes negatively charged, the excess positive charge will recombine with the electrons so that the surface retains the characteristics of a p-type semiconductor, see Fig. 4.5.

Annealing is done to reduce the amount of interface traps and trapped oxide charge.

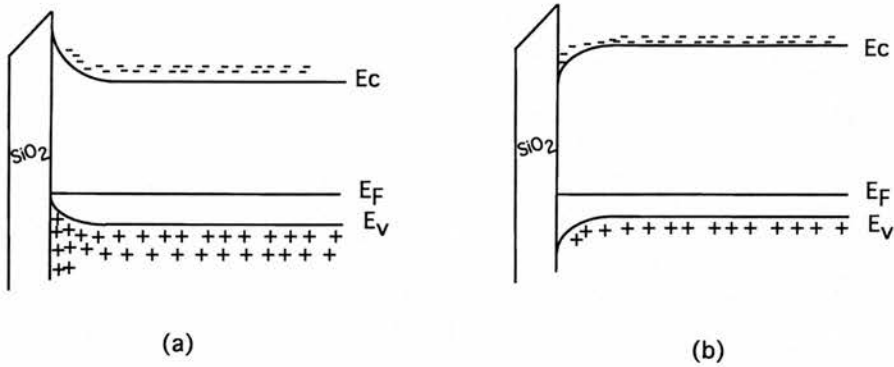


Figure 4.5: (a) Energy bands of a p++ silicon. (b) Energy bands after the p++ silicon has been negatively charged.

4.2.1.5 Masking Properties

A silicon dioxide layer can prevent dopant atoms from reaching the silicon surface, since it is a very good mask for both ion implantation and diffusion. For this to be effective, the diffusion in the oxide must be slow enough with respect to the diffusion in the silicon, so that the dopants do not diffuse through the oxide and reach the silicon surface, as can be seen in Fig. 4.6.

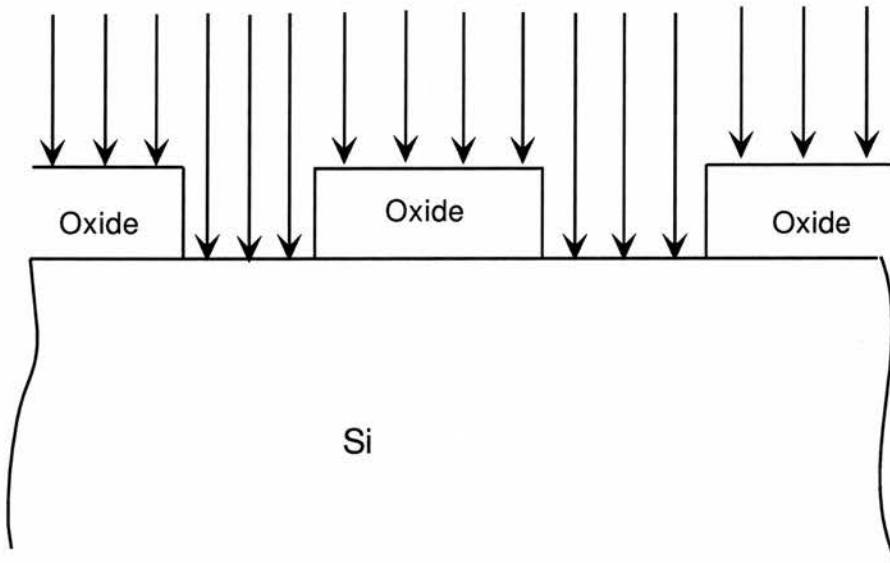


Figure 4.6: Silicon dioxide as a mask layer for dopants.

The values of diffusion constants for various dopants in SiO_2 depend on the concentration,

Dopants	Diffusion constants at 1100° cm ² /s
B	3.4×10^{-17} to 2.0×10^{-14}
P	2.9×10^{-16} to 2.0×10^{-13}
As	1.2×10^{-16} to 3.5×10^{-15}

Table 4.1: Diffusion constants in SiO₂.

properties, and structure of the SiO₂. Table 4.1 shows some diffusion constants for the dopants used.

Typically, oxides used for masking common impurities in conventional device processing are 0.5 to 0.7 μm thick.

4.2.1.6 Passivation

Passivation is the term used for the protection of the junctions and surfaces of integrated circuits from the environment, minimising unwanted electrical activity at the device surface. Hence, passivation results in a marked improvement in device performance, stability, and uniformity of properties from device to device. Passivation is achieved by forming a thin insulating layer on the semiconductor surface. A layer of silicon dioxide is most commonly used, though there are some other techniques.

4.2.2 Lithography

The patterns on each layer are defined by a processing sequence called photolithography. This sequence begins with a computer generated transparent quartz mask which has opaque regions of chromium to define patterns. The quartz mask is designed to have the exact sizes and widths of the circuit elements which have been previously determined. A thin layer of a photosensitive organic material (photoresist), typically 1 μm thick, is then deposited onto the wafer, covering the film to be defined. After exposing the photoresist with a UV light

source flashed through the mask onto the sample, the mask image is then transferred into the photoresist following chemical development. An illustration of the basic photolithographic process can be seen in Fig. 4.7.

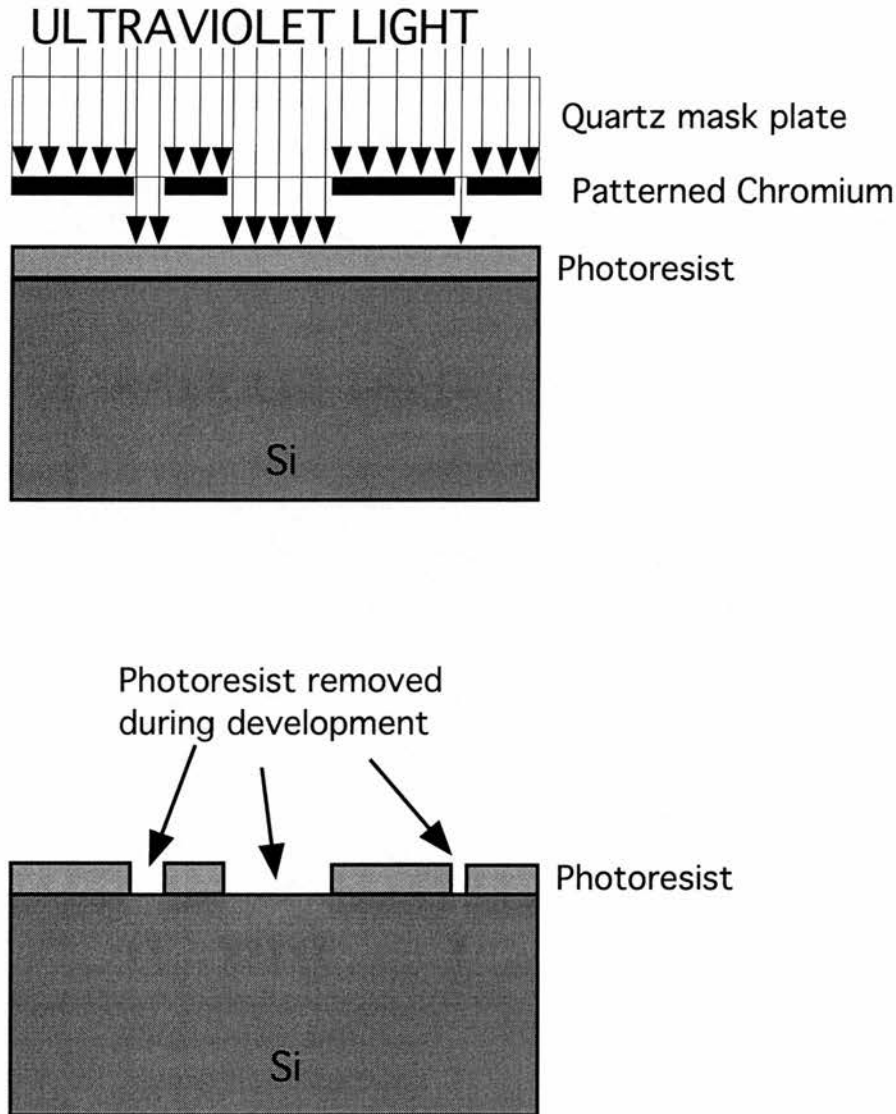


Figure 4.7: Basic photolithographic process.

The patterned photoresist, in turn, acts as a resistant mask when the underlying material is processed with a wet chemical etchant, reactive ion etch, ion implantation, or other semiconductor processes. Finally, the photoresist is stripped in either a O_2 plasma or fuming nitric acid, leaving only the layer with the transferred patterns. This photolithographic step

is repeated for subsequent layers with the corresponding masks.

Usually, more than one mask is required to fabricate circuits or devices in silicon therefore, masks should be designed to ensure that they line up with each other. It is essential that the different masks used in the process align correctly with one another. To achieve this, alignment aids are used. In each case alignment aids are defined and etched into a layer on the wafer using standard photolithographic techniques. A second mask is for patterning the subsequent layer is aligned to the alignment aids etched into the previous layer. When correctly aligned the pattern is exposed to UV-light.

Masks can be light field or dark field. A light field mask is largely transparent with small features defined in chromium on the mask plate. A dark field mask, on the other hand, is largely opaque with small features being etched through the chromium. With a light field mask, the majority of the wafer is exposed. If the photoresist is positive then the exposed regions will be dissolved leaving the resist defining the small features undeveloped. The dark field mask, also assuming a positive photoresist, results in only small regions of the wafer being exposed causing the photoresist in this regions to be developed out. Regions of the silicon wafer where the resist has been developed out will be exposed to the subsequent processing step.

4.2.2.1 Photoresist

The first photoresist used in IC fabrication produced a negative image and was thus called negative photoresist. That is, where the photoresist exposed to light is polymerised and becomes more difficult to remove, so that when the resist is developed the polymerised region remains, as shown in Fig. 4.8.

Later on, positive photoresists based on a different chemistry were used. In this case, the exposure to light breaks bonds in the photoresist making it soluble in the solvent developer

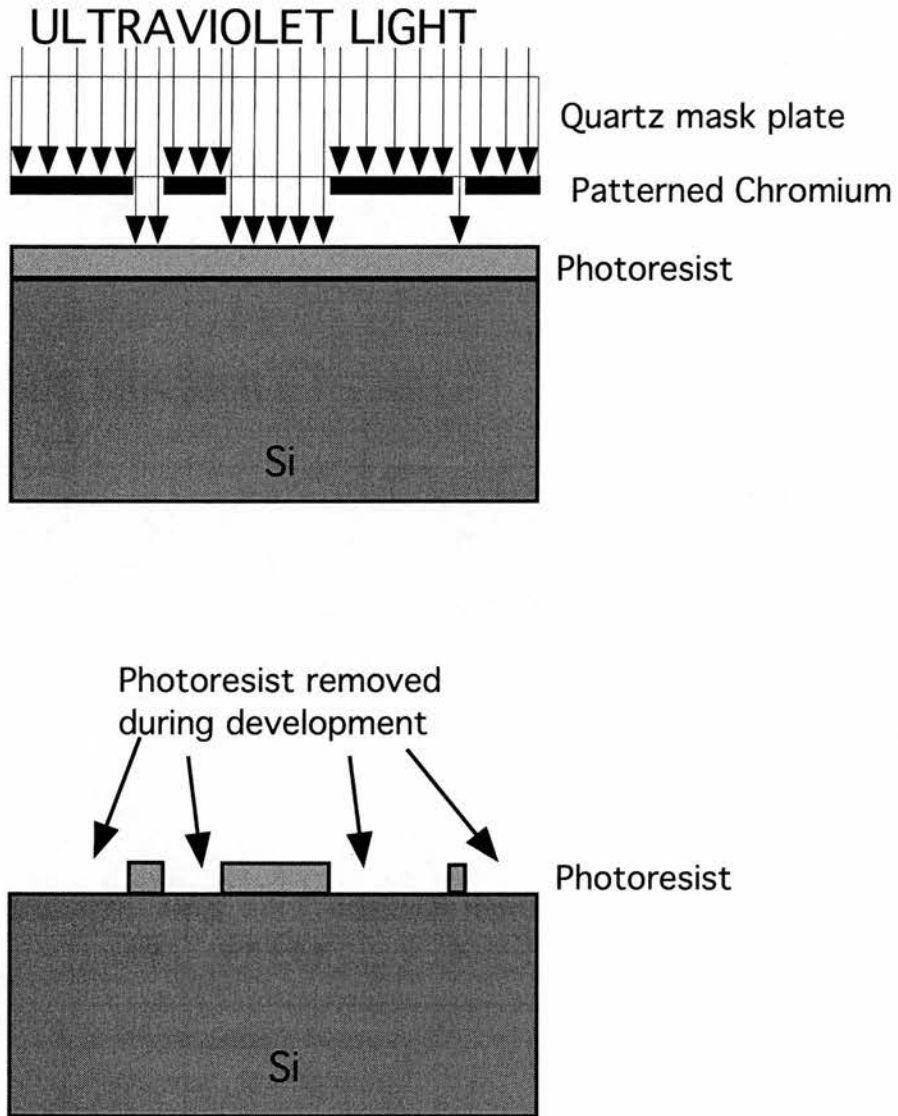


Figure 4.8: Effect of negative resist on pattern.

and it is easily removed, as shown in Fig. 4.7. Since the exposed regions are removed, the resist is referred to as positive.

4.2.3 Impurity Diffusion and Ion Implantation

The key processes to introduce controlled amounts of dopants into semiconductors are diffusion and ion implantation. The semiconductor substrate can be selectively doped with these techniques to produce either n- or p-type regions.

Thermal diffusion is a thermally activated process in which atoms or molecules in a material move from high to low concentration regions, as illustrated in Fig. 4.9.

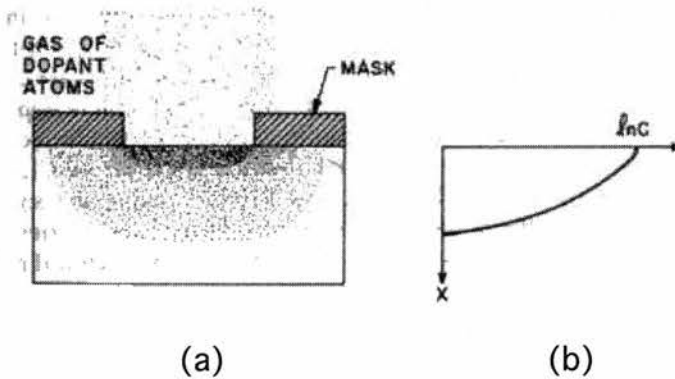


Figure 4.9: (a) Diffusion of atoms from high to low concentration regions. (b) Concentration profile of the diffused dopants, [11].

To accomplish this selective diffusion, the wafer is masked and holes are opened where the diffusion is required, as described in subsection 4.2.1.5. The wafer is then heated to the required temperature in an ambient atmosphere containing the impurities to be diffused (usually in a furnace), and held there long enough for the necessary diffusion to take place. The profile of the dopant distribution is determined mainly by the temperature and diffusion time. The furnace and gas flow arrangements are similar to those used in thermal oxidation.

The introduction of dopant ions into the silicon by means of a high-energy ion beam is

called ion implantation. This can be done at room temperature [4, 12]. The penetration depth is quite small, and unlike diffusion, the maximum concentration is beneath the wafer surface. The depth of the peak concentration increases as the accelerating voltage increases, and the total number of ions injected is proportional to the beam current and implant time. Fig. 4.10 (a) shows the ion implantation technique and in (b) the concentration profile is shown.

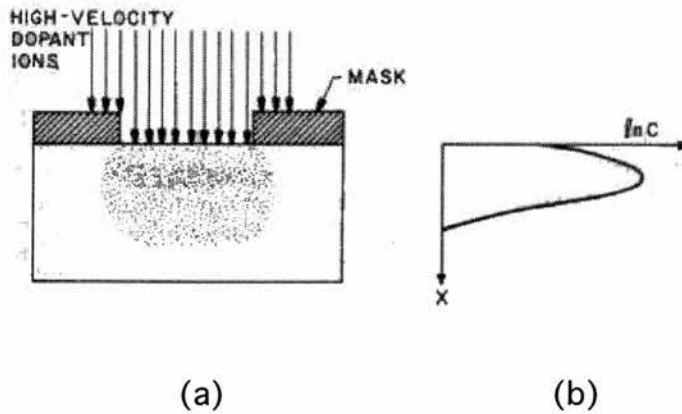


Figure 4.10: (a) Ion implantation for selective introduction of dopants. (b) Concentration profile of the implanted dopants, [11].

The advantages of the ion implantation process with respect to diffusion, is the precise control of the total amount of dopant, the improved reproducibility of the impurity profile, and the low temperature processing. The practical use of diffusion and ion implantation is mainly to change the electrical properties of the substrate. Diffusion is usually used to form a deep junction, while ion implantation is used to form a shallow junction [11].

4.2.4 Etching

In many IC manufacturing steps, whole wafers are completely coated with a layer or layers of various materials such as silicon dioxide, silicon nitride, or a metal. The unwanted material is then selectively removed by etching through a mask to leave, for example, holes in thermal oxide where diffusions are to be made or, long strips of aluminium for electrical interconnects

between individual circuit elements. In addition, patterns must sometimes be etched directly into the silicon surface.

The possible kinds of etching are wet chemical, electrochemical, pure plasma etching, reactive ion etching (RIE), ion beam milling, sputter etching, and high-temperature vapour etching. Wet etching, in which the wafers are immersed in aqueous etching solutions, is the oldest and, when applicable, the least expensive process. Electrochemical etching is done in aqueous-based solutions and has very limited applicability. Plasma etching and combination plasma/RIE, are performed in a low-pressure gaseous plasma, and are most commonly used in fine-geometry applications. Plasma etching generally involves fewer safety hazards and spent chemical disposal problems, but the additional cost of plasma equipment is a deterrent to its use when fine-line definition (less than $3\ \mu\text{m}$) is not necessary. Ion beam milling, is used less often. Sputter etching, done in a relatively low vacuum, is quite slow, produces surface damage, and is usually used only for cleaning surfaces prior to sputtering. Vapour etching generally requires temperatures of the order of 1000°C and is mostly used as an *in situ* clean before epitaxial depositions.

Most IC etching requires material removal in selected regions only and hence requires a series of related processing steps, which are:

1. Coat the wafer with an adhesion promoter and etch-resistant photoresist.
2. Selectively remove the resist to leave the desired pattern.
3. Etch to transfer the mask pattern to the underlying material.
4. Remove (strip) the photoresist and clean the wafer.

All these steps but the 3rd were discussed in the lithography section.

The difference in etch rates (selectivity) between different materials is a very important factor. The individual rate values are also of importance since if the rate is too slow,

the process may not be economically feasible and if it is too fast, the process may not be controllable.

In addition to etch rate, selectivity, and anisotropy, other etchant properties of interest are the effect of the etch on the mask material and the contaminants left behind.

4.2.4.1 Wet Etching

Wet etching in its simplest form consists of a beaker of etchant adjacent to several beakers of rinse water. The wafers are loaded into some an appropriate plastic holder and immersed in the etchant beaker for a specified time. They are then quickly transferred to the first rinse water beaker in order to abruptly stop etching and then moved in sequence to the others.

When considering wet etching it has to be pointed out that depending on the chemical used, the etching could be isotropic or anisotropic. The first one shows no preferential etch rate in any crystal orientation, the latter on the other hand, depends on the crystal orientation.

Isotropic Silicon Etching

Isotropic wet chemical etching began in the late 1950s, and many references can be found, e.g. [13]. Silicon etches that are nonselective with regard to crystallographic orientation and to crystallographic damage, producing smooth surfaces, are primarily based on HF-HNO₃-H₂O mixtures. The etching is a two step process in which the silicon is first oxidised by the nitric acid and then the oxide is dissolved by HF. The etch rate is agitation sensitive and temperature dependent.

During etching of deep, narrow geometries under stagnant conditions, diffusion of reactants into the small openings becomes a major limitation. This is due to the fact that even if the etching action may stop when the next step is reached, it still may continue to etch laterally and give undercutting, as can be seen in Fig.4.11. Since extensive undercutting

generally occurs in wet etching, small geometries are almost always dry etched.

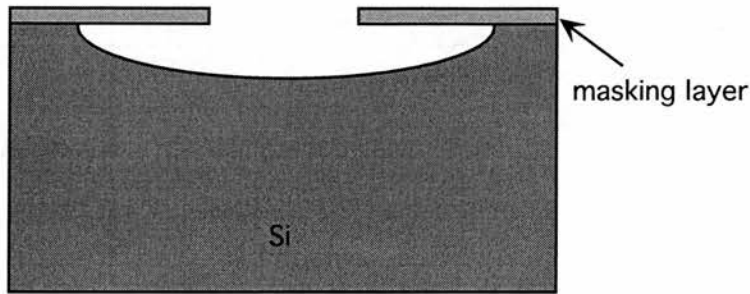


Figure 4.11: Isotropic etching showing undercutting.

Anisotropic Silicon Etching

Anisotropic etching techniques were investigated in the late 1960s [14]. They overcome the problems associated with precision and sensitivity, but are crystal orientation dependent. Anisotropic etchants etch much faster in one direction than in another. The most commonly used is KOH, which slows down markedly in the $\langle 111 \rangle$ planes of silicon, relative to the etch rates for the other planes. This property can be used to form a variety of patterns in a silicon wafer that would be very difficult to achieve in any other manner. The widely used (100) wafers are quite amenable to anisotropic etching. The edges of $\langle 111 \rangle$ planes intersecting a (100) surface make right angles with each other. If a mask with a slot opening in it is oriented azimuthally on the wafer so that the slot edge is parallel to a (111) trace, a trench bounded by $(\bar{1}1\bar{1})$ and $(\bar{1}\bar{1}1)$ planes on the sides can be etched. If etching is allowed to continue to completion, the trench will be V-shaped, with both the width and depth determined by the mask opening. Etching can be stopped earlier, however, leaving a flat-bottomed trench, as can be seen in Fig. 4.12. In this case the depth is a function of the etching time.

When designing the mask for opening a diaphragm using KOH, the anisotropic etch angle through the thickness of the wafer must be taken into consideration. This means that the mask window must be larger than the desired diaphragm, the relationship between etch depth and the increase in diaphragm window size is shown in Fig. 4.13. To obtain a D size of diaphragm, the mask window should be $D + 2X$ where $X = d/\sqrt{2}$ and d is the etch depth.

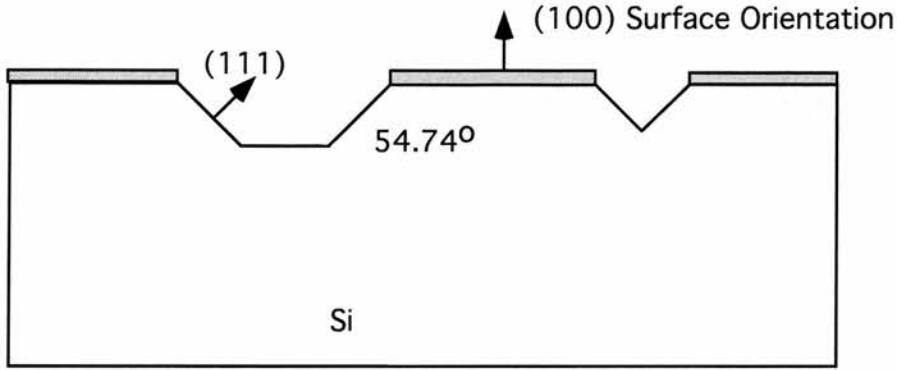


Figure 4.12: Sketch of anisotropically KOH etched silicon.

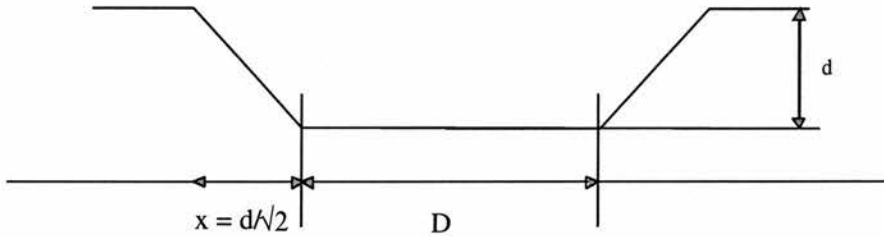


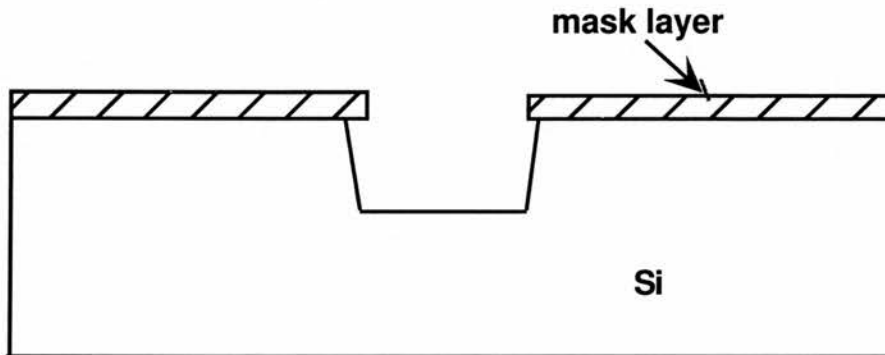
Figure 4.13: Calculation of diaphragm window size.

One of the problems with the bulk micromachining of KOH, is that it is very aggressive and can only be masked using an oxide/nitride masking layer. Even this layer cannot protect polysilicon deposited beneath it. It is usual therefore necessary to perform the bulk micromachining stage as one of the first steps in fabrication, timing it to leave a diaphragm of approximately $20 \mu\text{m}$ thick.

4.2.4.2 Dry Etching

Dry etching, or plasma etching, techniques were developed in the early 1970s [15]. These are orientation and concentration independent. Sputter etching, ion-beam milling, plasma etching and reactive ion etching (RIE) have become alternatives to the conventional wet etching techniques in silicon planar technologies due to the easy control over etch rate and profile, giving rise to the possibility of etching fine features. Their etch rate and etch profile are determined by procedural and instrumental parameters such as, reactant gases, flow rate,

pressure, power density of plasma and bias voltage between the substrate and the plasma [16]. A dry etch profile can be seen in Fig. 4.14



Reactive ion etching

Figure 4.14: The etching profile of RIE.

Energy is supplied by an RF generator. The wafers lie flat on one of the electrodes, and a plasma is generated between the electrodes. Biasing of the electrodes by the DC voltage from the RF generator power supply is excluded by capacitive coupling the RF to the electrode. The chemical species in the plasma are determined by the source gas(es) used. The operating pressure depends on the plasma mode being used and may range from a few Torr to fractions of a milli-Torr.

In plasma etching mode, the electrode areas are symmetrical, and the DC voltage between the plasma and either electrode is the same and relatively small [1]. The various ions and free radicals that are generated in the plasma diffuse to the electrode and wafer surfaces, where they can react with the material being etched to form volatile products that are pumped away.

Reactive ion etching uses a negative self-bias DC voltage developed between the plasma and the wafer electrode to accelerate ions from the plasma to the wafers. An asymmetric DC bias between the plasma and the two electrodes is developed when the two electrodes

have different areas, with the larger voltage being developed on the smaller electrode. Thus, when the electrode on which the wafers rest is deliberately made much smaller than the other electrode, plasma-to-wafer electrode voltages of several hundred volts are readily achievable. In the RIE mode, some etching occurs by free radicals, but more is achieved by ions that are accelerated to the surface. Part of the ion etching is due to the ions chemically reacting at the surface, and part is by physical removal of material when it is struck by the incoming ions.

4.3 Mask Design

To fabricate the cantilevers using the previously described techniques, different masks need to be designed. As a general rule a different mask is needed for each micromachining technique used.

The masks have been designed using the LEdit CAD package which is a specialist mask design package for the semiconductor industry. Areas of a design that are repeated throughout the wafer, for example contact windows and bond pads, can be drawn once in a cell and then this cell placed where required on the design. Any changes to the cell will be repeated throughout the design wherever the cell is used. The use of cells can form hierarchies in the design with cells being used in other cells that are then used in the final design, this design being located in what is called the top cell. Once accustomed to their use it becomes a very powerful tool for the layout of masks.

Since in most cases various masks are needed to fabricate devices in silicon, LEdit has various layers, each available for a particular mask. These layers can be built up and displayed on top of each other thereby ensuring each mask lines up with each other and enabling one to view the design as a whole. Each layer can also be displayed or modified individually and LEdit can support a large number of these layers.

The number of masks needed for the first cantilever batch is eight, one for the diaphragm, one for the required double sided alignment marks, three for the contact windows, one for defining the piezoresistors, one for defining the cantilever paddles, and one for the metallisation. The eight masks used in the fabrication of the first batch of simple cantilever paddles were fabricated at the Southampton University Microelectronics facility.

It was decided to use SOI wafers, with a $3.5\mu\text{m}$ silicon layer on top of the insulator, which is where the cantilevers will be formed. To release the cantilevers the $500\mu\text{m}$ thick silicon, underneath the insulator, must be removed. To do so, some diaphragms need to be anisotropically etched. A mask is needed to open the required windows, which must be larger than the desired diaphragms, as described in subsection 4.2.4. In this case, $3000\mu\text{m}$ long and $800\mu\text{m}$ wide diaphragms were required therefore, $3742\mu\text{m}$ long and $1542\mu\text{m}$ wide windows were drawn.

It is essential that the different masks used in the process align correctly with one another. To achieve this, alignment aids are used with two types being required in this process. The basic type ensures masks used on the same side of the wafer align correctly with one another, as shown in Fig. 4.15.

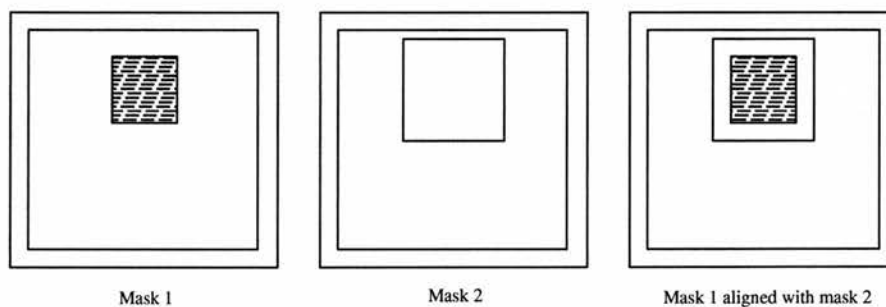


Figure 4.15: Single sided alignment aids.

The double sided alignment aids ensures masks used on different sides of the wafer align correctly with each other. This is required since the process involves working from both sides of the wafer and ensures the resonators are aligned over the diaphragms. The double sided

alignment aid is shown in Fig. 4.16.

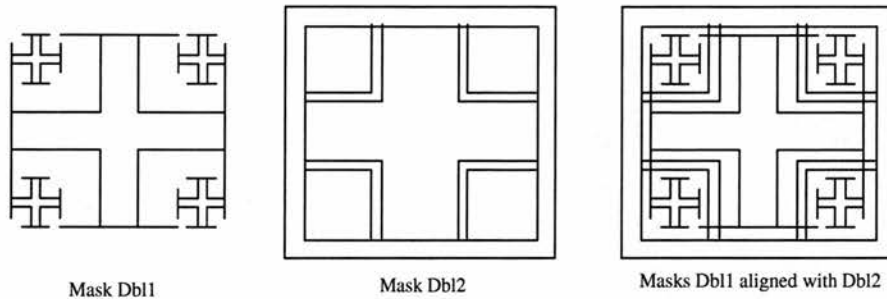


Figure 4.16: Double sided alignment aids.

In the case of the double sided alignment step, the alignment aid first etched on one side of the wafer can be observed by shining infra-red light through the wafer. The second mask is then aligned with the etched marks and when correctly aligned the pattern is exposed onto the wafer.

Since n-type piezoresistance coefficients are higher than p-type for the direction along which the implantation is to be performed, it was decided that the piezoresistors would be n-type. As described in section 5.3, long piezoresistors along the legs of the cantilever and shorter resistors beyond the fixed edge are needed. The piezoresistors were designed so that $5\mu\text{m}$ wide and $67\mu\text{m}$ long, along the legs and $5\mu\text{m}$ wide and $40\mu\text{m}$ long beyond the fixed edge, [17].

The cantilevers were defined according to the theoretical results from Chapter 2. As concluded, the optimal cantilever was a compromise of various parameters - length, thickness, and mass. Therefore, it was decided that for this first prototype, different lengths and different sizes for the paddle would be designed and then experimentally decide which one is most adequate for the application. A selection of different sizes of cantilevers can be seen in Fig. 4.17

Three different masks were design for the contact window. One for doping the piezoresistors, one to open contacts before metallisation, and one for the substrate contact doping.

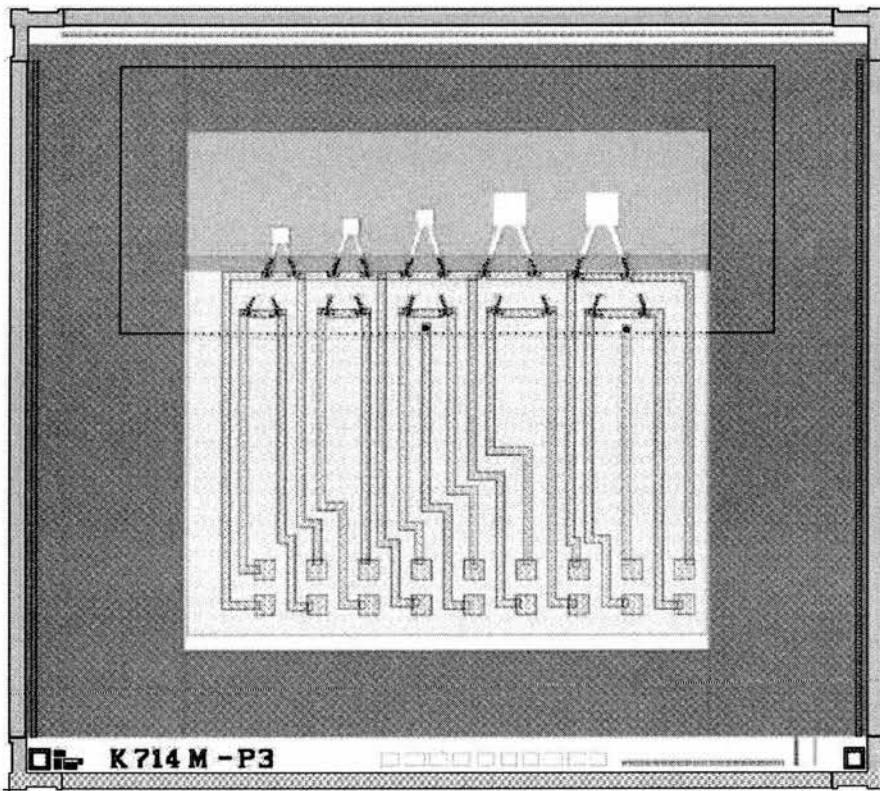


Figure 4.17: Layout of the design. Superposition of all the different layers.

The metal pads and the metal tracks connecting them to the piezoresistor contact windows for electrical connections required another mask.

4.4 Processing of The First Batch

The fabrication method for the first prototype of devices has 88 process steps, which can be grouped into 6 main stages, according to the masks used. The process listing can be found in Appendix B.

- The back etching of the SOI wafer
- The doping of the contact windows
- The implantation of the piezoresistors
- The patterning of the cantilever paddles
- The metal film deposition
- The release of the cantilever paddles

1. Backside Etching of SOI Substrate

First of all, a boron implant is made in the fronts of the wafers, which is followed by an RCA clean of the wafers, after which an initial oxide of 600nm is grown at 1100°C in wet O_2 ambient pressure. This oxide is grown to reduce the stress between the nitride to be deposited and the silicon, and to use as a mask later on in the process. 160 nm of Si_3N_4 is deposited by low pressure chemical vapour deposition (LPCVD) on both sides of the wafers. This silicon nitride is deposited to use as a mask layer when etching in KOH. Windows are opened on the back of the wafers using photolithography and by anisotropically dry etching the silicon nitride and then wet etching the oxide

—the fronts are protected with photoresist. After wet etching the oxide, the remaining photoresist is stripped off, and the wafers are ready to be bulk etched in 440 g/l KOH solution at 85°C. This is to make a diaphragm with a thickness of 20 μm , where the cantilever paddles will be defined. The reason for leaving 20 μm is to give some rigidity to the wafers. A schematic of the first steps can be seen in Fig. 4.18. Finally, the silicon nitride masking layer is etched away in orthophosphoric acid at 160 °C.

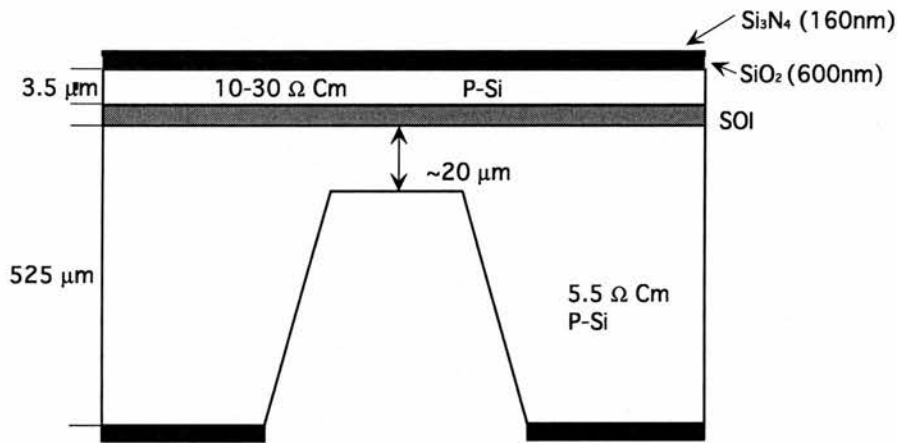


Figure 4.18: Sketch of the back KOH etching of the SOI wafer.

2. Contact Window Doping

After the removal of the silicon nitride, the wafers are cleaned in fuming nitric acid and the required windows are opened by wet etching the silicon oxide after a photolithography step. An n-type impurity, arsenic, is implanted with a dose of $5 \times 10^{15}/\text{cm}^3$ at 80 keV. These windows will be the piezoresistor contact windows.

3. Implantation of the Piezoresistors

The piezoresistors are implanted using an n-type impurity, phosphorus, with a dose of $5 \times 10^{14}/\text{cm}^3$ at 80 keV. This implant is done at the same energy as the contact windows, but the density of the impurity is lower. The reason for a lower density is to achieve the highest strain gauge coefficient.

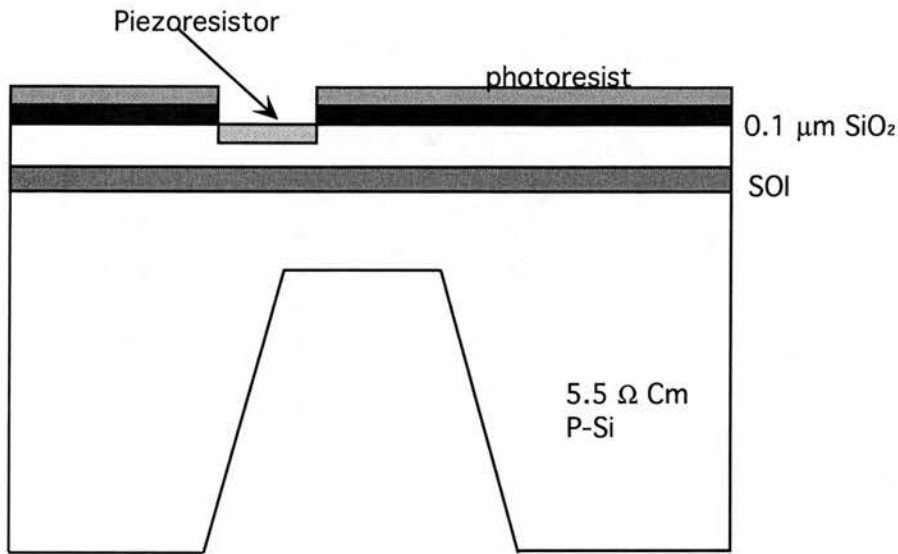


Figure 4.19: Sketch representing the definition of the piezoresistors.

Once the piezoresistors are implanted, the wafers are RCA cleaned and 100nm of oxide is grown at 1000°C . This oxide is necessary so that when the substrate contact doping is implanted the piezoresistors are protected from this new implant. The p-type ion BF_2^+ implanted at 70 keV with a dose of $5 \times 10^{15}/\text{cm}^3$ is used for making a low resistance contact to the substrate. This is needed to prevent the piezoresistors from becoming forward biased and to reduce the resistance when doing the electroplating. A simple sketch representing this stage in the process can be seen in Fig. 4.19

4. Definition of the Cantilever Paddles

After all the implants have been completed and all the remaining oxide is removed, 400 nm of passivation oxide is grown at low temperature, so that all the implants are protected and surface leakage current is prevented. After the low temperature oxide (LTO) is deposited, the wafers are densified, and the implants are driven-in and activated at 1000°C in dry O_2 ambient. This last step also activates the implants. The oxide layer is then patterned and wet etched, giving an oxide mask for the patterning of the cantilever paddles, that are dry etched in the silicon, as shown in Fig. 4.20.

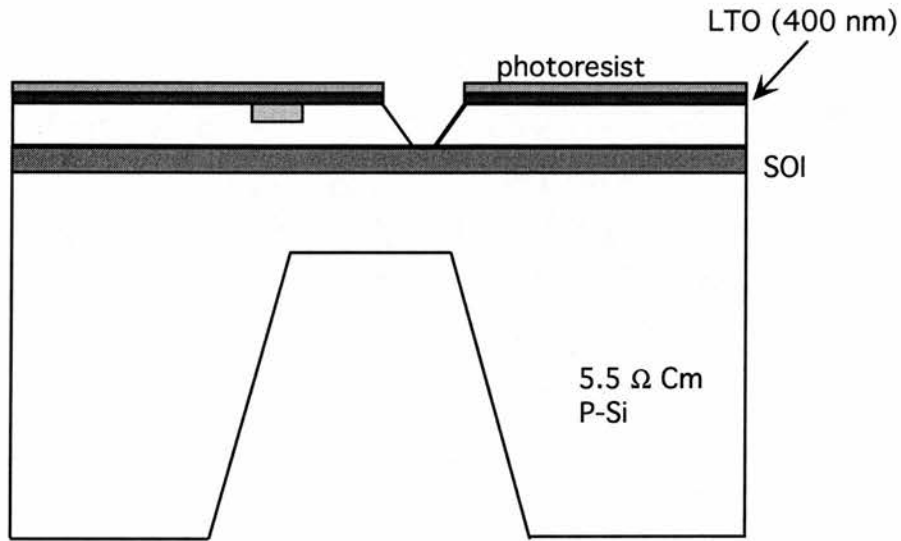


Figure 4.20: Sketch of the dry-etched cantilevers.

5. Deposition of Metal Layers

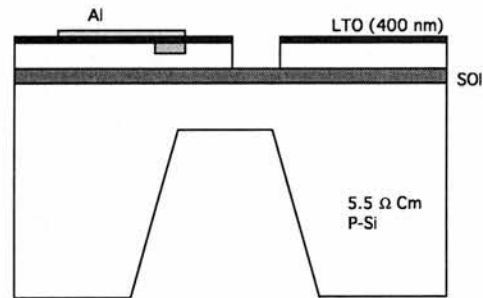


Figure 4.21: Sketch of the metal layer deposition.

Before the deposition of the metal, the contact windows must be opened, as at this stage they are protected by the oxide layer. Having done this, the wafers are dip etched in 20:1 BHF in order to remove any native silicon oxide and to allow good contact between the metal and the substrate or resistors. 100 nm of Ti and 1000 nm

of Al/Si are sputtered, patterned and wet etched. A cross section of the structure can be seen in Fig. 4.21. After the photoresist is stripped off, the metal layer is alloyed for 30 minutes at 350 °C in H₂/ N₂ ambient. This alloy/anneal is done to reduce the contact resistance.

6. Release of the Cantilever Paddles

The fronts of the wafers are protected with photoresist in order to etch the remaining silicon from the backs by RIE up to the SOI layer, after which the oxide layer is anisotropically dry etched, also by RIE. The release of the cantilever paddles is shown in Fig. 4.22.

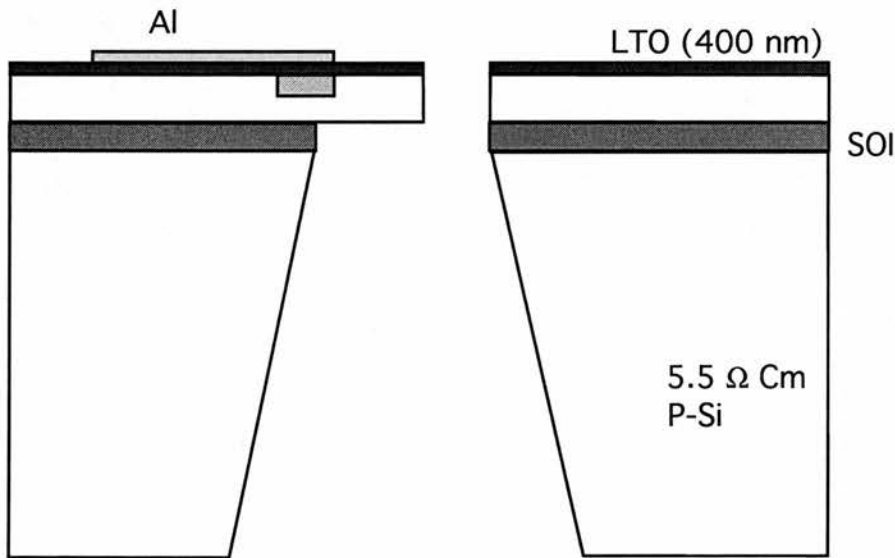


Figure 4.22: Cross-section of the final device.

An SEM picture of cantilevers with piezoresistors can be seen in Fig. 4.23.

4.5 Conclusions

The mechanical and electrical properties of silicon, together with the well known IC technology and micromachining techniques described here, made silicon the substrate of choice

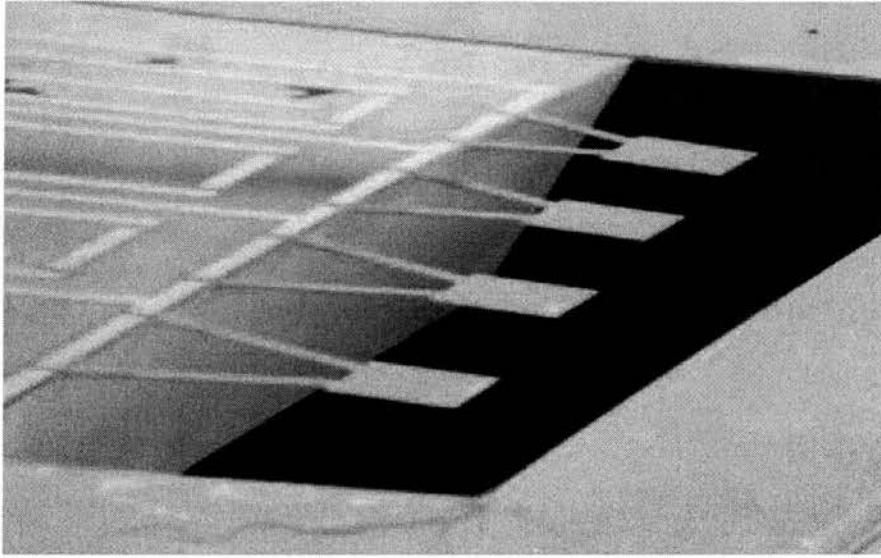


Figure 4.23: A SEM photo of the completed cantilevers.

for this project.

The design of the cantilever paddles was performed after a thorough study of the theoretical properties. The theory only predicted a compromise between the different parameters for the optimisation of cantilevers hence, a variety of different dimensions were designed.

No major problems were encountered through the processing of the wafers, leading to a successful completion of the batch.

References

- [1] W.R. Runyan and K.E. Bean , *Semiconductor Integrated Circuit Processing Technology*, Addison Wesley, (1990).
- [2] M.V. Whelan *et al.*, 'Residual Stress at an Oxide-Silicon Interface', *Appl. Phys. Lett.* **10**, 262-264, (1967).
- [3] E.A. Irene *et al.*, 'A Viscous Flow Model To Explain the Appearance of a High Density Thermal Oxide at Low Temperatures', *J. Electrochem. Soc.* **129**, 2594-2597, (1982).
- [4] S.M. Sze , *VLSI Technology*, McGraw-Hill, (1983).
- [5] R.S. Rosler, 'Low Pressure CVD Production Processes for Poly, Nitride and Oxide', *Solid State Technol.* **20**, 63, (1977).
- [6] W. Kern and R.S. Rosler, 'Advances in Deposition Processes for Passivation Films', *J. Vac. Sci. Technol.* **14**, 1082, (1977).
- [7] R.E. Logar *et al.*, 'Low Pressure Deposition of Phosphorous-Doped Silicon Dioxide at 400°C in a Hot Wall Furnace', *Chemical Vapor Deposition—Sixth International Conference*, Electrochemical Society, Princeton, N.Y. 195-202, (1977).
- [8] N. Goldsmith and W. Kern, 'The Deposition of Vitreous Silicon Dioxide Films from Silane', *RCA Review*, **28**, 153-165, (1967).

- [9] K. Strater and A. Mayer, 'The Oxidation of Silane, Phosphine, and Diborane During Deposition of Doped-Oxide Diffusion Sources', *Semiconductor Silicon*, Electrochemical Society, New York, (1969).
- [10] R.C. Henderson, 'Silicon Cleaning with Hydrogen Peroxide Solutions: A High Energy Electron Diffraction and Auger Electron Spectroscopy Study', *J. Electrochem. Soc.* **119**, 772-775, (1972).
- [11] S.M. Sze, *Semiconductor Devices, Physics and Technology*, Wiley Inter-Science, New York, (1985).
- [12] I. Brodie and J.J. Murray, *The Physics of Microfabrication*, Plenum, New York, (1982).
- [13] H. Robbins and B. Schwartz, 'Chemical Etching of Silicon', *J. Electrochem. Soc.* **106(6)**, 505-508, (1959).
- [14] D.B. Lee, 'Anisotropic Etching in Silicon', *J. Appl. Phys.* **40**, 4569-4574, (1969).
- [15] S.M. Irving *et al.*, 'Gas Plasma Vapor Etching Process', U.S. Patent 3,615,956 (1971).
- [16] R.G. Poulsen, 'Plasma Etching in Integrated Circuit Manufacture - a Review', *J. Vac. Sci. Tech.* **14**, 266-274, (1977).
- [17] Y. Su, *et al.*, 'Fabrication of Improved Piezoresistive Silicon Cantilever Probes for the Atomic Force Microscope', *Sensors and Actuators A*, **60**, 163-167, (1997).

Chapter 5

Preliminary Experimental Results on the Microfabricated Cantilevers

5.1 Introduction

This chapter discusses the driving and detection mechanism for the cantilevers fabricated as described in the previous chapter. A direct mechanism has a better performance than an indirect mechanism therefore it was decided to use a magnetic field to directly drive the cantilevers. The magnetic field can be used both in force and torque mode, both are studied in depth resulting in the choice of force mode. This chapter describes the construction and characterisation of the electronic system for detecting the change in resistance of the piezoresistors used in the detection system. The results gained from the test are detailed and conclusions drawn regarding the experimental results when compared to the FEA.

5.2 Magnetic Excitation

The driving mechanism required to oscillate the cantilever is one of the key parameters in optimising the sensitivity. As described in Chapter 1 an indirect excitation is commonly used since it is often mechanical in nature, e.g. acoustically [1, 2]. However this has several disadvantages. When the cantilever is indirectly driven, several modes are excited at the same time, which makes it more difficult to measure the resonant frequency.

This problem is minimised if the driving force is directly applied to the cantilever. This can be realised by applying a magnetic field to a magnetic coating or a magnetic particle fixed on the cantilever [3, 4]. As described in Chapter 1, such magnetically driven cantilevers demonstrate several advantages compared to the indirect driving mechanism [4]. On the one hand the response of the cantilever is simpler and no mixed modes appear [5], and on the other hand, the signal-to-noise ratio improves substantially, especially in fluids [4, 6, 7].

Hence, a magnetic excitation was chosen to drive the cantilevers. Torque and force mode were considered, as well as an optimisation of the magnetic field generating coil.

5.2.1 Optimisation of Coil Geometry

The simplest way to produce a uniform magnetic field is in a long thin solenoid. If the solenoid has N turns wound on a former of length L and carries a current i , the field inside it will be,

$$\bar{H} = \frac{Ni}{L} = ni \quad (5.1)$$

where n is defined as the number of turns per unit length. However, inside the solenoid there is no gradient, which requires a study of the field outside the solenoid.

In order to produce high field strengths from a solenoid, it eventually becomes more effective to increase the number of windings per unit length N/L than to increase the coil current. This is because the Joule heating is proportional to I^2 whereas the field is proportional to i . Therefore, if the current is doubled in a coil of fixed resistance the Joule heating is quadrupled, while, if the number of windings is doubled the Joule heating is only doubled. Both methods will result in a doubling of the magnetic field. Therefore solenoids are often wound with several layers of windings and hence are no longer 'thin'. That is, the radii of the inner and the outer windings are no longer equal or even close to being equal. In the case of these thick solenoids, the calculation of the magnetic field is more complicated.

To design the optimal coil, it is necessary to know the axial field of a finite solenoid, outside the solenoid, which can be obtained by integrating the field due to a thin shell solenoid over the range of radii. This at the same time can be obtained by integrating over the distance along the axis to each current loop.

5.2.1.1 On-Axial Field Due to a Current Loop

The simplest formula uses the Biot Savart law, integrated over a circular loop to obtain the magnetic field at any point along the axis of the loop [8], leading to,

$$\bar{H} = \frac{ir^2}{2(r^2 + x^2)^{3/2}} \quad (5.2)$$

where x is the distance on axis, from the centre of the current loop, in meters, r is the radius of the current loop, in meters, i is the current in the wire, in amperes, and \bar{H} is the magnetic field, in teslas, at any point on the axis of a current loop. A cross-section of the loop can be seen in Fig. 5.1.

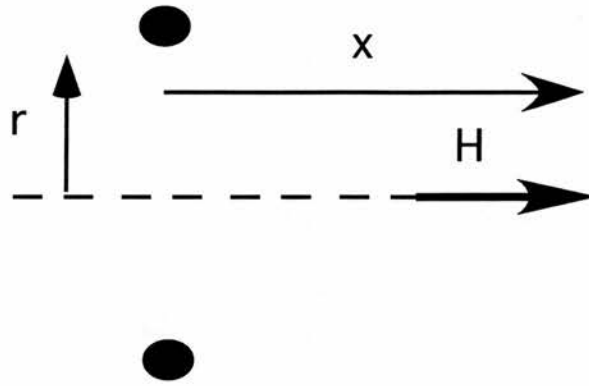


Figure 5.1: A sketch of a current loop in cross-section view.

5.2.1.2 Axial Field of a Finite, Thin Shell Solenoid

The next step to determine the magnetic field of a coil, or thick solenoid, is to determine the field of a thin solenoid, which can be achieved by integrating over a range of displacements of the field due to a current loop, to obtain the magnetic field at any point on the axis of a finite, thin shell solenoid. The cross-section of such a solenoid can be seen in Fig. 5.2

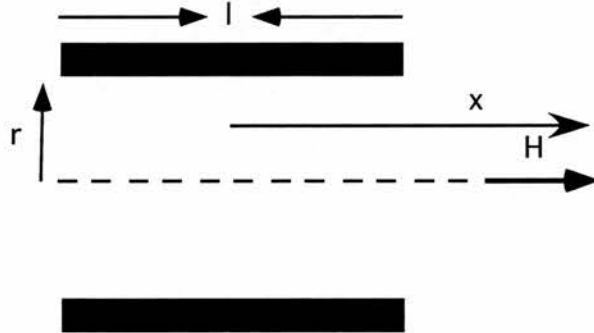


Figure 5.2: A sketch of a thin shell solenoid in cross-section view.

Hence, the \bar{H} , in Teslas, at any point on the axis of the solenoid is described by,

$$\bar{H} = \frac{iN}{2l} \left[\frac{x + l/2}{\sqrt{(x + l/2)^2 + r^2}} - \frac{x - l/2}{\sqrt{(x - l/2)^2 + r^2}} \right] \quad (5.3)$$

where x is the distance, on axis, from the center of the solenoid to the magnetic field measurement point, in meters.

5.2.1.3 Axial Field of a Finite Solenoid

Finally, integrating the field due to a thin shell solenoid over a range of radii, the magnetic field at any point of a finite solenoid is obtained. Fig. 5.3 shows the cross-section of a coil.

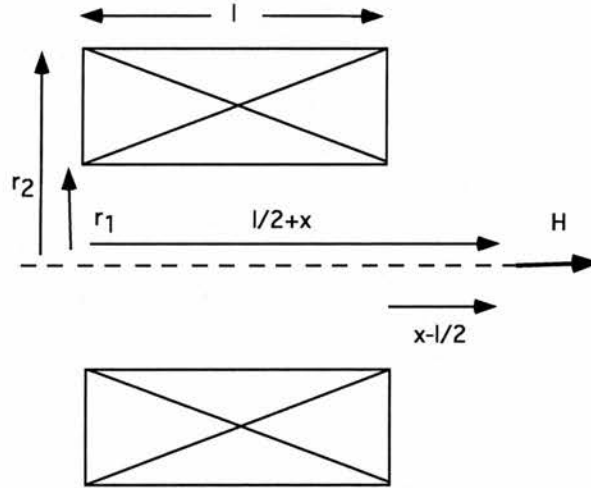


Figure 5.3: A sketch of a coil in cross-section view.

The required magnetic field is then,

$$\bar{H} = \frac{in}{2(r_2 - r_1)} \left[(x+l/2) \ln \frac{\sqrt{r_2^2 + (x+l/2)^2} + r_2}{\sqrt{r_1^2 + (x+l/2)^2} + r_1} - (x-l/2) \ln \frac{\sqrt{r_2^2 + (x-l/2)^2} + r_2}{\sqrt{r_1^2 + (x+l/2)^2} + r_1} \right] \quad (5.4)$$

where r_1 is the inner radius of the coil and r_2 is the outer radius of the coil.

Often it is necessary to consider the limitations imposed by the available power supply, which will give maximum field. Clearly, the impedance or resistance of the coil should be chosen to operate as close to the current and voltage limitations of the supply as possible.

That is, the optimum resistance R_{opt} should be,

$$R_{opt} = \frac{V_{lim}}{i_{lim}}. \quad (5.5)$$

It was originally demonstrated by Fabry [9] that the field can be written in terms of the power as:

$$\bar{H} = \sqrt{\frac{P\lambda}{r_1\rho}} G \quad (5.6)$$

where all the geometrical terms have been collected together in a single expression $G(\alpha, \beta)$ known as the 'geometrical factor'.

Two parameters can be defined, α and β , which describe the geometrical properties of the coil,

$$\alpha = \frac{r_2}{r_1} \quad (5.7)$$

and

$$\beta = \frac{l}{2r_1}. \quad (5.8)$$

Therefore, the geometrical factor is,

$$G = \sqrt{\frac{1}{2\pi\beta(\alpha^2 - 1)}} \left[(\gamma + \beta) \ln \frac{\alpha + \sqrt{\alpha^2 + (\gamma + \beta)^2}}{1 + \sqrt{1 + (\gamma + \beta)^2}} - (\gamma - \beta) \ln \frac{\alpha + \sqrt{\alpha^2 + (\gamma - \beta)^2}}{1 + \sqrt{1 + (\gamma - \beta)^2}} \right] \quad (5.9)$$

where $\gamma = \frac{x_1 + x_2}{2r_1}$.

And λ is the so called filling factor which is defined as,

$$\lambda = \frac{\text{active section of the winding}}{\text{total section of the winding}} \quad (5.10)$$

ρ is the specific resistivity of the material used for the coil and r_1 is the inner radius.

The examination of the geometrical factor contours for uniform current density coils reveals a maximum ($G=0.179$) near $\alpha = 3$ and $\beta = 2$ [10]. A coil with $\alpha = 3$ and $\beta = 2$ will

produce the highest field with the lowest power. The fact that there should be an optimum geometry can be qualitatively predicted as follows. Given a certain number of ampere-turns, indicates that the smaller the radii, the more field is generated per ampere turn. However, unless the loops are spread over an adequate cross-section, excessive power would be required to drive the current. For the case of uniform current density, $\alpha = 3$ and $\beta = 2$ represents the optimum compromise between these conflicting requirements.

5.2.2 Torque Mode

The torque due to the force a magnetic field produces on a magnetic moment is [8],

$$\tau = \mu_0 \bar{\mu} \times \bar{H} \quad (5.11)$$

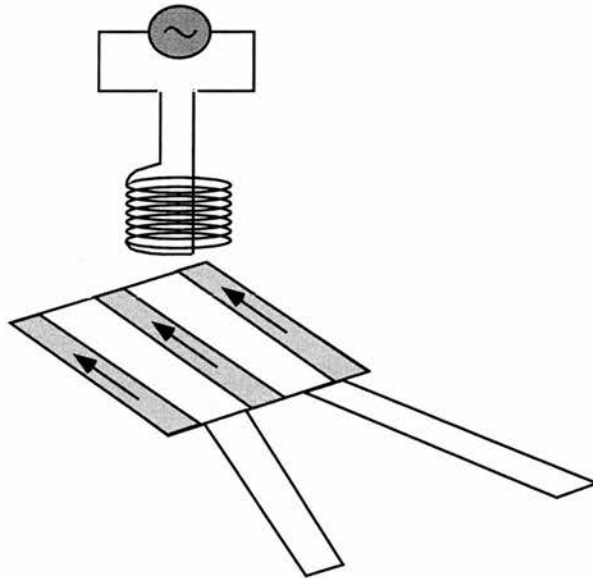


Figure 5.4: A sketch of a coil inducing a magnetic torque onto the cantilever.

This means that the magnetic field \bar{H} tries to align the moment \bar{M} so that it lies parallel to the field. In our case, if we had a thin magnetic layer on the paddle, and were to apply a magnetic field in torque mode, this would excite the cantilever in the z direction as can be

seen in Fig. 5.4.

At this point it is easy to see that the magnitude of the applied torque is directly proportional to the magnetic field \vec{H} . Therefore, the applied torque will be maximum at the point where \vec{H} is maximum, and that's in the centre of the coil, as can be seen from the graph of \vec{H} versus the distance in Fig. 5.5.

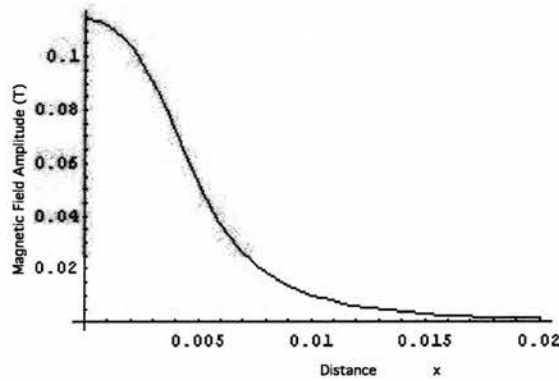


Figure 5.5: Magnetic Field versus distance.

5.2.3 Force Mode

The force due to the magnetic field is [8],

$$\vec{F} = -\bar{\mu}\nabla\vec{H} \quad (5.12)$$

Assuming that the cantilever is aligned exactly with the centre of the coil, from symmetry it can be deduced that the only term of the gradient which is not zero is $\partial H/\partial x$, as can be seen in Fig. 5.6.

In this case the magnetic moment and the field must lie parallel, and hence, a high aspect-ratio magnetic particle is needed.

The force applied on the magnetic particle has to be maximised. As the force is propor-

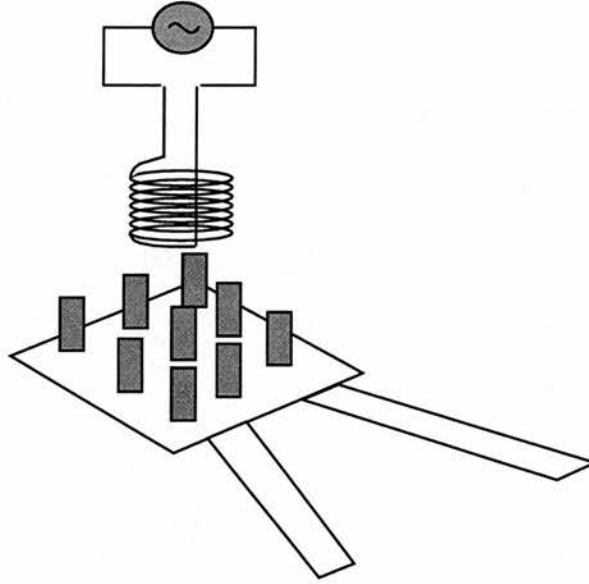


Figure 5.6: A sketch of cantilever excited in the force mode.

tional to the gradient of the magnetic field, the gradient has to be maximised. In Fig. 5.7 can be seen that the maximum gradient is at $0.5x_l$ from the coil centre.

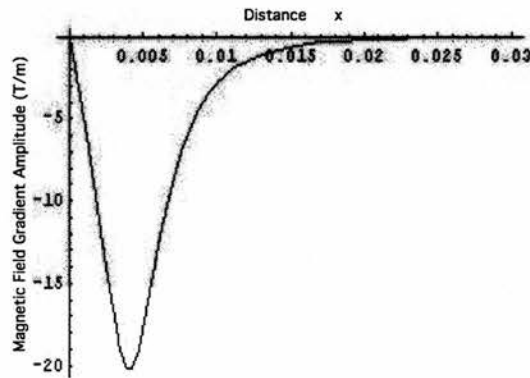


Figure 5.7: The magnetic field gradient versus distance.

Therefore, the cantilever needs to be placed outside the coil but very close to the coil for the force to be maximum.

5.2.4 Summary of Driving Mechanism

From the previous study it can be concluded that the best excitation mechanism is the magnetic force mode. The torque mode would imply bigger coils which would be incompatible with the μ TAS technology.

The force mode requires a good alignment of the cantilever with the coil, high-aspect-ratio particles and working close to the coil.

5.3 Piezoresistive Detection

Difficulties in detecting the signal can occur depending on the detection system. In the case of optical detection (as described in Chapter 1), if the optical beam has to pass several interfaces an attenuation of the signal could occur, or even phase changes. Alternatively, piezoresistive detection can be used. The deflection of the cantilever results in a change of the piezoresistance and can be read out directly in a Wheatstone bridge. This removes the complications of detecting cantilever movement under fluids, although absolute sensitivity is less than on optical system.

5.3.1 Wheatstone Bridge

Wheatstone bridges are commonly used in strain gauges to allow the small changes in resistance to be more easily measured. In this case the bridge will be driven by AC rather than DC to enable changes of 2 parts per million to be seen and measured.

Wheatstone bridges are made from 4 similar value resistors connected together as shown in Fig. 5.8. Typically the bridge is powered by a DC voltage at V_{in} . As the resistor values are nominally the same, the voltage across the output is normally small. A change in the

values of any resistors will cause a change in the output voltage V_{out} .

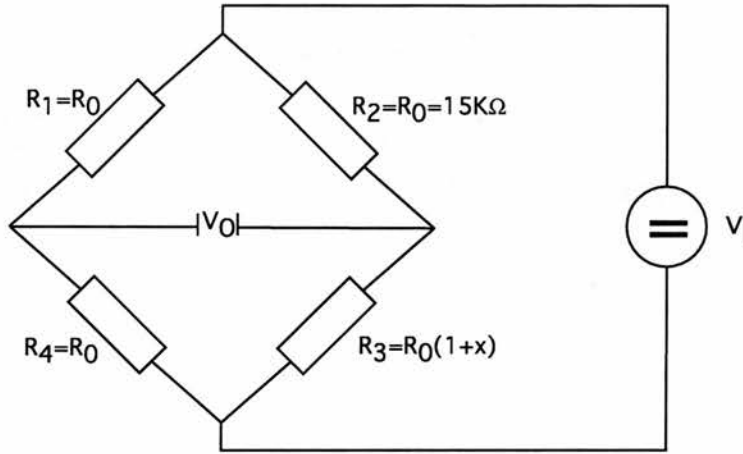


Figure 5.8: A sketch of a simple Wheatstone bridge, where R_3 represents the piezoresistor, and x is the fractional change in resistance produced in the piezoresistor.

Following the notation from Fig. 5.8, if $x = 0$, then for a balanced bridge the balanced condition can be defined as,

$$\frac{R_1}{R_4} = \frac{R_2}{R_3} \quad (5.13)$$

If the measure taken is the voltage, the equation for the bridge is,

$$V_{out} = V_{in} \left(\frac{R_3}{R_2 + R_3} - \frac{R_4}{R_4 + R_1} \right) \quad (5.14)$$

This bridge arrangement also has the advantage that it can discriminate against any temperature related change in resistance. The overall resistance will be a combination of stress-induced resistance due to the deflection and an additional resistance variation due to the temperature. This temperature variation can be compensated with another piezoresistor, which will suffer the same temperature variation but no displacement, both in the same arm of the bridge, as shown in Fig. 5.9.

With this arrangement, and solving Eq. 5.14, the following simple expression is obtained

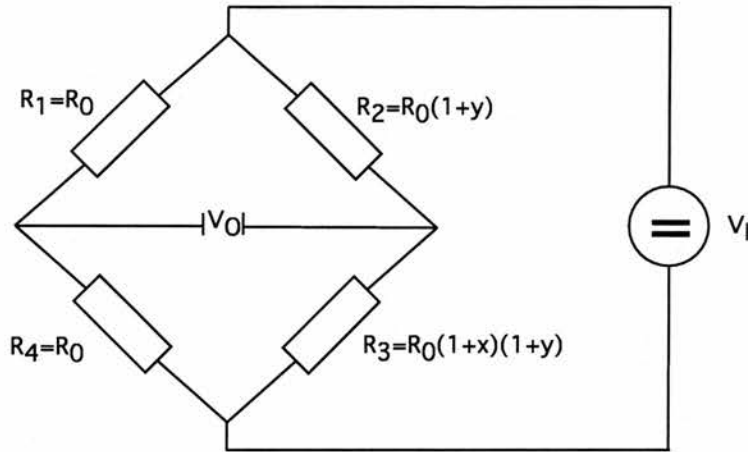


Figure 5.9: A sketch of Wheatstone bridge for the compensation of temperature by means of a passive piezoresistor, where y represents the change in temperature and/or any other change.

for V_{out} ,

$$V_{out} = \frac{V_{in}}{2} \frac{x}{x+2}. \quad (5.15)$$

The accuracy of measurements taken with this arrangement of resistors depends on the accuracy with which V_{out} can be measured. Unfortunately, if V_{out} is in the region of μV , there are a number of difficulties in making this measurement accurately. The input impedance of a measuring operational amplifier would need to be very high to avoid loading the circuit and the input offset voltage would need to be very small. Under these circumstances the noise can also become a problem and special care will have to be taken to avoid thermocouple effects.

By driving the Wheatstone bridge with an AC voltage rather than a DC voltage, a number of these problems are resolved. The input offset voltage of the amplifier is now not a problem, and thermocouple effects can be neglected. The problem which now arises is to be able to measure accurately the AC signal produced by the bridge. To solve this problem a lock-in amplifier is used (see Fig. 5.10).

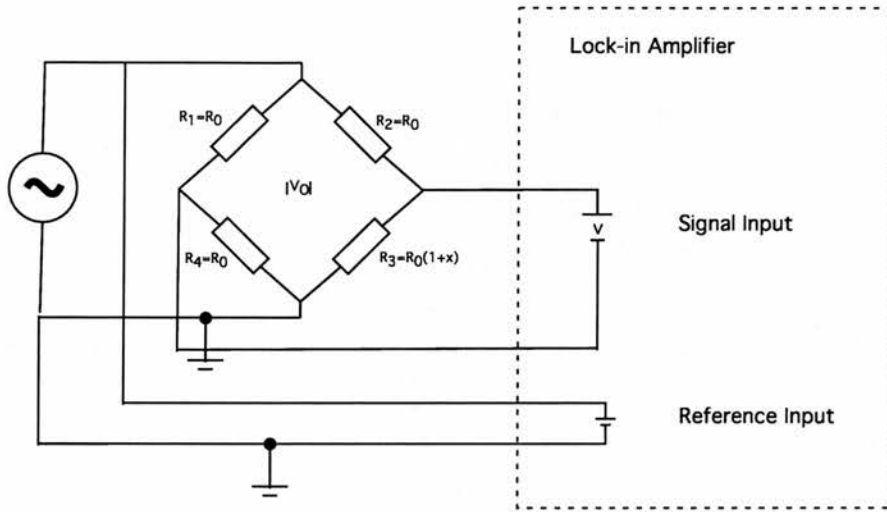


Figure 5.10: A sketch of Wheatstone bridge driven by an AC voltage.

As the circuit is driven at a chosen frequency, it is possible to remove all noise at any other frequency through the lock-in amplifier process. In particular, DC errors are resolved and AC noise input such as 50 Hz mains are eliminated.

Nevertheless, when driving the Wheatstone bridge with a sine wave type signal, an extra complication is introduced. As the drive is AC, any imbalance in the capacitive or inductive values of the bridge network will cause phase shifts in the bridge output relative to the drive voltage. This behaviour is best illustrated with a description of the actual experiment, which is described in section 5.4 later on in this chapter.

5.3.2 Noise in Piezoresistors

Noise is present in all electronic circuits and is important because it specifies a lower limit to the sensitivity of the devices. Existence of shot noise is basically due to the fact that electrical charge is not continuous, but is carried in discrete amounts equal to the electron charge. Some forms of noise, such as that caused by extraneous pick-up of external man-made signals can be reduced or eliminated by filtering and by paying attention to wiring and parts location. Other forms of noise, on the other hand, are unavoidable as they are the

result of charge flowing through the components of the circuits.

Piezoresistive sensors have two main noise sources, both easily distinguishable on a typical noise spectrum vs. frequency, as shown in Fig. 5.11. At low frequencies, all resistors suffer from $1/f$ noise, usually dominated by conductance fluctuations, that is, the noise power density [V^2/Hz] decreases as one over the frequency. In addition to this, there is Johnson noise, which is independent of frequency, and is represented on a frequency spectrum plot as an horizontal line. Johnson noise is fundamentally due to thermal energy in a resistor, and the fundamental cause has long been well understood [11].

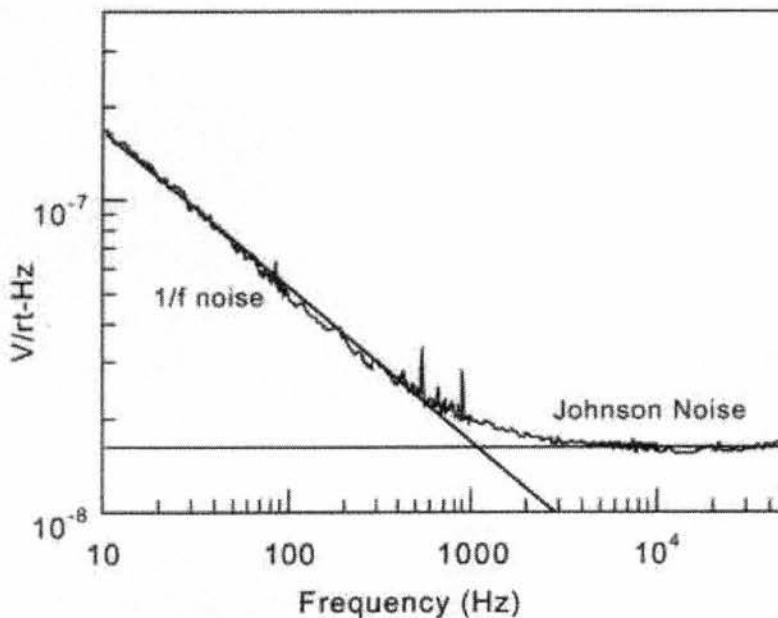


Figure 5.11: Typical measured cantilever noise spectrum showing Johnson and $1/f$ noise. Typical cantilevers transition from $1/f$ to Johnson noise is in the low hundreds of Hertz.

On the other hand, $1/f$ noise can have a number of underlying causes, and despite the fact that it is the dominant noise source for most piezoresistors, it has not been properly included in a piezoresistor analysis. $1/f$ is created by the effect of resistance fluctuations when an externally applied current flows through a resistor, and is heavily dependent upon

the construction of the resistor involved.

5.3.2.1 Johnson Noise

J. B. Johnson first analysed the noise voltage that appears across the terminals of a resistor due to free electrons moving in thermally excited motion. This noise is known as thermal, white or Johnson noise. Thermal noise is due to the thermal motion of electrons in resistors and is unaffected by the presence of a current. Therefore, the Johnson noise is related to absolute temperature, and as temperature approaches to zero, so will do the thermal noise.

Any resistor sat on a bench will generate a noise voltage across its terminals that will have a flat frequency spectrum, which voltage generated by a resistance R at a temperature T is given by,

$$V_{noise}(rms) = \sqrt{(4k_B T R \Delta f)} \quad (5.16)$$

where K_B is the Boltzmann's constant, and Δf is the measurement bandwidth.

Although the Johnson noise varies as \sqrt{R} , minimising R is not the way to proceed, since the sensitivity of the piezoresistors also vary as \sqrt{R} [12], as described in Eq. 5.17

$$\frac{\Delta R}{R}(Johnson) = \frac{4\sqrt{k_B T R \Delta f}}{V} \quad (5.17)$$

where R and ΔR are the resistance and its change under strain, and V is the biased voltage. Since both the sensitivity and the noise varies as \sqrt{R} , the Johnson noise due to high resistances could be compensated by an increased bias voltage, but this will cause an increase in current or heating, which increases shot noise and $1/f$ noise. The minimum value of R should be high enough to exceed the voltage noise of the first stage of amplification.

5.3.2.2 1/f Noise

In 1969, F. N. Hooge [13] explained the empirical observation that the 1/f noise spectral density of an homogeneous resistor is dependent on the total number of carriers in the resistor, according to,

$$S_H = \frac{aV_B^2}{Nf} \quad (5.18)$$

where N is the total number of carriers, f is the frequency, V_B is the bias voltage, and a is a dimensionless parameter, which for an implanted resistor has been found to vary depending on the annealing [14].

If Eq. 5.18 is integrated from f_{min} to f_{max} , then the voltage noise power is,

$$\overline{V_H^2} = \frac{aV_B^2}{N} \ln\left(\frac{f_{max}}{f_{min}}\right) \quad (5.19)$$

Note that for any decade of frequency, the integrated 1/f noise is constant. The total noise between 1Hz and 10 Hz is the same as that between 1 KHz and 10 KHz. Although the bandwidth is much greater in the latter case, the noise level is therefore correspondingly less.

For a constant doping concentration, the number of carriers is proportional to the volume of the resistor. Hence, the 1/f noise is inversely proportional to the cantilever volume. 1/f is not dependent on the resistance since a long thin resistor with high resistance can have the same number of carriers as a short, wide, low resistance one.

5.3.2.3 Thermo-Mechanical Noise

In gases at normal pressures or in liquids, the small moving parts are specially susceptible to mechanical noise resulting from molecular agitation. If the cantilever is intended for low-level signals, this thermo-mechanical noise can be the limiting noise component.

One of the more well known mechanisms for thermo-mechanical noise is the Brownian motion. Here, the agitation of an observable is caused by molecular collisions from a surrounding gas or liquid and the agitation is directly related to the fluid's viscosity [15]. In fact, any molecular agitation, even through solid structures like springs and supports, can cause random motion of an object. It is often assumed that the preamplifier noise dominates the sensor noise floor [16]. Nevertheless, in the case of microminiature cantilevers, for which the thermo-mechanical noise can be important, the noise can be dominated by thermo-mechanical noise.

In practice, there are two tools to analyse equilibrium fluctuations [17], The Equipartition Theorem and the Nyquist Relation. According to the Equipartition Theorem [18], the mean-square displacement of a mass-spring oscillator resulting from thermal agitation is,

$$\frac{1}{2}k\langle x^2 \rangle = \frac{1}{2}k_B T \quad (5.20)$$

where $\langle x^2 \rangle$ is the average of the spectral density over all frequencies, and k is the force constant.

The Nyquist's Relation [18], gives the spectral density of the fluctuating force related to any mechanical damping,

$$F = \sqrt{4k_B T b \Delta f} \quad (5.21)$$

where b is the mechanical damping.

This is a direct analog of Johnson noise related to electrical resistance [17].

In the non-resonant case, much below or above than ω_0 , the amplitude of the noise displacement becomes,

$$y_{thermo} = \sqrt{4k_B T b} \frac{1}{k} \quad (5.22)$$

where k is the cantilever spring constant. Eq. 5.22 can be expressed in terms of Q since $Q = \omega_0 m / b$, where m is the mass of the cantilever. Rewriting in terms of the frequency and the force constant, the damping factor can be expressed as $b = k / \omega_0 Q$,

$$y_{thermo} = \sqrt{4k_B T / \omega_0 k Q}. \quad (5.23)$$

And at resonance the amplitude of the noise displacement becomes [19],

$$\begin{aligned} y_{thermo} &= \sqrt{4k_B T b} \frac{Q}{k} \\ &= \sqrt{4k_B T Q / \omega_0 k} \end{aligned} \quad (5.24)$$

From which it can be seen that the noise displacement not only depends on the thermal energy but also on the Q of the system, and it is inversely proportional to the square root of the resonant frequency and the spring constant.

5.3.3 Sensitivity

Having done a study on the possible noise sources, now it is possible to determine which of these limits the sensitivity of the cantilevers. As it has already been pointed out, the $1/f$

noise is only present at very low frequencies. To determine whether the piezoresistor's Johnson noise or the thermo-mechanical noise is the limiting factor, the theoretical characteristics of the devices will be calculated.

The limiting factor for the piezoresistors is the Johnson noise, so the minimum detectable change in the piezoresistors is found by considering Eq. 5.17 and substituting the theoretical values, $k_B = 1.38 \cdot 10^{-23} J/K$, $R = 15 K\Omega$, $T = 300 K$, $\Delta f = 10.000 Hz$ and the Wheatstone biased voltage $V = 4V$,

$$\left(\frac{\Delta R}{R}\right)_{Johnson} \propto 10^{-7} \quad (5.25)$$

Now, considering that the sensitivity of the piezoresistor is given by Eq. 2.40, which with the values of $E = 1.5 \times 10^{11} N/m^2$, $\pi_l = 45 \times 10^{-11} m^2/N$, $t = 3\mu m$, $L_1 = 400\mu m$, $L = 200\mu m$, $\omega = 40\mu m$, and $\beta = 0.58$, becomes,

$$S = \beta \frac{3\pi_l E t L_1}{2(L_1^3 - L^3 + 2\omega L^2)} = 2209 m^{-1} \quad (5.26)$$

Therefore, the minimum detectable displacement is,

$$y = \frac{\Delta R}{S} = 4.5 \times 10^{-11} m \quad (5.27)$$

On the other hand, the displacement due to the thermo-mechanical noise is described by the Eq. 5.24, which considering that $k = 1.36 N/m$, $\omega_0 = 11000 Hz$, and $Q = 100$ it becomes,

$$y_{thermo} = 1.05 \times 10^{-11} m \quad (5.28)$$

which is slightly smaller than the displacement measurable by the resistors.

From the discussion above, it can be concluded that the dominant noise source is the Johnson noise in the resistors.

5.4 Experimental Set-up and Electronic Considerations

In order to resonate the cantilevers using a magnetic force, a magnetic moment perpendicular to the cantilever surface is needed. The cantilevers fabricated so far, as explained in Chapter 2, are plain cantilevers in the sense that they have no ferromagnetic particles on them. Therefore, a high aspect ratio iron cylinder is attached to the paddle with the aid of a microscope and some micromanipulators.

The sinusoidal magnetic field is induced by a coil placed close to the magnetic particle. The coil is design to possess well defined gradients so that the magnetic dipole will experience a force perpendicular to the plane of the paddle, as explained in Section 5.2. The input of this coil is a sinusoidal current generated by a lock-in amplifier.

The piezoresistors, placed at the base of the cantilevers, will experience a large strain when vibrating at resonant frequency. The Wheatstone bridge which detects this change in the piezoresistors is also driven by the same sinusoidal signal as the coil. The Wheatstone bridge consists of an external $10K\Omega$ resistor and a potentiometer in one of the arms, and the other arm is an internal resistor (which is under exactly the same conditions as the cantilever's piezoresistor, except for the strain) and the cantilever piezoresistor. The potentiometer is used to balance the bridge prior to measurements. The output of the bridge is detected by the lock-in amplifier and recorded in a computer. The set-up is shown schematically in Fig. 5.12.

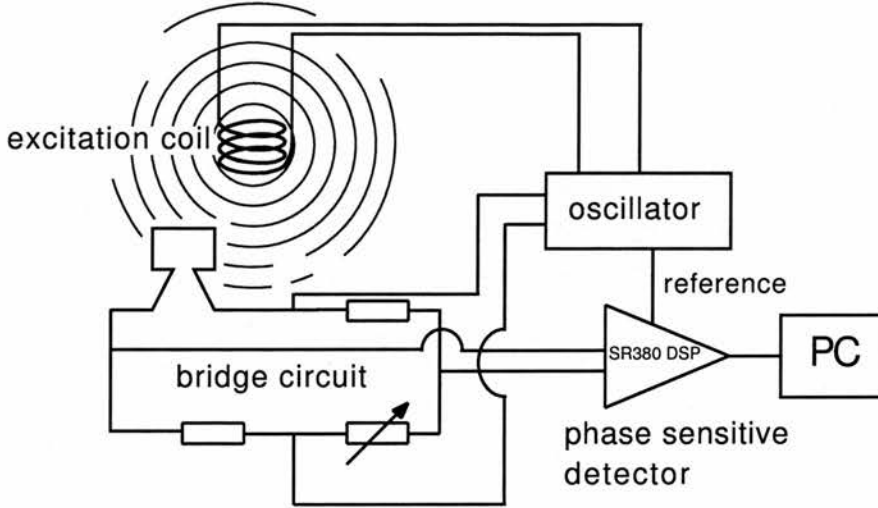


Figure 5.12: Schematic diagram of the measurement apparatus.

5.4.1 Study of the Circuit

The phase on the lock-in amplifier was adjusted to maximise the signal. It should be noted that the drive signal and output signal are not expected to be in phase because of the inductance of the coil.

1. Drive Circuit

The drive circuit can be seen in Fig. 5.13.a, and it can be modelled as in Fig. 5.13.b.



Figure 5.13: (a) An sketch of the drive circuit. (b) The drive circuit modelled by the resistance and the inductance of the coil.

Suppose the current in the circuit is,

$$i = i_0 \cos \omega t \tag{5.29}$$

The total voltage across the circuit is,

$$V_T = iR - \frac{\partial \Phi}{\partial t} \quad (5.30)$$

and writing Φ in terms of the current and inductance, $\Phi = iL$, then,

$$\begin{aligned} V_T &= i_o R - L \frac{\partial}{\partial t} i_o \cos \omega t \\ &= i_o R \cos \omega t + L \omega i_o \sin \omega t. \end{aligned} \quad (5.31)$$

From Eq. 5.31 an important consequence can be deduced.

The reference phase for the phase sensitive detector (PSD) is taken from the voltage, but it is the current through L which determines the phase of the external circuit.

$$V_T = i_o R \cos(\omega t + \phi) + L \omega i_o \cos(\omega t - 90^\circ) \quad (5.32)$$

which can be represented as a complex quantity

$$V_T = i_o (R - j\omega L) \cos \omega t. \quad (5.33)$$

This is the sum of two vectors with an angle defined by,

$$\tan \phi = \frac{\omega L}{R}. \quad (5.34)$$

Thus, there is a phase shift ϕ between the reference voltage phase and the drive current for the coil, and hence the drive field. And the amplitude is,

$$|V| = |i|\sqrt{R^2 + L^2\omega^2} = |i|z. \quad (5.35)$$

2. Detection System

There are two voltages in the detection system. The voltage due to the piezoresistors and the unwanted voltage due to pick-up.

The signal from the out-of-balance bridge due to a change in the piezoresistance, is dependent on time, since the force applied on the cantilever is time dependent. Therefore, the output voltage, which is proportional to the change of the piezoresistor is also time dependent. From Section 5.2 and Section 5.3 it can be concluded that,

$$V_{piez} \propto \Delta R_{piez}(t) \propto F(t) \propto \Delta B(t) \propto i_0 \cos \omega t \quad (5.36)$$

i.e. V_{piez} is in-phase with the current.

On the other hand, the voltage due to the pick-up, which is created by the change of induction $\Delta B(t)$ (which gives a time dependent flux $\Phi(t) \propto \Delta B$) in the circuit, is out of phase with the current.

$$\begin{aligned} V_{p-u} &= -\frac{\partial \Phi}{\partial t} \\ &= -K \frac{\partial}{\partial t} \cos \omega t = K\omega \sin \omega t \end{aligned} \quad (5.37)$$

Therefore, the total detection voltage off resonance is,

$$\begin{aligned}
 V_T &= V_{piezo} + V_{p-u} \\
 &\propto V_{0piez} \cos \omega t + V_{0p-u} \omega \cos(\omega t - 90^\circ)
 \end{aligned}
 \tag{5.38}$$

which is the sum of two signals with a phase difference of 90° . Therefore, the terms are completely separable. The amplitude of the voltage from the pick-up is linear with the frequency and the amplitude of the voltage from the piezoresistors constant. The behaviour can be seen schematically in Fig. 5.14.a and Fig. 5.14.b respectively.

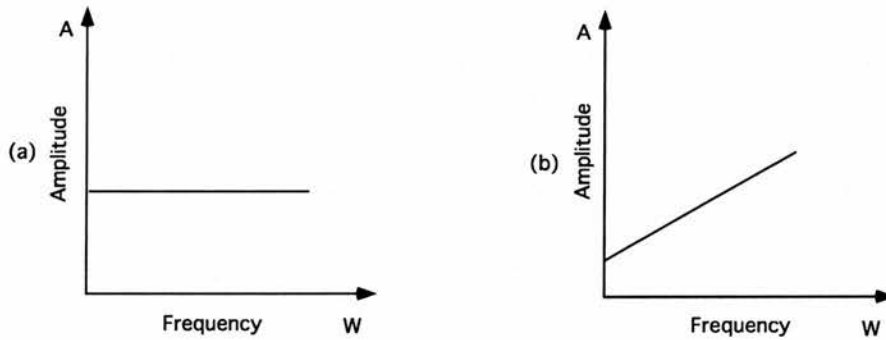


Figure 5.14: (a) The piezoresistors absolute amplitude behaviour as function of the driving frequency off resonance. (b) Behaviour of the pick-up absolute amplitude as function of driving frequency.

Near the resonance, as explained in Section 2.4, the piezoresistors voltage suffers a phase change, since the resonance occurs at 90° out of phase from the driving frequency. The pick-up voltage, on the other hand, has the same linear behaviour with frequency, as can be seen in Fig. 5.15.a and Fig. 5.15.b respectively.

5.5 Initial Results

First attempts to mount the magnetic particle on the smallest cantilever paddles were unsuccessful, since the magnetic particle was of the same diameter as the paddle and therefore

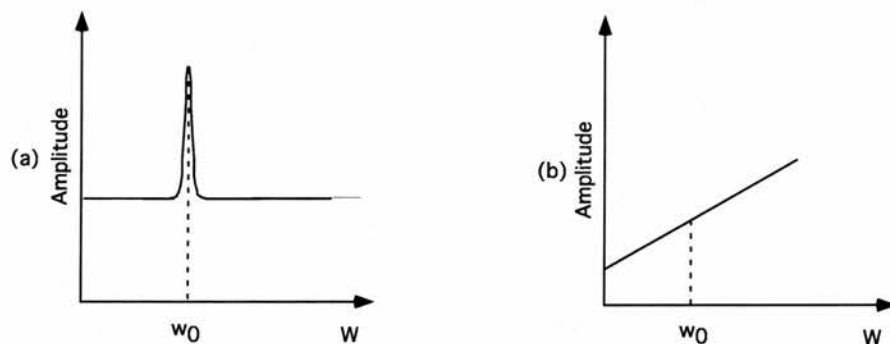


Figure 5.15: (a) Piezoresistors absolute amplitude change near resonance. (b) The pick-up absolute amplitude behaviour near resonance as function of driving frequency.

too big for it, typically of $100 \mu\text{m}$ diameter cylinder and $400 \mu\text{m}$ length. Hence, only the bigger cantilever paddles were used to performed the following measurements.

Once a magnetic particle is mounted onto the paddle, with the aid of a micromanipulator and a very small amount of glue. The coil is then placed in the optimal position to achieve the highest force (Section 5.2) . The bridge is balanced and then the ac current is applied to the coil and the bridge. Using LabView, the data is read into a computer, where the real and imaginary part of the signal are recorded.

Before taking any measurement, it is important to optimise the signal by varying the phase of the lock-in amplifier. Taking the same measurement, lock-in the phase at different angles, it is found that the optimal angle to do the measurements was 20° , as can be seen in Fig. 5.16, where optimal is considered when in phase with the current.

As it can also be seen in Fig. 5.16, the resonant frequency of the cantilever and the particle is a few hundred hertz. This large change is due to the relatively large mass of the magnetic particle. The current hand-mounted particle is typically of $100 \mu\text{m}$ diameter cylinder and $400 \mu\text{m}$ length, which is of about $8\mu\text{g}$. This carries some advantages:

1. The moment is large and hence resonance is easy to excite.
2. The large load leads to a low resonance frequency of a few hundred Hertz, which is

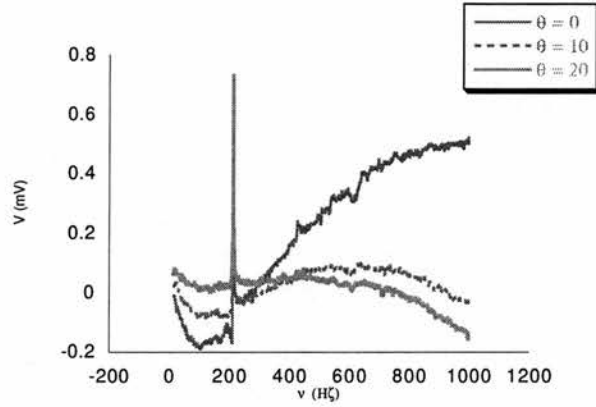


Figure 5.16: Optimisation of the signal varying the phase of the lock-in amplifier.

easy to measure.

3. The large load also leads to high-Q giving good resolution and performance even resonating in air, since the mass of the system increases but the frictional damping (proportional to the cross-sectional area) does not. Q can be expressed in terms of the effective mass as,

$$\begin{aligned}
 Q &= \frac{m^* \omega_0}{b} \\
 &= \frac{\sqrt{m^* k}}{b}
 \end{aligned}
 \tag{5.39}$$

which easily explains the Q enhancement when incrementing the effective mass, m^* .

The component that is approximately out of phase with $i(t)$ arises from direct pick-up of the driving magnetic field, so can be easily separated from the resonance signal. This pick-up can nevertheless be greatly reduced by using a matched pair of piezoresistors on the device. After optimising the response of the cantilever to the magnetic field is stable and has a sharp peak at the resonance frequency, as can be seen in Fig. 5.17. This resonant frequency is close to the one predicted by the FE analysis which was 430Hz.

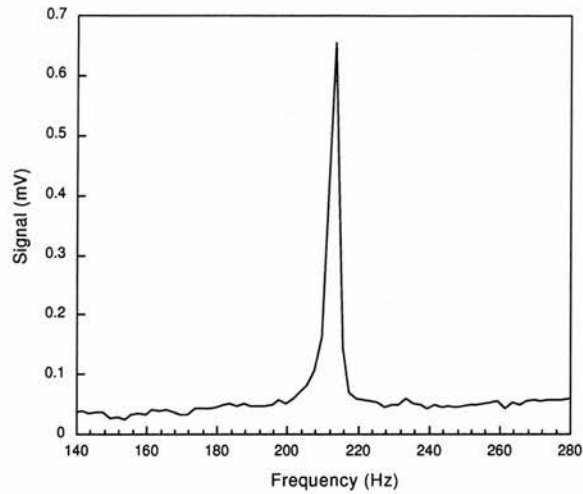


Figure 5.17: Typical response of a cantilever to the changing frequency of the oscillating magnetic field.

This resonant frequency will be altered if the total mass of the resonating element changes. As the load on the paddle is increased, the resonant frequency decreases, since the resonance frequency is given by,

$$\omega_0 \propto \sqrt{k/m_0} \quad (5.40)$$

where k is the spring constant and m_0 is the effective mass of the cantilever paddle.

The high sensitivity of these microcantilevers makes it possible to measure small changes in mass. A mass calibration was performed by adding small cubes of salt, with the aid of a microscope and some micromanipulators. An estimate of the weight of the salt cubes is made by determining the size of the cubes and multiplying the volume by the density of salt. From this, an average of 1100 ng per cube is estimated. As can be seen in Fig. 5.18 the paddle completely loaded. Note that the paddle has been evaporated with gold for the SEM, which accounts for irregular deposits on the surface.

Fig. 5.19 shows that the resonant frequency shift is linear with mass. The linear nature of response may be surprising due to the square root dependence of the cantilever mass

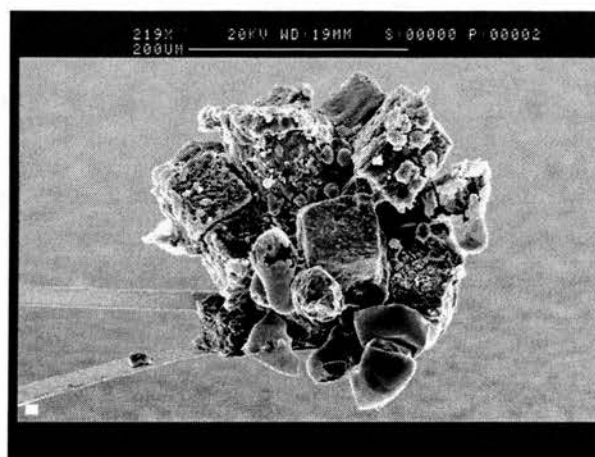


Figure 5.18: A paddle loaded with an Fe cylinder and surrounded by cubes of salt.

Mass (μg)	FEA Δf (Hz)	Experimental Δf (Hz)
0	430.907	367.86
1	426.665	356.86
2	422.291	351.00
5	410.318	342.00
10	392.202	320.00

Table 5.1: Change in frequency per μg for the FE analysis and experimental data.

Eq. 5.40. However, the estimated total added mass is negligible relative to the mass of the cantilever and the magnetic particle. Eq. 5.40 is essentially linear over this limited range and the resonance should follow Eq. 5.41, as explained in Section 2.4.1.2. From the data in the graph it can be deduced that a sensitivity of 240 ng per Hz is detected. Using the simple arrangement described here, frequency changes down to 0.01 Hz could be resolved, which means that a change as small as 3 ng can easily be achieved. These results are in good concordance with the FEA results described in Chapter 3, as can be seen in Table. 5.1.

$$\frac{\Delta\omega}{\omega_0} = -\frac{1}{2} \frac{\delta m}{m} \quad (5.41)$$

Preliminary measurements have also been performed to dynamically monitor simple inorganic chemical reactions, in order to develop software and instrumentation for the desired

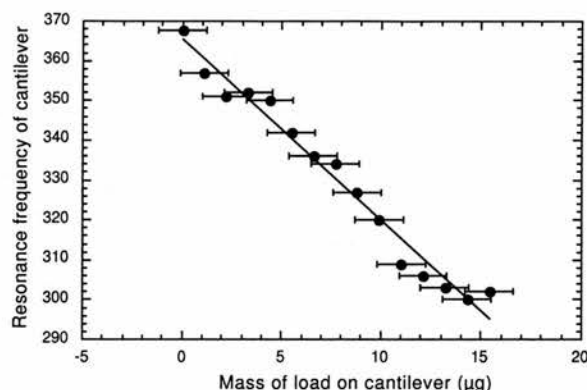


Figure 5.19: The resonance frequency of the cantilever as a function of the load of salt crystals.

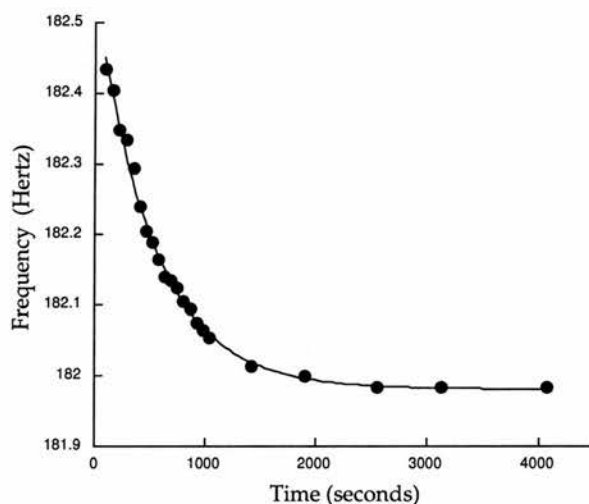


Figure 5.20: Dynamic monitoring of the hydration of a tiny copper sulphate crystal adhered to a cantilever.

application. At present experiments which involve submerging the cantilever in a liquid are difficult because the surface tension tends to dislodge the manually attached magnetic particle.

Fig. 5.20 is an example of an alternative experiment where the reactant is attached to the paddle and exposed to a reactive gaseous atmosphere. In this measurement a tiny dehydrated copper sulphate crystal (ca. $50\mu\text{m}$ diameter sphere) is placed on the cantilever, where the magnetic particle had previously been attached, and exposed to an atmosphere of humid air, causing the crystal to rehydrate (ca. 10% mass change for this crystal). As

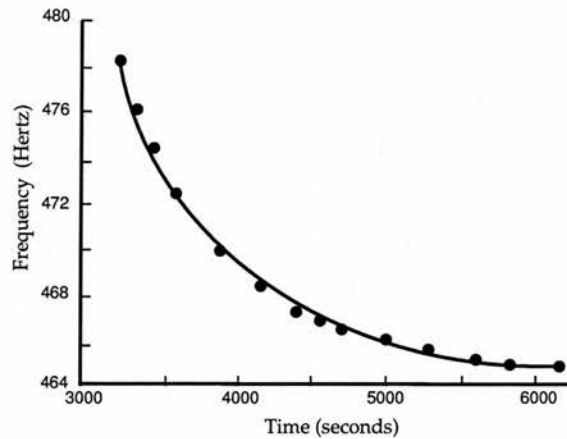


Figure 5.21: Dynamic monitoring of the hydration of calf's thymus DNA attached to a cantilever.

the mass of the crystal increases the resonance frequency falls until it reaches a plateau due to the saturation of the copper sulphate crystal. It should be noted that this represents the dynamic monitoring of a reaction of a tiny single crystal.

Fig. 5.21 is another example of a dynamic measurement. It shows the dynamic monitoring of a small sample of calf's thymus DNA in response to step wise changes in humidity. As in the case of the sulphate crystal, a piece of dry (lyophilised) DNA is adhered to the paddle and exposed to an atmosphere of humid air, causing the DNA to absorb the water. In this case the DNA absorption also reaches a plateau although in this case it takes longer to reach the complete saturation state. It can also be note that due to the experimental conditions, real measurements could not be taken until the system was in equilibrium.

5.6 Conclusions

A direct excitation mechanism was chosen since it minimises mixed modes. Furthermore, a magnetic excitation was selected for its compatibility with liquids. The force mode was considered the most suitable mechanism since it requires smaller coils. Smaller coils for a given power means smaller magnetic field producing a small torque, but even for small

magnetic fields the gradient of the field can be large, generating a big force. It is important to maintain the sensor as small as possible, for it to be compatible with the μ TAS technology.

A Wheatstone bridge driven by an AC voltage with a lock-in amplifier was used to read out the signal. The problems arising from the imbalance in the capacitive and/or inductive values of the bridge network were discussed and an experimental solution given, by manually tracking the right phase at which to monitor the resonance signal.

Theoretically, the Johnson noise in the piezoresistors is the dominant source of noise in the actual devices. Nevertheless, it could be improved by either reducing the resistance to the minimum possible value, or redesigning the cantilevers (e.g. making them thinner) so that the minimum detectable displacement is improved.

First measurements were taken on the cantilevers confirming the predictions made by the FE analysis. A sensitivity of 3 ng over 30 ms averaging time was achieved even though the relatively large magnetic particle attached onto the paddle decreases the expected relative change $\Delta m/m$ expected.

Dynamic monitoring measurements of different samples were performed. Our proposed application in the first instance is to develop a system to measure the occurrence of a reaction by an initial and final measurement. This example, however, demonstrates the potential of the method to dynamic monitoring.

References

- [1] D. Sarid, *Scanning Force Microscopy*, Oxford University Press, (1991).
- [2] Y. Hirai, *et al.*, Jpn. J. Appl. Phys., **37**, 7064, (1998).
- [3] S.P. Jarvis *et al.*, 'A New Force Controlled Atomic Force Microscope for Use in Ultrahigh Vacuum', Rev. Sci. Instrum. **67** (6), 2281-2285, (1996).
- [4] W. Han and S.M. Lindsay and T. Jing, 'A Magnetically Driven Oscillating Probe Microscope For Operation in Liquids', Appl. Phys. Lett. **69**(26), 4111-4113, (1996).
- [5] E.L. Florin *et al.*, 'Atomic Force Microscope With Magnetic Force Modulation', Rev. Sci. Instrum. **65** (3), 639-643, (1994).
- [6] S.J. O'Shea, *et al.*, Chem. Phys. Lett., **223**, 336, (1994).
- [7] M.A. Lantz and S.J. O'Shea and M.E. Welland, 'Force Microscopy Imaging in Liquids Using ac Techniques', Appl. Phys. Lett. **65**, (4), 409-411, (1994).
- [8] M. Alonso, and E. J. Finn, *Fundamental University Physics II. Fields and Waves*, Addison-Wesley, (1967).
- [9] M. P. Fabry, 'Eclairage Electrique', **17**, 133, (1898).
- [10] D. B. Montgomery, *Solenoid Magnet Design*, Wiley & Sons, (1969).

- [11] H. Nyquist, 'Thermal Agitation of Electric Charge in Conductors', *Phys. Rev.*, **32**, 110-113, (1928).
- [12] M. Tortonese *et al.*, 'Atomic Force Microscopy Using a Piezoresistive Cantilever', *Proceedings of Transducer's 91*, IEEE, New York, 448-451, (1991).
- [13] F. N. Hooge, '1/f Noise Is No Surface Effect', *Phys. Lett. A*, **29**, 139-140, (1969).
- [14] L. K. J. Vandamme and S. Oosterhoff, 'Annealing of Ion Implanted Resistors Reduces the 1/f noise', *J. Appl. Phys.*, **59** (9), 3169-3174, (1986).
- [15] G.E. Uhlenbeck and L.S. Ornstein, 'On the Theory of the Brownian Motion', *Phys. Rev.*, **36**, 823-841, (1930).
- [16] J.W. Young, 'Optimization of Acoustic Receiver Noise Performance', *J. Acoust. Soc. Amer.*, **61**, 1471-1476, (1977).
- [17] T.B. Gabrielson, 'Mechanical-thermal Noise in Micromachined Acoustic and Vibration Sensors', *IEEE trans. Electron. Devices*, **40** (5), 903-909, (1993).
- [18] C. Kittle, *Elementary Statistical Physics*, New York, Wiley, (1958).
- [19] D.P. Smith, 'Limits of Force Microscopy', *Rev. Sci. Instrum.*, **66** (5), 3191-3195, (1995).

Chapter 6

Microfabrication and Design of Magnetic Particles

6.1 Introduction

In our preliminary studies the most versatile and robust method of excitation of the cantilever resonance for this application uses a small permanent magnet attached to the cantilever which is driven by a small *ac* magnetic field. A small coil placed close to the device produces an alternating force on the cantilever due to the switching of the gradient of the magnetic field associated with the coil. For optimum performance the magnetic particle should be of high coercivity, that is, the direction of its magnetic moment is not reversed easily when the driving field changes direction. The particle should also have a high aspect ratio with the long axis perpendicular to the surface of the paddle. This is to ensure the self-return field from the particle (the demagnetising field) causes the minimum energy configuration adopted by the system to be that in which the magnetic moments align along the long axis. The only force on the cantilever will then be directed towards the coil, thus stabilising a large-amplitude single-mode oscillation. In our preliminary studies magnetic particles of

transition metal elements were attached to the cantilever *after* microfabrication. These were found to perform excellently in combination with the piezoresistive strain sensors. It is obviously desirable to include the magnetic particles as part of the microfabrication process.

There are several possible approaches to achieving this including lithographic lift-off techniques or ion-beam milling of deposited films, or electrodeposition of a metallic element. These techniques and the application to the specific case studied here are discussed in the following section. The advantages and disadvantages of each technique are discussed and finally one technique is chosen to implement within the main process. At the end of this chapter it is explained how the chosen technique is applied and the results achieved using this technique are shown.

6.2 Fabrication Techniques

Different magnetic materials are used for the different techniques approached. From the point of view of the magnetic properties of the materials iron is the most suitable element, and indeed was used in the post microfabrication procedure. For ion-beam milling and lift-off techniques cobalt was used, since it is the only magnetic material evaporated at Southampton University. And finally since nickel is the easiest material to electroplate and is a magnetic material, it was decided to electroplate nickel.

6.2.1 Ion Beam Milling

Ion Beam milling to obtain high aspect ratio structures was first used in 1996 [1]. This is a very straight forward approach that uses deep anisotropic etching. A diagram of the process can be seen in Fig. 6.1.

To achieve this high aspect ratio for magnetic particles a very thick layer of cobalt is

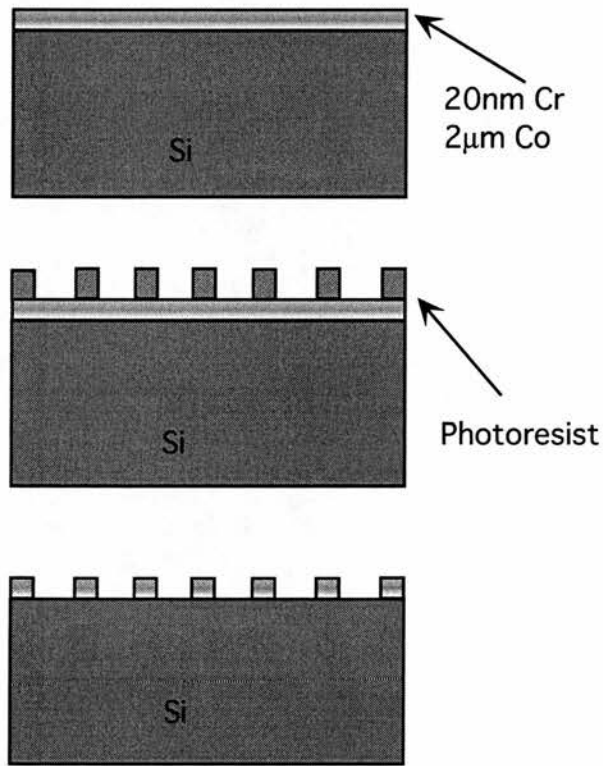


Figure 6.1: Schematic representation of an Ion beam milling process.

needed. The minimum feature given by contact lithography is $1\ \mu\text{m}$, therefore a layer of at least $2\ \mu\text{m}$ is needed. To evaporate cobalt, the source is heated up to $500\ ^\circ\text{C}$ with a high energy electron beam. Once evaporated it quickly cools down. This large change in temperature subjects the cobalt layer to an enormous stress.

In the facilities at Southampton, evaporation of such a thick layer of cobalt had never previously been attempted. Therefore, a first attempt was made, and no problems were found in evaporating $2\ \mu\text{m}$ of Co. A thickness of $1\ \mu\text{m}$ was evaporated, left overnight, and then another $1\ \mu\text{m}$ was evaporated, ($1\ \mu\text{m}$ of Co had previously been evaporated without problems). No metal layer was evaporated between the Co and Si. When the wafers were spin coated with the resist, the cobalt peeled off. It was thought that the reason the cobalt peeled off was due to the lack of a thin metal adhesion layer in between the silicon and the cobalt.

The next step was to verify whether or not the cobalt would adhere properly with a metal interfacial layer. In order to decide which of the typically used adhesion layers was best, chromium and titanium were used. $40\ \text{nm}$ of titanium was evaporated on two wafers and $40\ \text{nm}$ of chromium on another two. It was decided that the $2\ \mu\text{m}$ of Co could be evaporated in a single step, since no problems had been encountered in the previous run. A first attempt was made with the Ti layer, and it resulted in very good adhesion between the cobalt and titanium, so that there was no peeling when subsequently spinning the wafer with resist. Nevertheless, a different problem arose due to the contamination from the walls of the chamber. The very high stress in the cobalt caused the different layers of metal on the wall of the evaporator to peel off.

During evaporation, not only are the wafers coated, but also the walls of the chamber. Therefore, when evaporating $40\ \text{nm}$ of Ti on to the bare wafers, Ti is also being deposited on the walls. The evaporated cobalt therefore, not only sticks to the wafer but also to the walls. The large stress created in the cobalt with the change in temperature causes the

cobalt to curl up once it has stuck to the titanium layer on the wall. Subsequent evaporation of different materials creates many different layers on the walls. Therefore, the curling up of the cobalt not only causes the titanium layer to peel off, but all the different layers on the walls that were previously evaporated. This is a problem since it causes contamination within the evaporator.

Due to this problem, only the two wafers with a Ti adhesion layer were used, and the use of Cr as an intermediate layer was abandoned. The wafers with $2\mu\text{m}$ of Co and 40 nm of Ti were ion-beam milled. The first attempt was performed with $2.2\mu\text{m}$ of resist and 60 minutes of ion-beam milling. We can see in Fig. 6.2 that the milling is smooth and that although $1\mu\text{m}$ of photoresist has still not been etched in the large features, 367 nm of Si has been etched due to the effect of ion-beam milling on the sides. It can also be observed that the profile is closer to 45° than to 90° .

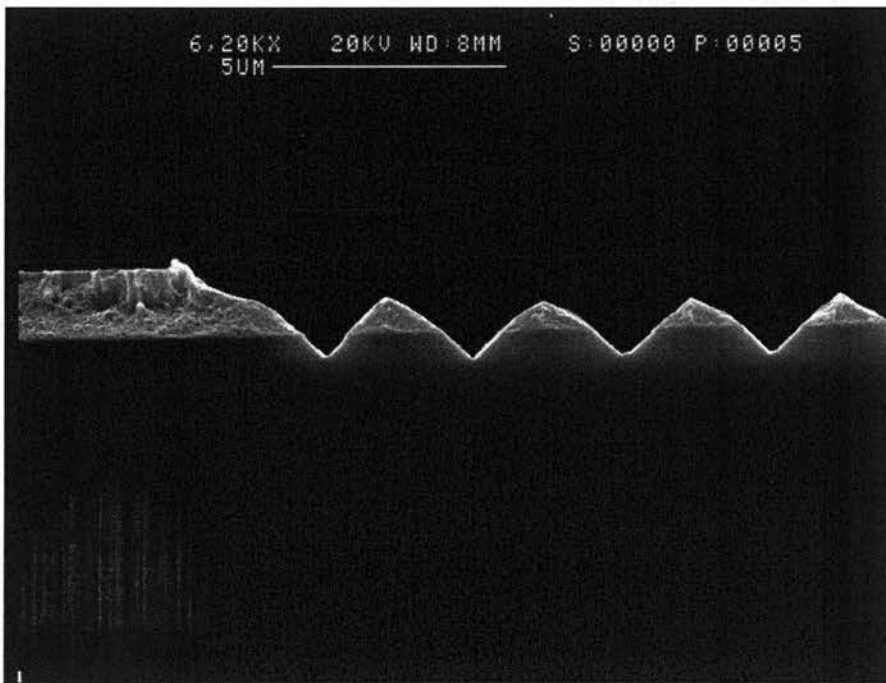


Figure 6.2: SEM image of dark and light field features after 60 min of ion-beam milling.

It had been assumed that the ion-beam milling rates for cobalt and the resist were the

same, but with the resist used (SPRT518) in practice it turned out that the milling rate of the resist was about double that of the cobalt. Therefore, for the second wafer 1.1 μm of photoresist was used and, with the aim of minimising the effects at the sides, it was ion-beam milled for only 50 minutes. In this case, as can be seen in Fig. 6.3 the sidewalls are again about 45°. There was 250nm of Si etched and 1.6 μm of Co was left.

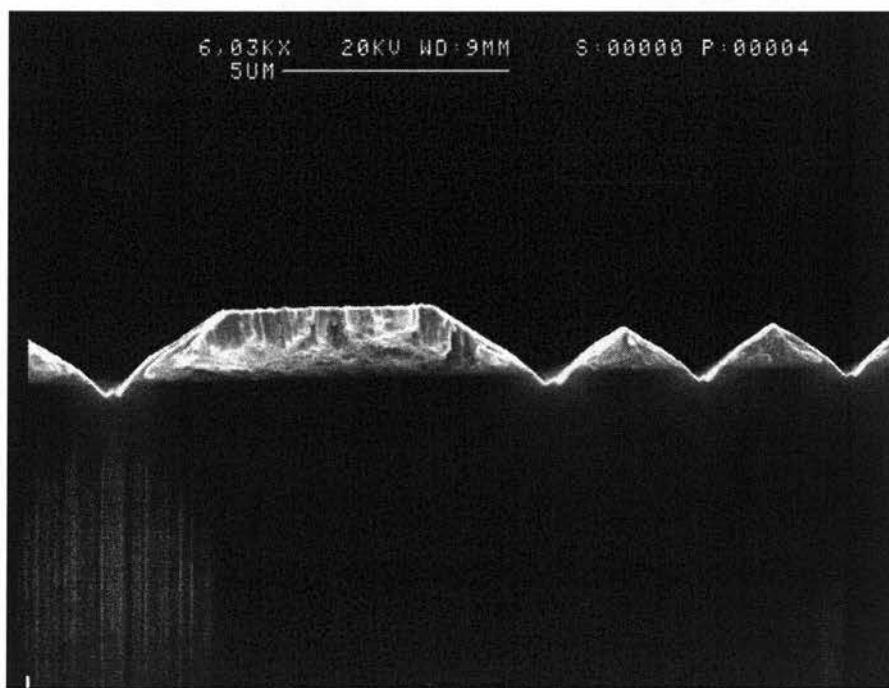


Figure 6.3: SEM picture of dark and light field features after 50 min of ion-beam milling and only 1.1 μm of photoresist.

An attempt was made to repeat this process with another batch, but it was found that the wafers bowed due to the stress in the cobalt. As described in subsection 4.2.2 when the wafers are bowed, the light used to expose the resist is reflected and diffraction patterns are created on the wafers due to the very small pattern features, making it impossible to perform the lithography. The detailed fabrication process list can be found in Appendix B.

A final trial was carried out. Aiming to reduce the stress created by the cobalt, silicon dioxide (SiO_2) was grown on two wafers -the stress created by the cobalt would be released through the silicon dioxide. With the same purpose, it was decided to use a shadow mask on

two wafers (one with SiO_2 and one without), so that less cobalt would actually be evaporated onto the wafer and therefore the stress would be reduced. The process list can be seen in Appendix B. The wafers appeared not to be bowed, and were ready to be ion beam milled. But at that stage, the ion beam miller developed a long term problem which did not get resolved before completion of the study of the various fabrication methods.

6.2.2 Lift-Off

A simple, tried and tested method to pattern metallic films is simply to allow metal to adhere to the substrate only in regions where it is ultimately desired. In this process, a layer of an intermediate film (such as photoresist) is first deposited and patterned on the substrate. The structural film is next evaporated on the sample. This film is patterned by selectively removing the intermediate layer (and the structural material above it) as shown in Fig. 6.4. Lift-off techniques are commonly used for patterning low-melting point metal interconnects.

A first attempt was carried out to fabricate magnetic particles using this method, which is easy to process. The process listing can be found in Appendix B. Aiming to reduce the stress created by the cobalt, silicon dioxide (SiO_2) was grown on two wafers (a sketch can be seen in Fig. 6.4).

The main problem when attempting this method is the stress created by the cobalt. When taking the wafers from the evaporator the cobalt was already peeling off from a large area of the wafer, nevertheless one of the wafers was taken a step further and was introduced into NMP (N-Methyl Pyrrolidone) for the last step of the lift-off process, to remove the unwanted metal. At this point, most of the metal was inadvertently removed. The areas that needed to be removed were much larger than those we wanted to keep. This added to the high stress on the cobalt layer made it impossible to retain the $1\mu\text{m}$ by $2\mu\text{m}$ magnetic particles. On the two wafers on which the SiO_2 was grown, the amount of cobalt peeling off

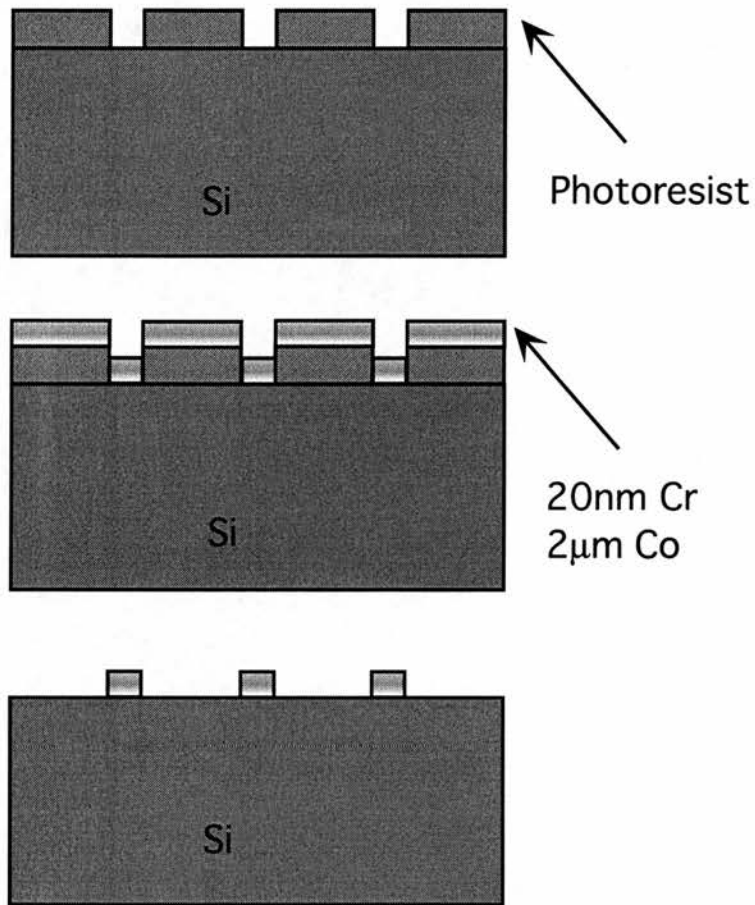


Figure 6.4: Schematic representation of a lift-off process.

was less, but nonetheless, the result was the same.

In thinner layers of cobalt the stress created is much lower, but due to the limitations of the contact lithography, and the requirement to have high aspect ratio pillars, a layer at least $2\ \mu\text{m}$ thick was needed.

6.2.3 Electroplating

Electroplating is a very useful process for producing additive metal structures above a substrate and can be done in a beaker with simple and inexpensive equipment. The object to be plated is metallised and masked to define regions on which metal is to be deposited and it is maintained at a negative potential (*cathode*) relative to an inert positive counterelectrode (*anode*). The electroplating solution (generally aqueous) contains a *reducible* form of the ions of the desired metal. By biasing the surfaces to be plated at a negative potential, electrons are supplied to the surface of the exposed metallic conductors and metal ions in the solution are reduced at the surface (one or more electrons are added to each ion so that it becomes a metal atom), depositing metal there. The metal ions must also bond to the surface for plating to be effective (an intermediate layer may be required for some combinations of plated metal and substrate).

The electrochemical mechanisms underlying electrodeposition exhibit a saturable $\mathbf{J} - \mathbf{V}$ characteristic (current density, \mathbf{J} , is used rather than the total current, \mathbf{I}). Above a certain applied potential, the total current depositing metal saturates at \mathbf{J}_{lim} . A further increase in voltage occurs above this point due to the increase of the current, but the excess current ends up driving unwanted reactions. Thus, for a given electroplating chemistry there is generally a recommended current density that for a specific temperature, provides an optimal deposition rate. Often, these recommended current densities do not simply correspond to the maximum rate, but also take into account the morphology of the plated metal.

The quality of the plating is mainly assessed by the roughness, uniformity, and purity. These properties depend on a number of different parameters that need to be controlled. The most important parameters to control are:

- Plating temperature
- Current density
- Electroplating solution composition, additives, concentration and quality maintenance
- Cell/equipment design (anode geometry, anode position, tank shape etc.)
- Mixing/stirring conditions
- Quality of the seed layer, adhesion layer, photoresist material
- Pre-plating steps, cleaning, rinsing etc.

The plating temperature, current density and electroplating solution composition and concentration still, have to be controlled precisely and are defined by the electrolyte supplier. The stirring conditions and the tank shape can also be defined by the supplier, but the seed layer, plating geometry and pre-plating steps are left to the designer to formulate in the optimum way. Low aspect ratio geometries are easier to electroplate as it is easier to achieve a uniform surface, since it is easier to have a uniform current density across the wafer.

With high aspect ratio geometries, such as the ones required here, it is more difficult to get uniform current density. The uniformity depends on the electric field distribution, and this in turn depends on a number of factors including the resist pattern. The resist pattern may affect the field distribution in many ways. The sidewall quality (vertical, slanted, rough, clean, contaminated etc.) and the actual pattern design (sharp points, edges etc.) are the most important factors to account for.

Even with vertical current lines, there might still be a problem with the current density distribution since the pattern design may generate 'edge effects', thus causing excess current density in some sites on the wafer. This may be overcome by corrections in the design or by introducing so called *dummy* sites, that is, pattern sections that are not a functional part of the design.

6.3 Moulds for Electroplating

An increasing number of applications in MEMS require high aspect ratio lithography, *i.e.* good dimensional control over the vertical sidewalls of tall structures. The most well known technique is the LIGA (Lithographie, Galvano-formung, Abformung) process [2], which makes use of synchrotron X-ray lithography to pattern very thick PMMA (polymethylmetacrylate) layers. As frequently reported in the literature [3, 4], X-ray lithography is an ideal technique for achieving high aspect ratio structures with submicron resolution because of the reduced diffraction, low resist absorption and absence of scattering. However, the cost of the LIGA process is prohibitively high due to the need of a synchrotron radiation source, which currently makes it inappropriate for general routine application. This gives rise to the necessity of finding an UV photolithography based process, which would be suitable for many MEMS applications, even though the aspect ratio ultimately attainable might be lower than with LIGA.

Different photoresists were investigated with the aim of achieving the high aspect ratio geometries needed. In particular polyamide, a thick epoxy based photopolymer (SU-8) [5], and a commercially available positive photoresist (SPR220-7) were tried. In the following section a description is given of the work undertaken on the different photoresists, SU-8 and SPR220-7, a negative epoxy based photoresist and positive photoresist respectively. Processes for thicknesses varying from $20\mu\text{m}$ up to $100\mu\text{m}$ were developed for the fabrication

of high aspect ratio microstructures for application in micro-actuation of a micromechanical cantilever.

6.3.1 SU-8 Negative Photoresist

IBM first developed SU-8 photoresist based on the EPON resin commercially available from Shell Chemical. There are three attributes which make this photoresist well suited for thick film applications [6, 7]

- Due to its low molecular weight, SU-8 dissolves in a variety of organic solvents, such as PGMEA (propylene glycol methyl ether acetate).
- SU-8 has very low optical absorption in the near UV-range. This high transparency can be exploited to fabricate high aspect ratio patterns, featuring almost vertical sidewalls. Aspect ratios of up to 18 have been reported [7].
- Because of its highly cross-linked matrix, the exposed resist shows thermal and chemical stability, making it suitable for prolonged plasma etching and electroplating processes.

SU-8 can be spun to thicknesses from 1-1000 μm using a single coat, thereby reducing problems. It has excellent mechanical properties and is able to provide structure and support for microstructures.

There are six standard grades of SU-8 commercially available. The resultant mixture is characterised by its viscosity, which determines the thickness versus spin speed behaviour, as can be seen in Table 6.1.

As a chemically enhanced negative photoresist, SU-8 must be spun, pre-exposed baked, exposed, post-exposure baked, developed and finally removed. These various process parameters determine the characteristics of the final layer.

SU-8	%Solids	Viscosity (cSt)	Thickness (μm) at 900 rpm
5	51.8	265	12
10	59.1	989	30
25	63.3	2646	58
50	69.1	14953	150
100	72.9	52407	320

Table 6.1: Relationship of the commercially available standard grades with the viscosity and thicknesses.

1. Resist Spin

The standard SU-8 100 was used. By varying the speed at which it was spun, different thicknesses were obtained. The spin curve shown in Fig. 6.5 represents the thickness versus spin speed characteristics found. As can be seen the speed at which it needs to be spun in order to achieve 100 μm is 3000rpm, which is relatively high. This thus avoids the formation of edge beads (accumulation of the resist at the edge of the substrate), and leads to a good homogeneity of the resist layer. Due to the high viscosity of the resist, it was found that it was best to pour the resist directly from the bottle onto the wafer, measuring by eye the quantity needed to achieve the desired thickness.

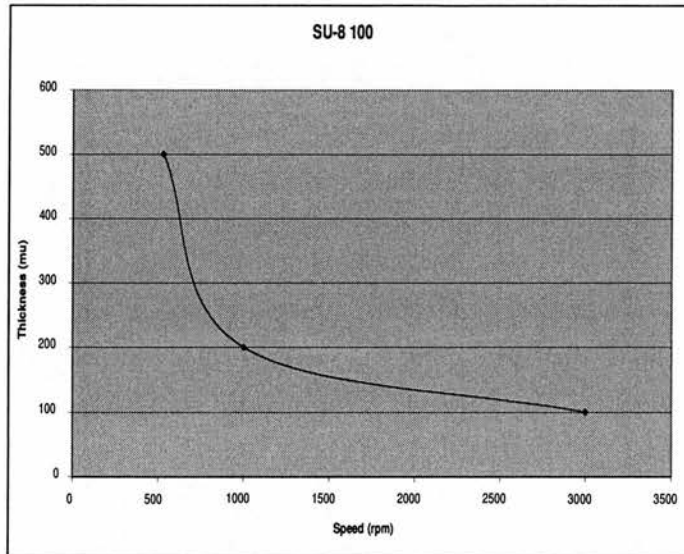


Figure 6.5: SU-8 100 Spin Curve.

2. Pre-Exposure Bake

The pre-exposure bake stage is one of the most important stages of the process. The exposure time, development time, structure definition, and the mould's aspect ratio may vary depending on the chosen bake [8]. The pre-bake was performed at 135°C on a hot plate for an hour. Since the baking was done without a ramped temperature cycle high internal stress was generated, which when the resist was exposed produced cracks. With the aim of preventing these cracks in the resist, a ramped temperature cycle was used, using 20 minutes to ramp up the temperature from 50°C to 135°C , an hour at 135°C , and then another 20 minutes to ramp down to 50°C . With this process the cracks were eventually prevented, but as the polymerisation process also occurs at high temperatures the resist close to the substrate was more polymerised and it was more difficult to develop. Further investigation of the cracks show that they were only superficial and didn't go all the way through to the substrate as can be seen in Fig. 6.6. Therefore it was decided to use the non-ramped cycle.

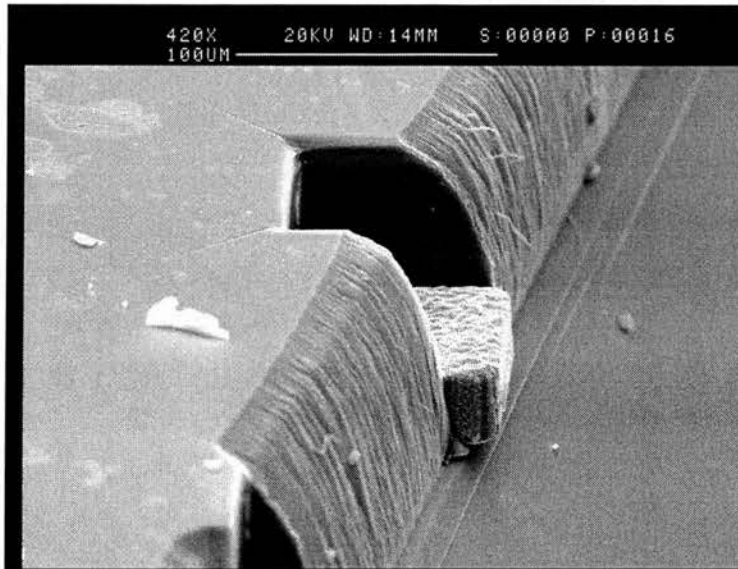


Figure 6.6: SEM picture of the cracks created when the SU-8 is being exposed.

3. Exposure

Exposure to UV light promotes cross-linking of the SU-8 negative photoresist. To ensure uniform illumination through the whole resist layer, a high exposure energy is required. Exposures performed in contact resulted in the resist becoming stuck to the mask due to the heat, so all the exposures were performed in proximity using a small gap. 240 seconds were needed with a lamp of $3.9\text{mW}/\text{cm}^2$.

4. Post-Exposure Bake

Post-Exposure bake is best performed on a hot plate. A 10 minutes post-exposure bake was done on a hot plate at 95°C . After baking, pre and post, the wafer had to cool down before being taken to the following step, in order for the resist to stabilise. Throughout all of the steps it is crucial to always keep the wafer flat in order to produce smooth, uniformly coated substrates.

5. Developing

EC-solvent was chosen for developing the resist. It does not need to be heated up.

It takes 40 minutes with constant agitation for complete development. In Fig. 6.7 a well-developed high aspect ratio square fabricated under the conditions described is shown. As can be seen, vertical profiles were obtain.

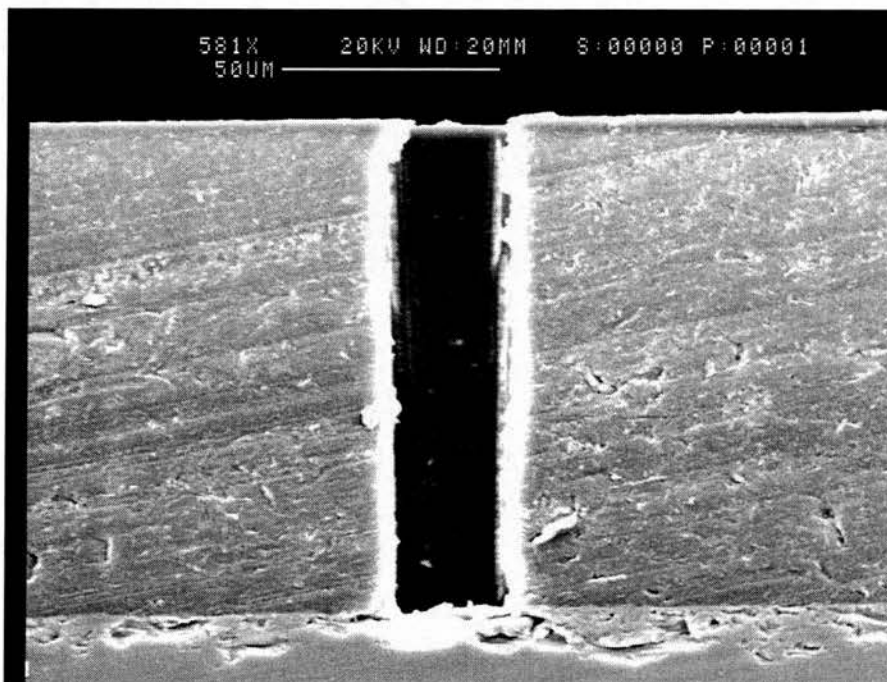


Figure 6.7: SEM image of the cross-section of a well developed SU-8 mould square.

Nevertheless, a 5 minutes de-scum provides smoother side walls as seen in Fig. 6.8.

6. Removal

The removal of the SU-8 is very difficult. Oxygen plasma and fuming nitric acid can be used, though the long times needed for complete removal make both techniques too aggressive for our application. It was reasoned that depending on the geometry of the mould the removal could be more or less plausible. With our geometry it was impossible to remove it, but with 2D geometries the SU-8 can even be removed with NMP at high temperatures.

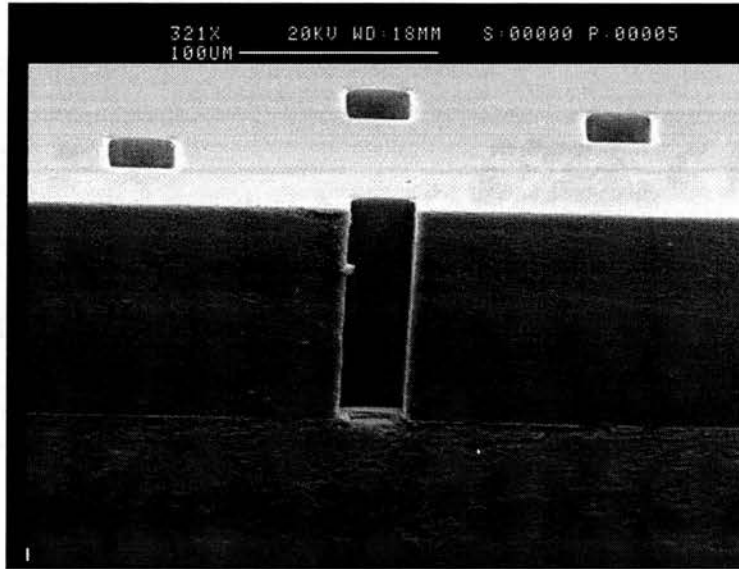


Figure 6.8: SEM image of the cross-section of a de-scum SU-8 mould square.

- Below is a summary of the final Recipe Used with SU-8 100
 - Dehydration bake for 10 minutes in an oven at 190°C
 - Cool down (in order to be able to handle the wafers)
 - Spin with hand spinner at 3000rpm for 60sec
 - Bake on hot plate for one hour at 135°C
 - Cool down to set
 - Exposure with Cannon in proximity for 240 seconds at an intensity of $3.9\text{mW}/\text{cm}^2$
 - Bake on hot plate for 10 minutes at 95°C
 - Cool down to set
 - Develop in ec-solvent for 40 minutes with agitation
 - Rinse with I.P.A.
 - Rinse with water
 - Blow or spin dry

Thickness	Number of layers	Speed
7 μm	1	3000rpm for 60 sec
18 μm	1	750rpm for 60 sec + 2200rpm for 5 sec
36 μm	2	750rpm for 60 sec + 2200rpm for 5 sec, each layer
54 μm	3	750rpm for 60 sec + 2200rpm for 5 sec, each layer

Table 6.2: Relationship of thicknesses with respect to speed and number of layers spun up for the SPR220-7 Positive Photoresist.

6.3.2 SPR220-7 Positive Photoresist

SPR220-7 is a positive photoresist commercialised by Shipley. A number of layers can be spun up one onto another, creating a very thick layer. There is very good adhesion between layers, so there are no gaps preventing the photolithography from being performed. Being a positive photoresist it can be removed with the standard methods, such as acetone and oxygen plasma etching.

As with most positive photoresists, SPR220-7 must be spun, pre-exposed baked, exposed, developed, hard baked and finally removed.

1. Resist Spin

With the positive photoresist SPR220-7, as opposed to SU-8, the spinning speed has to be quite low to achieve thick layers, which brings about a significant edge bead. The situation may be partially improved if a fast short spin is performed after the thickness of the layer has been defined, whereby the edge bead will become narrower. The main characteristic of this positive photoresist is that it is possible to spin layer after layer increasing the thickness of the layer. In Table 6.9 the relationship between the thickness achieved and the speed and the different numbers of layers is shown. There is a limit to the minimum speed at which the photoresist can be spun on, since too low a speed will lead to a very non-uniform resist layer. Therefore there is a necessity to spin layer after layer to achieve thicker layers.

2. Pre-Exposure Bake

The pre-exposure bake is the most difficult step to optimise. Furthermore, the optimisation depends on the number of layers. In the case of one layer, as it is still not too thick, there are not too many problems associated with trapping of the solvent or the temperature gradient across the layer.

For 7 μm , the wafers were baked for 100 seconds on a hot plate at 90°C followed by another 100 seconds on a hot plate at 115°C .

For 18 μm , the wafers were baked for 60 seconds on a hot plate at 90°C followed by 55 minutes in an oven at 90°C .

For 36 μm , 2 layers of 18 μm each are used ; the wafers were baked for 60 seconds on a hot plate at 90°C after the first layer, and then after the second layer was spun on the wafers were baked for 70 minutes in an oven at 90°C .

For 54 μm , therefore 3 layers were used; after the first and second layers were deposited the wafers were baked for 30 seconds on a hot plate at 90°C . After the third layer was deposited the wafer was baked for 60 seconds on a hot plate and then a further 90 minutes bake was performed in an oven at 90°C .

3. Exposure

Before exposing these thick photoresists, the wafers must be left for at least one day after the pre-exposure bake, so that all the solvents evaporate and the resist itself stabilises. Once the resist has settled down the first thing needed to be done is to remove the edge bead formed when spinning on the resist. The edge bead prevents good contact between the wafer and the mask during contact-printing, causing diffraction during exposure. Therefore, in order to achieve high-aspect ratio structures, the edge bead must be removed. With this aim, the edge bead was overexposed for 20 minutes and developed out. Once the edge bead had been removed, the contact between the

Thickness	Exposure Time	Developing Time
7 μm	270s	3 minutes
18 μm	350s	4 minutes
36 μm	600s	6 minutes
54 μm	800s	8 minutes

Table 6.3: Detailed exposure times and developing times relative to thicknesses.

wafer and the mask was good, and the high aspect ratio structures could be defined. The detailed exposure times relative to the thicknesses can be seen in Table 6.3.

4. Developing

If any post-exposure bake were to be done, the photoresist would burn and development would become impossible. SPR220-7 can be developed in a standard positive photoresist developer, for example MF3-22. Times for developing can be found in Table 6.3. An example of the type of mould achieved with this photoresist can be seen in Fig. 6.9. This is a 36 μm thick mould, *i.e.* 2 layers, and it can be observed that the side walls are not as well defined as in the case of SU-8, but they are still good enough for electroplating vertical high aspect ratio columns.

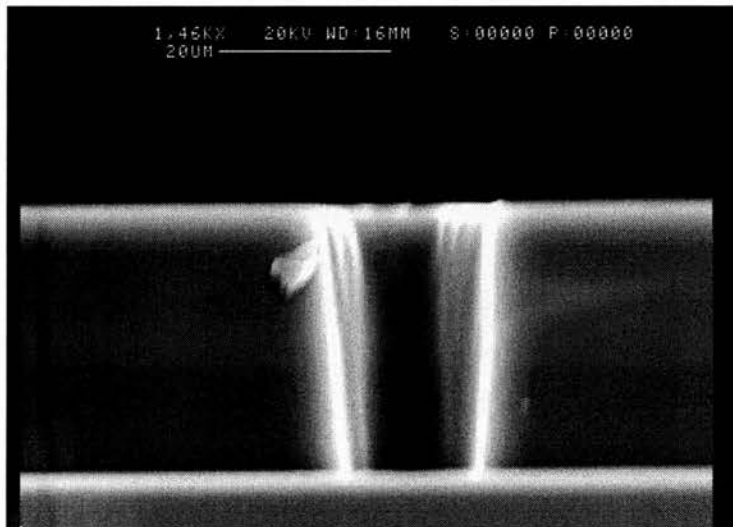


Figure 6.9: SEM image of the cross-section of a SPR220-7 mould structure.

5. Removal

The removal of the SPR220-7 is very easy, which is a clear advantage compared with the SU-8. The less aggressive method required to remove the photoresist after electroplating involves soaking in acetone followed by oxygen plasma etching of the residual photoresist.

6.3.2.1 Electroplating of the Moulds

The electroplating of Ni was carried out in a commercially available sulphamate type bath at 55°C. The experimental set up for the electrochemical deposition of nickel can be seen in Fig. 6.10. It consists of an inner tank filled with the plating electrolyte (nickel sulphamate, nickel chloride, boric acid and sodium lauryl sulphate) placed within an outer tank containing heated water. Inside the inner tank there is a stirrer for the strong mixing required as well as a thermometer to keep the bath temperature under control. The two electrodes (*anode*-nickel thick foil, *cathode*-the wafer to be electroplated) are connected to a stabilised power supply.

There are different electrolyte compositions for nickel electroplating, and therefore different parameters for each of these electrolytes, as can be seen in [9, 10]. Nickel sulphamate electrolyte is based on sulphamic acid, which has been commercially available since the late 1930s. It is beneficial to have 3 to 5 g/l of Cl in the sulphamate electrolyte to promote anode corrosion and to stabilise the pH when not using sulphur depolarised electrolytic nickel anodes [11, 12].

Nickel sulphamate is more soluble than nickel sulphate, this makes the sulphamate electrolyte more suitable for electroplating at high rates with low internal stress deposits, assuming the electrolyte is concentrated enough (*e.g.* 600g/l) and there is a continuous optimal conditioning of the sulphamate electrolyte [13]. On the other hand sulphamic acid is not

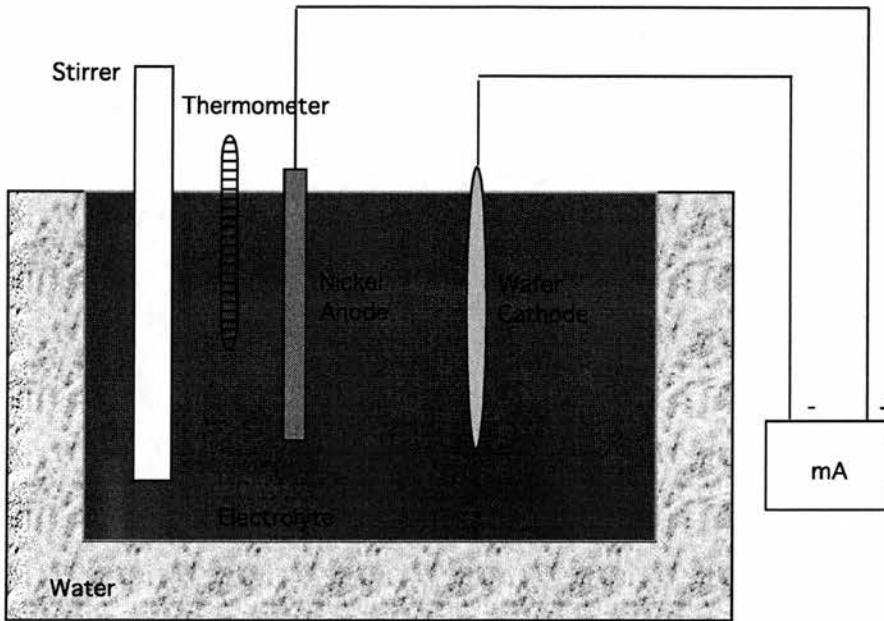


Figure 6.10: Experimental set up of the electrochemical deposition of nickel.

as stable as sulphuric acid, therefore sulphamate baths require more careful control of the conditions; low pH values (below 3.0) and high temperatures (above 60°C) may cause hydrolysis to ammonium sulphate [14]. Highly polarised anodes or the use of insoluble anodes in sulphamate baths cause the formation of azo-disulphonate [13, 15], which introduces sulphide into the nickel plate and can change a dark columnar low tensile stress structured deposit into a bright laminar deposit with high compressive stress [13, 16, 17].

As stated before, the main components of the bath are nickel sulphamate, nickel chloride, boric acid and sodium lauryl sulphate (wetting agent). The nickel ion content is mostly provided by the nickel sulphamate, which is highly soluble and commercially available. The nickel ion concentration in the cathode depends on the metal ion concentration of the electrolyte itself, which limits the density of the nickel deposition. The chloride is used to improve anode dissolution by reducing polarisation. It also increases the conductivity of the bath [18]. Boric acid serves as a weak buffer to control the pH in the cathode. In its absence, nickel deposits tend to be hard, cracked and pitted [19]. During the process, hydrogen ions are discharged and cling to the growing cathode deposit, which results in pitted plating. To

prevent this pitting, wetting agents which do not appreciably affect the ductility or stress of the plating can be used [20]. In this case sodium lauryl sulphate was used.

Sulphamate electrolytes work over a wide range of concentrations. An average cathode current density of 5 A/dm^2 at a temperature of 50°C is usually used. Under such conditions local current densities of one, half or twice this value will still result in very good deposits.

As explained in subsection 6.2.3, the quality of the plating can be influenced by current density, temperature, pH and agitation, and all of them interrelated, which means that a variable cannot be altered considerably without altering other variables if the quality of the plating is to be maintained.

Taking into account data from the literature, the specifications given by the electrolyte providers [21] and the geometry of the area to be electroplated, the optimum conditions to operate the bath are: strong mixing, temperature of the electrolyte $55\text{-}60^\circ\text{C}$, voltage 1.75 V and distance between the electrodes 5 cm . Under these conditions the electroplating rate is $3\text{-}5 \mu\text{m/h}$. In Fig 6.11 an electroplated nickel layer in a SU-8 mould can be seen. The plating is fairly uniform on the whole surface; there is no pitting or cracks, all the crystals grew with equal rate on the seed layer, so the top area is completely uniform.

Electroplated nickel in SU-8 moulds can be seen in Fig. 6.12. The pillar open in the SU-8 is $100\mu\text{m}$ deep and $40\mu\text{m}$ wide. In Fig. 6.13 we can see a nickel pillar electroplated using a SPR220-7 mould. The SPR220-7 has been removed but the sample hasn't been cleaned thoroughly, as can be observed. This pillar is only $10\mu\text{m}$ in diameter and $45\mu\text{m}$ tall.

In both cases the electroplating was performed under identical conditions. The electroplating was continuous and smooth, this having been achieved due to the complete control over the electrolyte.

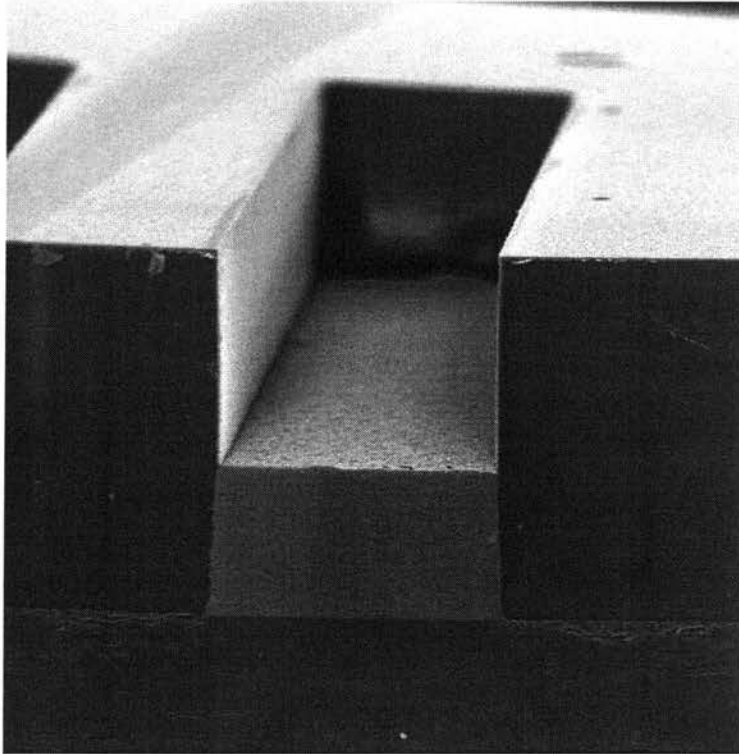


Figure 6.11: Cross-section of electroplated Ni.

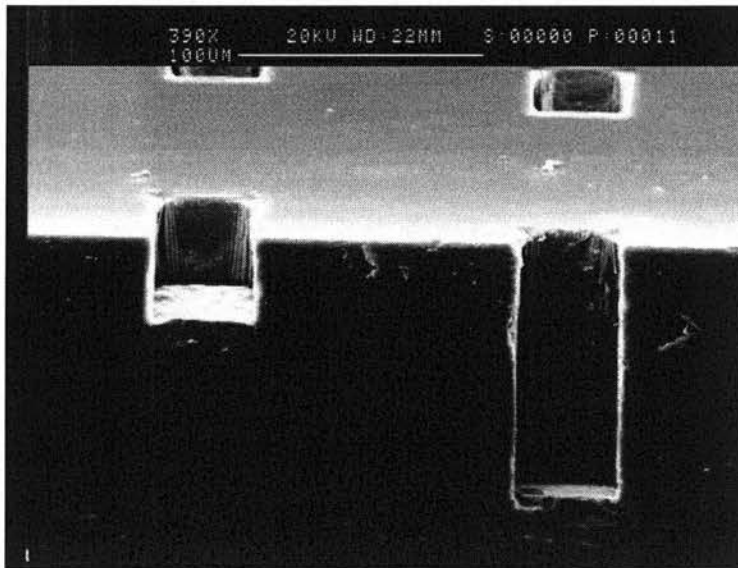


Figure 6.12: Cross-section of a SU-8 mould filled with electroplated Ni.



Figure 6.13: Electroplated nickel pillar using a SPR220-7 mould.

6.3.2.2 Magnetic Properties of the Electroplated Pillars

To determine if the initial aim has been fulfilled, *i.e.* the magnetic moments in the pillars are perpendicular to the cantilever surface, torque magnetometry was used.

The torque magnetometer is mainly used for anisotropy measurements. It is based on the fact that a magnetic dipole $\vec{\mu}$ in an external magnetic field \vec{H} in free space experiences a torque $\vec{\tau}$,

$$\vec{\tau} = \mu_0 \vec{\mu} \times \vec{H}. \quad (6.1)$$

The torque must be measured in a uniform magnetic field. The sample is aligned so that its magnetisation lies in the plane of rotation of the field.

This involves balancing the magnetic torque. The balancing is achieved by the elastic deformation of a torsional wire or cantilever, where the strain gives a measure of the magnetic

moment. The angle ϕ through which the torsion cantilever is twisted is dependent on the length of the cantilever and its shear modulus as well as the torque. ϕ is therefore proportional to the force on the sample,

$$\begin{aligned}\phi &= \text{constant} * \tau \\ &= \text{constant} * \mu_0 \mu \times \bar{H}\end{aligned}\tag{6.2}$$

If α is the angle between the magnetisation μ and the magnetic field \bar{H} ,

$$\phi = \text{constant} * \mu_0 \mu H \sin \alpha.\tag{6.3}$$

The instrument is calibrated using a sample of well known anisotropy, and consequently since μ_0 , \bar{H} and the constant are known, the angle α can be measured and the magnetic moment μ can be calculated.

For a purely isotropic system the magnetisation always lies parallel to the applied field, so the torque on the sample is always zero. On the other hand, for an anisotropic system, there exist magnetisation components perpendicular to the applied field, and therefore, a torque may be generated.

For an anisotropic paramagnet, *i.e.* small coercivity, the susceptibility can be represented as a second order tensor such that the magnetisation is given by Eq. 6.4. Making angular dependent measurements is a very powerful method to probe this anisotropy [22].

$$\bar{M} = \mu_0 [\tilde{\chi}] \bar{H}\tag{6.4}$$

Fig. 6.14 is the angular dependent torque measured on a 40 μm diameter electroplated

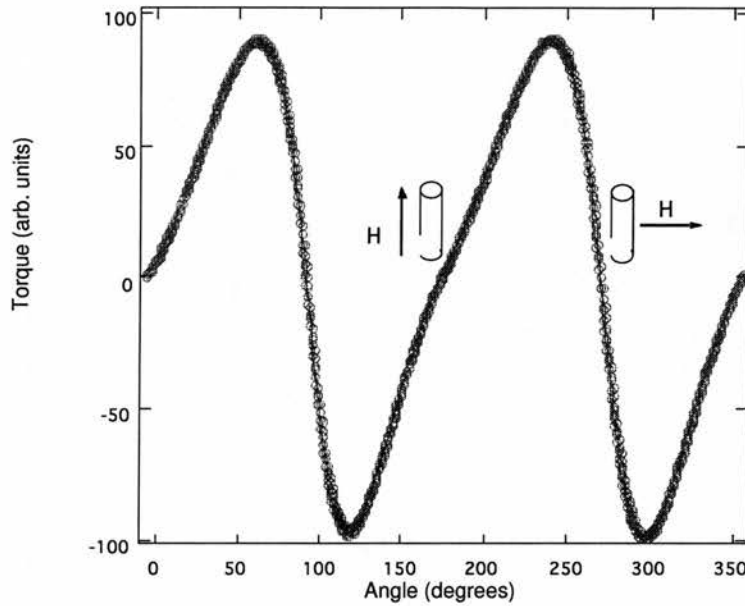


Figure 6.14: Angular dependent torque measurement on a $40\mu\text{m}$ diameter electroplated pillar.

pillar. The asymmetry of the curve shows that overall anisotropy has an easy axis directed perpendicular to the surface of the sample, along the long axis of the pillars.

6.3.3 Summary of Microfabrication Techniques for Creating High-Aspect Ratio Magnetic Particles

Lift-off and ion beam milling techniques were rejected after some experimentation due to the technological limitations of both techniques. The stress created by the $2\mu\text{m}$ of Co along with the limitations of the photolithography would require two major pieces of development. This major development together with the equipment limitations involved too much effort to achieve such a specific application. Therefore, all the effort was then directed towards developing the moulds for electroplating high aspect ratio pillars.

Positive and negative photoresist were considered for electroplating high aspect ratio, 3D structures. It has been demonstrated that the negative photoresist, SU-8, offers very well

defined side walls (90° side walls) and the possibility of achieving very thick layers. SU-8 is therefore a very promising photoresist for very thick layers, but due to the surface stress created by the large area where crosslinking occur destroys the $20\mu\text{m}$ thick diaphragms, making SU-8 only feasible to use when working on bulk silicon. The removal of SU-8 is especially difficult when dealing with such high aspect ratio structures.

SPR220-7 reveals poorer side walls, which are less well defined than those produced using SU-8, and inclined at angles of around 80° . On the other hand, it does not present the high surface stress or the problems associated with the removal of the photoresist.

To electroplate pillars onto micromachined cantilevers for use as magnetic actuators, the cantilever process has to be considered. In this process the electrodeposition is done on $20\mu\text{m}$ thick diaphragms, as explained in Section 4.4. This diaphragm is too thin to cope with the surface stress created by the SU-8, making it unsuitable for this application. Nevertheless, SU-8 is a promising resource for applications in MEMS when thick layers are needed, as for example in the case of accelerometers with disk thicknesses of $200\mu\text{m}$ [23]. SPR220-7 on the other hand, can be used on thin diaphragms making it more suitable for this kind of process and when less thick features are required.

6.4 Cantilevers With Integrated Ni Pillars

Having determined that the optimal way to achieve the high aspect ratio pillars on the paddles is to electroplate them using the SPR220-7 positive photoresist as moulds, this needed to be implemented within the process used to create the cantilevers. It was decided to implement them at the end of the process, after the metallisation. Therefore, the process remains the same as in Section 4.4 up until the metallisation stage. The precise listing of the process can be found in Appendix B.

With the aim of producing cantilevers closer to our requirements, new masks were designed with improvements over the previous batch. In the preliminary study it was found that the ideal dimensions for the cantilevers were $200 \times 200 \mu\text{m}^2$ square paddles and $200 \mu\text{m}$ long legs. These dimensions are to gain a compromise between good sensitivity and feasible handling of the devices. It was also decided that an integrated Wheatstone bridge would lead to a more compact set-up and a reduction of the noise in the measurements. Fig. 6.15 shows the integrated bridge within the chip.

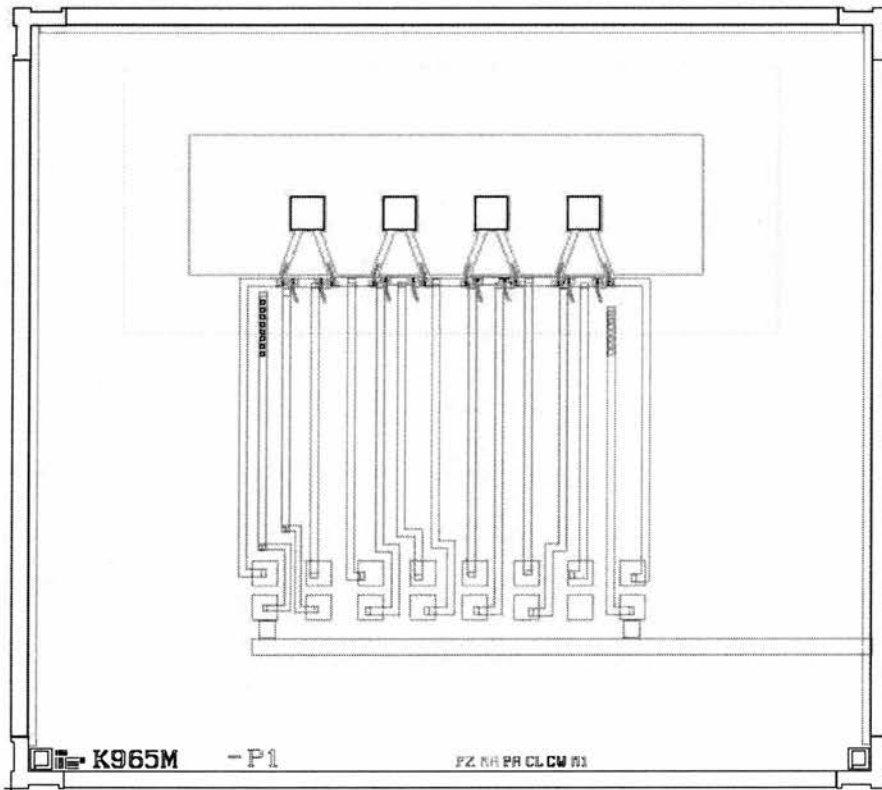


Figure 6.15: Mask design of the integrated Wheatstone bridge within the chip.

Along with these changes, a major change had to be made to allow the electroplating to be done. A conductive seed layer was needed for electroplating and it was decided to incorporate this at the metallisation stage.

All the electroplating tests were done on a titanium seed layer, since to be compatible with the main process the seed layer had to be titanium. This is due to the fact that the

metallisation consists of a thin layer of titanium to improve the adhesion of the aluminium which follows. Two masks were design for the metallisation step. The first mask would define the aluminium tracks and the seed layer, and the second mask would etch away the aluminium from the areas where the titanium seed layer is needed, as can be seen in the sketch in Fig. 6.16.

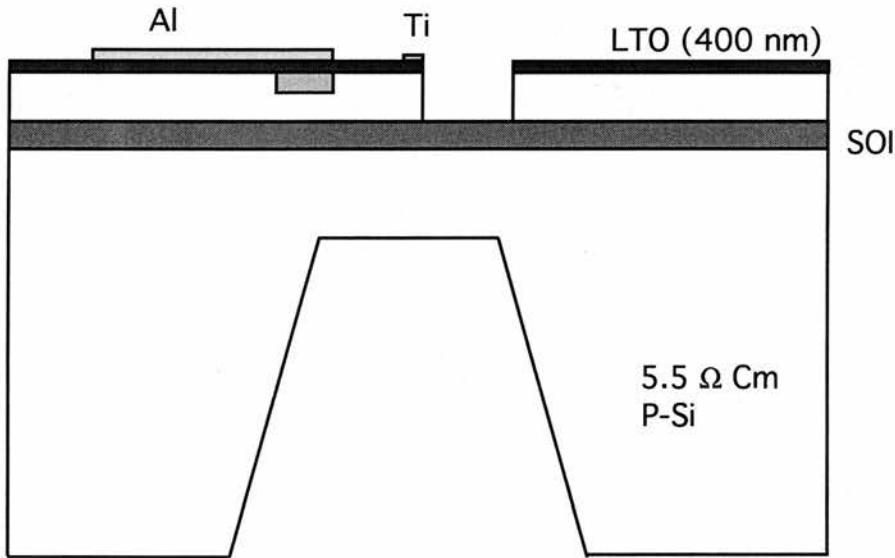


Figure 6.16: Design of the SPR220-7 mould for electroplating the magnetic pillars on the paddles.

To achieve a uniform current density across the wafer it was necessary to design the so called *dummy* sites, patterned sections that are not a functional part of the design. This was implemented on the wafer in the way shown in Fig. 6.17, but the area available was not big enough to over come the problem. Therefore, an outer copper ring was used, clipped to the wafer, to achieve the necessary vertical current lines.

In Fig. 6.18 a picture, taken from above, of a SPR220-7 mould on a paddle can be seen, and Fig. 6.19 is a picture, also from above, of an electroplated mould. These two picture were taken from the very last wafer left out of the initial 6 wafers in the batch, as the other wafers had been broken during the process for different reasons, *e.g.* one wafer broke when spinning due to a fault in the vacuum of the hand spinner, one wafer was slightly over etched

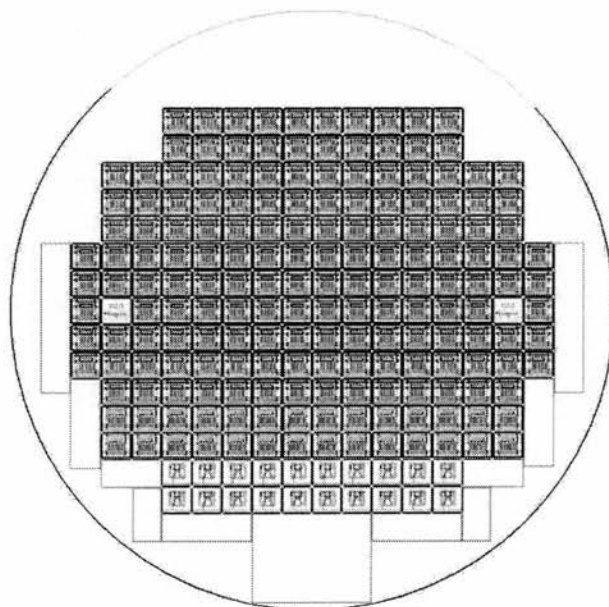


Figure 6.17: Metallisation mask layout, showing the dummy sites surrounding the chips.

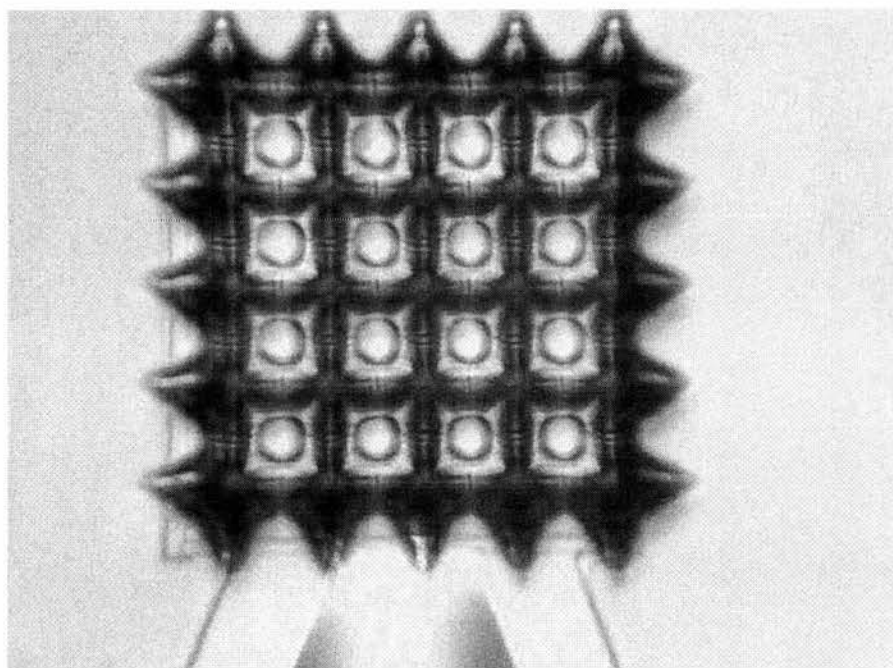


Figure 6.18: SPR220-7 mould on a paddle.

when KOH etching, etc.

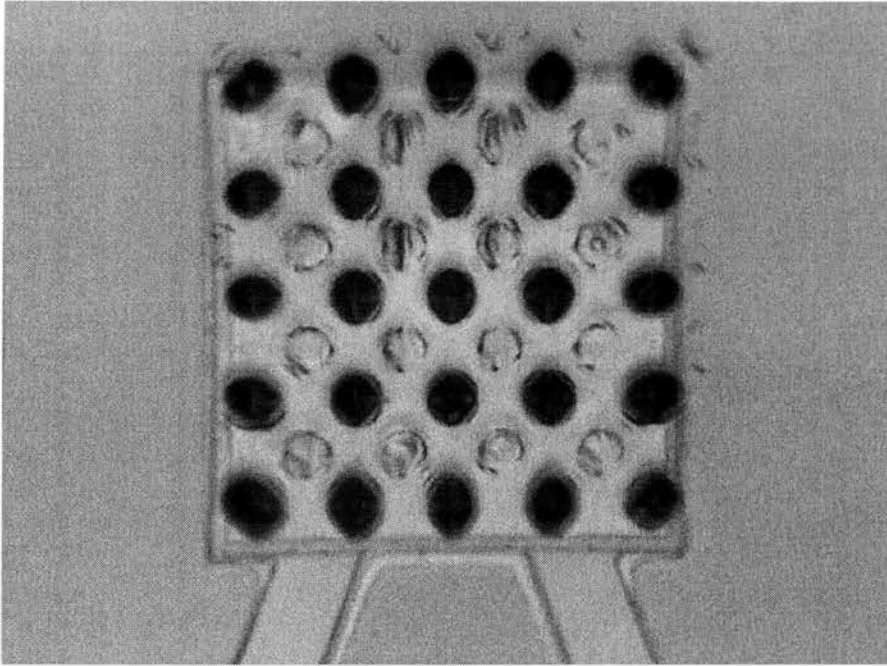


Figure 6.19: Electroplated nickel pillar using a SPR220-7 mould on to a paddle.

After performing the electroplating, the cantilevers needed to be released. To do so, as explained before in Section 4.4, the wafers were dry etched from the back. The SPR220-7 mould was left on to protect the front of the wafer while etching from the back, but the high temperature to which the wafer was brought caused all the solvents trapped in the thick layer of photoresist to escape. This produced a destructive blistering of the photoresist, which damaged the electroplated pillars.

It was deduced that the pre-exposure bake would have to be changed to allow the solvents to evaporate completely. The best way to do this would be to use a ramped temperature cycle on the hot plate.

Unfortunately, at this stage the final wafer broke when handling, so the final stage in which the cantilevers were to be released could not be completed. Nevertheless, the completion of the batch led to several important modification to the process which could be incorporated into the design of the new batch.

On a new batch special care was taken to try to overcome all the problems seen previously. The initial KOH etching was stopped slightly earlier, so that the diaphragms would be $25\mu\text{m}$ thick and the wafers less fragile for handling, the pre-exposure bake for the SPR220-7 was optimised with a ramped temperature cycle, so that there would be hardly any solvent trapped.

The development work described in this chapter has subsequently allowed staff at Southampton University [24] to successfully complete a batch. At the time of writing it just remains for the devices to be finally released.

6.5 Conclusions

The requirement to include the magnetic pillars as part of the microfabrication process led to the study of different techniques capable of producing high aspect ratio structures.

The first attempts made were using the most straight forward techniques, Ion Beam Milling and Lift-off techniques, but due to the lithographic limitations and the problems encountered when evaporating the necessary $2\mu\text{m}$ of cobalt, it was decided to study the possibility of electroplating the pillars. Even though this required major process development, it was the most promising technique, since with this technique small photolithographic features are no longer needed.

A thorough investigation was performed on the different photoresists available for high aspect-ratio moulds. The work was started using the negative photoresist SU-8 as it allows higher aspect ratio structures to be patterned. The type of mask used and the conditions of the wafer when this step needed to be implemented limited the use of the SU-8. The large areas where crosslinking occurred created high stress in the wafer destroying the $20\mu\text{m}$ thick diaphragms. Along with this, the problems found in removing the photoresist discouraged

the use of this photoresist.

A final attempt was made with the positive photoresist SPR220-7, to avoid the problems encountered with the negative photoresist SU-8. It proved to be a successful approach and relatively easy to implement within the main process.

The electroplating was carried out with the electrolyte supplied by TECAN [21], and after finding the optimal conditions, both of the electrolyte and of the cathode geometry, the electrodeposition could be conducted repeatedly.

SPR220-7 does not allow such high aspect ratio structures as SU-8, but as the magnetic measurements show the aspect ratio achieved is high enough to obtain the desired condition of having the magnetic moments align along the axis perpendicular to the surface of the cantilever.

References

- [1] E. Berenschot, *et al.*, 'Thermally Assisted Ion Beam Etching of Polytetrafluorethylene: A New Technique for High Aspect Ratio Etching of MEMS', Proc. IEEE International Whorkshop on MEMS, Sna Diego, CA, 227-284, (1996).
- [2] E.W. Becker *et al.*, 'Fabrication of Microstructures with high aspect ratios and great structural heightths by synchrotron radiation lithography, galvano-forming, and plastic moulding (LIGA process)', Microelectron. Eng., **4**, 35, (1986).
- [3] W. Menz, W. Bacher, M. Harmening and A. Michel, 'The LIGA technique — a novel concept for microstructures and the combination with Si-technologies by injection modeling', Proc. IEEE Micro Electro Mechanical Systems, Nara, Japan, 74-79, (1991).
- [4] M.W. Borner, M. Kohl, F.L. Pantenburg, W. Bacher, H. Hein and W.K. Schomburg, 'Sub-micron LIGA process for movable microstructures', Microelectron. Eng., **30**, 505-508, (1996).
- [5] A. Furuya *et al.*, Proc. IEEE Micro Electro Mechanical Systems, Fort Lauderdale, 56-64, (1993).
- [6] J.M. Shaw *et al.*, 'Negative Photoresist for Optical Lithography', IBM Journal of Research and Development, (1997).

- [7] H. Lorenz, *et al.*, 'Nouvelles Technologies de Microstructuration de Type UV-LIGA et Fabrication de Composants Micromécaniques', Lausanne (CH) (1998).
- [8] M.W. Moreau, *Semiconductors Lithography Principles*, New York: Plenum. 329-333, 488-506, (1988).
- [9] F.A. Lowenheim, *Modern Electroplating*, 3rd ed., John Wiley & Sons INC., New York, (1974).
- [10] A. Manner, S. Harsh and W. Refold, 'Mass Production of Microdevices with Extreme Aspect Ratios by Electroforming', *Plating and Surface Finishing*, **10**, 60-65, (1988).
- [11] *Nickel Plating. Processes and Properties of Deposits*, International Nickel Company., New York, (1967).
- [12] W.T. McFarlen, *Plating*, **57**, 46, (1970).
- [13] O.J. Klingenmaier, *Plating*, **52**, 1138, (1965).
- [14] M.B. Diggin, *Trans. Inst. Met. Finish*, **31**, 243, (1954).
- [15] A.F. Greme, *Plating*, **55**, 594, (1968).
- [16] J.L. Marti, *Plating*, **53**, 61, (1966).
- [17] B.B. Lnapp, *Plating*, **58**, 1187, (1971).
- [18] W.A. Wesley and J.W. Carey, *Trans. Electrochem. Soc.*, **75**, 209, (1939).
- [19] D.J. Macnaughtman, *Mon. Rev. Am. Electrplat. Soc.*, **22**, 71, (1935).
- [20] G.V. Greene, *Trans. Electrochem. Soc.*, **76**, 391, (1939).
- [21] Tecan Components Ltd. Tecan Way, Weymouth, Dorset, DT4 9TU, UK.

- [22] F. Y. Ogrin, *et al.*, 'Development of a Highly Sensitivity Magnetometer Using Microfabricated Silicon Cantilevers', Proc. Conf. on Micromechanics Europe, Paper C 4, (1997).
- [23] M. Kraft, M.M. Farooqui, A.G.R. Evans 'Modelling and Design of an Electrosotatically levitated disk", Proc. Conf. on Micromechanics Europe, Paper C12, Stockholm, (2000).
- [24] L. Grigore, Research Assistant in the ECS department, Southampton.

Chapter 7

Conclusions and Further Work

7.1 Conclusions

The aim of the work described in this thesis is to produce a highly sensitive sensor based on a micromechanical resonating element which would be suitable for routine application in molecular probe chemistry research. Representative cantilever geometries were fabricated and tested and results compared to the theoretical results from the design study. This allowed both the theoretical modelling techniques used and the structures developed to be evaluated and conclusions to be drawn regarding their suitability and performance.

The review of μ TAS compatible detection systems showed an impending need for novel sensors. This is unsurprising given that the current technology encounters two major disadvantages. Firstly, end point determination is often the only option available. Secondly, chemical labelling may be required for specific detection. New approaches towards combining the mechanical properties of MEMS with biological materials are being taken to achieve portable and cost effective specific chemical detection systems. The so-called gravimetric devices, based on the detection of small mass changes, are the main approach in this new

field.

Much effort has been directed towards the development of piezoelectric crystal based gravimetric devices. Nevertheless, practical limitations with the piezoelectric crystals suggest the need for an alternative approach. These limitations can be overcome by oscillating cantilevers, since their use simplifies the electronic arrangement and brings the final devices closer towards that required for the μ TAS technology. The design of such cantilevers will depend upon many factors defined by the nature of the application.

Since the ultimate application of the cantilevers is for dynamic monitoring of reactions, both the driving and sensing mechanism of the cantilever play an important role. For a clean and direct excitation mechanism a magnetic drive was chosen. It was decided that the most practical mechanism was the magnetic force mode since it simplifies the response of the cantilever and improves the signal-to-noise ratio for the dynamic mode. Piezoresistors were considered as the sensing elements. These can be incorporated within the cantilever legs, forming an integrated component which allows the devices to be operated in diffuse scattering liquids.

The analysis of micromechanical cantilevers was aimed at maximising the sensitivity, by maximising the Q-factor and optimising the performance characteristics. Taking into account the fact that a low force constant is needed for maximum sensitivity, the geometrical and dimensional dependence of the force constant was calculated using basic mechanics. It was concluded that long and thin cantilevers give the lowest spring constant and therefore the higher sensitivity. However, since the cantilevers are to be used as gravimetric devices, the relative change of mass should also be considered when designing the cantilevers, and a compromise between spring constant and relative change of mass should be achieved. The cantilever paddles were designed after a thorough study of the theoretical properties. Nevertheless, the results implied a compromise between the different parameters for optimisation of the cantilevers and therefore a variety of dimensions were used for the first generation of

devices.

A key development of this research project involved using the stress levels at the cantilever's fixed boundaries as the sensing mechanism, since the piezoresistors detect that stress. This requires accurate calculation of nodal stress values whilst performing a modal analysis to determine resonant frequencies. All the results gained from FEA were in good agreement with the predicted values. FEA results also predicted the mass sensitivities of the different models proposed, giving the second generation of devices a much higher mass sensitivity.

For the magnetic excitation, the force mode was chosen since it induces a bigger deflection on the cantilever than the torque mode. For the initial experiments using the devices from the first generation batch, a magnetic particle had to be attached manually to the cantilever paddle. Even with an experienced hand the biggest cantilever paddles were needed to successfully attach the magnetic particles. A simple Wheatstone bridge was used to detect the signal along with a lock-in amplifier. These preliminary results were very encouraging since they confirm the predictions made by the FE analysis and demonstrate the potential of this method for dynamic monitoring detection.

It soon became evident however, that the magnetic particles should be integrated within the fabrication process since the repeatable fabrication of the cantilevers is of fundamental importance in achieving suitable structures for mass-produced sensor applications. This led to the study of different techniques capable of producing high aspect ratio magnetic structures. After the failure of ion beam milling and lift-off techniques, it was decided to approach the problem with electrodeposition.

Following a thorough investigation on the different available photoresists for high aspect-ratio moulds, it was decided to use the negative photoresist SU-8. SU-8 proved to be a suitable photoresist when used in bulk silicon. However, the use of this polymer resist on

20 μ m diaphragms was impractical due to the large surface stress created by the crosslinkage. A final attempt was carried out with the positive photoresist SPR220-7, which was successful. SPR220-7 does not allow such high aspect ratio structures as SU-8. Nonetheless, the magnetic measurements show that the aspect ratios are sufficient to align the moments along the axis perpendicular to the surface of the cantilever.

This work has demonstrated the feasibility of this technology for application in specific chemical detection, and forms the basis for future development work. Some suggestions for how this work might progress further are discussed below.

7.2 Future Work

The development of cantilever devices for operation in liquids presents two major drawbacks. For bending mode operation there exists long-term drift of the cantilever deflection. For the resonating devices, the quality factor Q is reduced by roughly two orders of magnitude when immersed in a liquid [1]. The quality factor is defined by $Q = m(2\pi)f_0/\gamma$, where γ is the damping constant of the cantilever, and effectively defines the line width of the resonance peak $\Delta f_0/f_0 \approx 1/Q$. The frequency and hence mass resolution of a resonating device is thus severely reduced under liquids. Nonetheless, by careful experimental design and by choosing an appropriate frequency, SFM images have been successfully obtained under liquids e.g. [2, 3]. Suitable choice of shape and composition of magnetic material and careful design and placement of the driving coil can lead to large applied forces or torques. This may be particularly important under liquids due to the inherently low Q -factor, since the force required to excite a cantilever at resonance at a particular amplitude is proportional to k/Q .

The low- Q -factor typically obtained under liquids would thus seem like a severe limitation on achieving high signal levels and good frequency resolution for application in specific chemical detection. A promising way forward has been proposed recently e.g. [4, 5, 6]. In

this scheme active feedback is used to greatly enhance the effective Q -factor, whereby part of the time-dependent cantilever response is phase shifted by $\pi/2$ and fed back into the driving signal. This leads to an effective damping constant $\gamma_{eff} = \gamma - G/\omega$, where G is the gain of the feedback signal and ω is the angular frequency, and an effective quality factor $Q_{eff} = m\omega/\gamma_{eff}$. Care must thus be taken, since too large a feedback will lead to a negative damping and self-sustained oscillations. In order to lock the system into resonance, a phase locked loop (PLL) is also employed to maintain a $\pi/2$ phase difference between the driving signal and the cantilever response, as is the case for a dissipative resonator at the point of energy resonance. Using this approach, quality factors of up to 1000 have been achieved under liquids, although in practice this is usually limited to a few hundred to maintain stability.

For chemical detection we also conclude from the foregoing discussion that one requires a large area for adsorption, preferably at the end of the cantilever if it is intended to concentrate on contributions to the shift of the resonant frequency due to the changes of mass. Other considerations for the design of a system might include simplicity of operation and complexity of ancillary equipment.

In order to undertake specific chemical detection, schemes must be developed which allow molecular probes to be attached to the surface of the device. There are two basic approaches to this problem. The first, most desirable approach is to covalently bond a material to the surface onto which a highly specific molecular probe may subsequently be attached. The second method is to non-covalently attach a coating to the surface, the molecules of which contains a specific molecular probe. This could be, for instance, the hydrophilic attraction of a protein that is conjugated with an antibody. One problem here is the need to subsequently block the possibility of non-specific attachment, of the target or an impurity species, directly to the protein. Ultimately the first approach will give much greater control over surface modification, but may be harder to achieve.

One possible approach to covalently bonding to silicon involves the use of organofunctional silanes followed by covalent attachment of a biological molecule to the functional group of the silane. This type of approach is commonly used on glass substrates [7]. For modification of silicon surfaces an oxide layer is required, although there exists the possibility of using the thin native oxide which is always present. The oxide must be activated, usually by reaction with a peroxide solution, to yield hydroxyl groups at the surface. One suitable material is (3-mercaptopropyl) trimethoxysilane (3-MPTS), where the reaction is thought to proceed by the initial hydrolysis of hydroxyl groups that can covalently interact with the hydroxyl groups present on the surface. The result is that one or more covalent Si-O bonds form between the molecule and the surface. For the case of MPTS, the terminating thiol group may subsequently be used to covalently bond to a specific biological molecular probe, including oligonucleotides [7]. The use of the native oxide could be important for microcantilever based systems, since it is already present on the paddle surface following processing, and negates the need for further surface coating or oxide growth.

References

- [1] J. Tamayo, *et al.*, Appl. Phys. Lett. **64**, 2454, (1994).
- [2] C.A.J. Putman *et al.*, 'Tapping Mode Force Microscopy in Liquid' App. Phys. Lett. **64** (18), 2454-2456, (1994).
- [3] T.E. Schäffer *et al.*, 'Studies of Vibrating Atomic Force Microscope Cantilevers in Liquid', J. Appl. Phys. **80** (7), 3622-3627, (1996).
- [4] J. Tamayo *et al.*, 'piconewton Regime Dynamic Force Microscopy in Liquid', Appl. Phys. Lett. **77**(4), 582-584, (2000).
- [5] A.D.L. Humphris, *et al.*, Langmuir, **16**, 7891, (2000).
- [6] J. Tamayo *et al.*, 'Chemical Sensors and Biosensors in Liquid Environment Based on Microcantilevers with Amplified Quality Factor', Ultramicroscopy, **86**, 167-173, (2001).
- [7] C. Halliwell and A.E.G. Cass, Anal. Chem., **73**, 2476, (2001).

Appendix A

Detailed Resolution of the Mechanical Properties

A.1 Cantilevers Design Criteria and Selection

Based on basic mechanics and assuming that the lateral stress is zero, the force constant of the cantilever paddle is determined. First the deflection of the cantilever is calculated using the equation of deflection Eq. A.1,

$$EI_z \frac{d^2 y}{dx^2} = Fx \quad (\text{A.1})$$

with the following boundary conditions:

$$x = L_1 \quad , \quad \frac{dy}{dz} = 0 \quad (\text{A.2})$$

$$x = L_1 \quad , \quad y = 0 \quad (\text{A.3})$$

Where E is the Young's modulus; I_z the second moment of area of the cross-section with respect to the neutral axis Z ; L_1 the total length of the cantilever paddle and F a single force at the end of the cantilever.

The second moment of aread of the cantilever is defined by,

$$I_z = \int_{-\frac{t}{2}}^{\frac{t}{2}} \left[\int_{-\frac{\omega}{2}}^{\frac{\omega}{2}} y^2 dy \right] dz \quad (\text{A.4})$$

This integral should be solved for the two different geometries, for when x goes from 0 to L , and for when x goes from L to L_1 . Therefore we have,

$$I_z = \begin{cases} \frac{1}{12} L t^3, & x \in (0, L) \\ \frac{1}{6} \omega t^3, & x \in (L, L_1) \end{cases} \quad (\text{A.5})$$

where L , t , and ω , are the size of the paddle, the thickness and the width of the cantilever respectively.

Therefore, Eq. A.1, is also solved considering these two regions. For x in the range of 0 to L we have:

$$\begin{aligned} \int_0^x d \frac{dy}{dx} &= \frac{dy}{dx}(x) - \frac{dy}{dx}(0) \\ &= \int_0^x \frac{Fx}{EI_{z1}} dx \\ &= \frac{F}{EI_{z1}} \frac{x^2}{2} \end{aligned} \quad (\text{A.6})$$

Integrating Eq. A.1 for x in the range from L to L_1 , we have:

$$\begin{aligned}
\int_0^x d\frac{dy}{dx} &= \frac{dy}{dx}(x) - \frac{dy}{dx}(0) \\
&= \int_0^L \frac{Fx}{EI_{z1}} dx + \int_L^x \frac{Fx}{EI_{z2}} dx \\
&= \frac{F}{EI_{z1}} \frac{L^2}{2} + \frac{F}{EI_{z2}} \frac{x^2 - L^2}{2}
\end{aligned} \tag{A.7}$$

Now, using the boundary condition Eq. A.2,

$$\begin{aligned}
\frac{dy}{dx}(L_1) - \frac{dy}{dx}(0) &= 0 - \frac{dy}{dx}(0) \\
&= \frac{F}{EI_{z1}} \frac{L^2}{2} + \frac{F}{EI_{z2}} \frac{L_1^2 - L^2}{2}
\end{aligned} \tag{A.8}$$

Introducing this result in Eq. A.8, the first derivative for $x \in (0, L)$ is,

$$\frac{dy}{dx}(x) = \frac{F}{EI_{z1}} \frac{X^2 - L^2}{2} - \frac{F}{EI_{z2}} \frac{L_1^2 - L^2}{2} \tag{A.9}$$

and for $x \in (L, L_1)$,

$$\frac{dy}{dx}(x) = \frac{F}{EI_{z2}} \frac{x^2 - L_1^2}{2} \tag{A.10}$$

Integrating Eq. A.10 for x from 0 to L_1 , the deflection of the cantilever is obtained.

$$\begin{aligned}
\int_0^x dy &= y(x) - y(0) \\
&= \int_0^L \left[\frac{F}{2EI_{z1}}(x^2 - L^2) - \frac{F}{2EI_{z2}}(L_1^2 - L^2) \right] dx + \int_L^x \frac{F}{2EI_{z2}}(x^2 - L_1^2) dx \quad (\text{A.11}) \\
&= -\frac{FL^3}{3EI_{z1}} + \frac{F}{2EI_{z2}} \left(\frac{x^3}{3} - L_1^2 x + \frac{2L^3}{3} \right)
\end{aligned}$$

Now, using the boundary condition Eq. A.2, and substituting I_{z1} and I_{z2} , the deflection $y(0)$ of the cantilever becomes,

$$\begin{aligned}
y(L_1) - y(0) &= -y(0) \\
&= -\frac{2F}{E\omega t^3} (2\omega L^2 - (L^3 - L_1^3)) \quad (\text{A.12})
\end{aligned}$$

Therefore,

$$y(0) = \frac{2F}{E\omega t^3} (2\omega L^2 - (L^3 - L_1^3)) \quad (\text{A.13})$$

The force constant is defined as,

$$F = ky(0) \quad (\text{A.14})$$

and, k is then

$$\begin{aligned} k &= \frac{F}{y(0)} \\ &= \frac{E\omega t^3}{2(2\omega L^2 + L_1^3 - L^3)} \end{aligned} \tag{A.15}$$

This is proportional to the thickness to the cube and to the effective width of the cantilever arms, and is inversely proportional to the total length to the cube of the cantilever paddle. Therefore a small force constant is achieved with thin and long cantilevers.

A.2 β Correction Factor for the Piezoresistors

To determine the sensitivity of the piezoresistors it is necessary to take into consideration the fact that the piezoresistors have a distribution along the stress direction and along the depth of the cantilever. Therefore, it is necessary to determine β the correction factor, which allows for this real approximation.

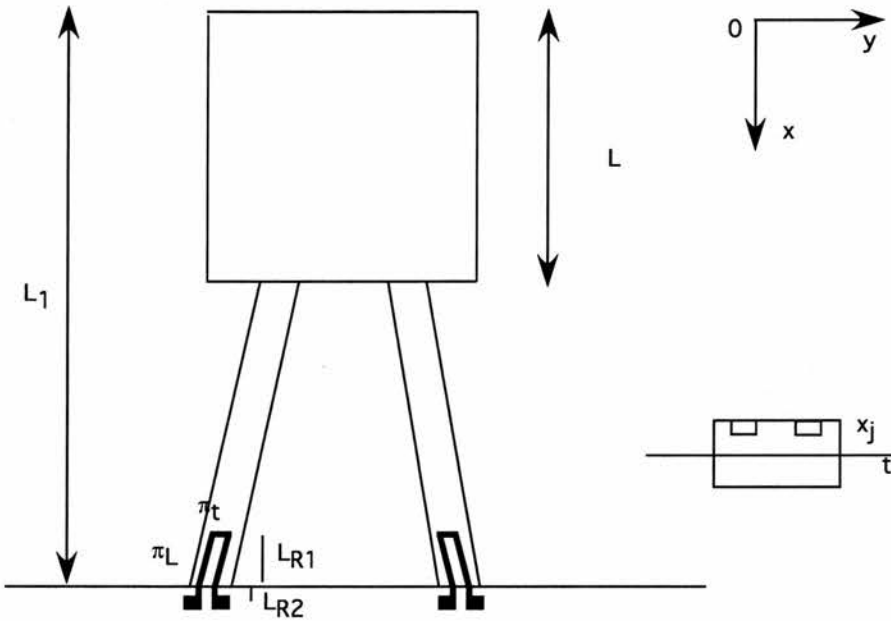


Figure A.1: A sketch of the resistors in the cantilever. Where L_{R1} is the length of the resistor along the cantilever, L_{R2} is the extension of the resistor beyond the fixed edge, and x_j is the junction depth.

The features to be taken into consideration are sketched in Fig. A.1. Here, it can be assumed that there is no stress beyond the fixed edge of the cantilever. Hence, the part of the resistor located on the cantilever, R_1 , is in the maximum stress area. The piezoresistive output can for the ideal case, and for the real case is given by Eq. A.16 and Eq. A.17,

$$\begin{aligned}\frac{\Delta R}{R} &= S_{ideal}y(0) \\ &= \frac{\Delta R_1}{R_1}\end{aligned}\tag{A.16}$$

$$\begin{aligned}\frac{\Delta R}{R} &= S_{real}y(0) \\ &= \frac{\Delta R_1}{R_1 + R_2}\end{aligned}\tag{A.17}$$

where S_{ideal} and S_{real} are the real and ideal piezoresistive sensitivity, and $y(0)$ is the deflection of the cantilever. From Eq. A.16 and Eq. A.17, the first modification factor is,

$$\beta_1 = \frac{R_1}{R_1 + R_2}\tag{A.18}$$

Since the resistors also have a junction depth, and the maximum stress is only located on the surface of the fixed edge of the cantilever, a second modification factor, β_2 must also be considered. Therefore, let δR at (x, y) be the resistor element defined by,

$$\delta R = \frac{\rho dx}{\omega dy}\tag{A.19}$$

where ρ is the resistivity, dx is the length increment of the resistor in the x direction, dy is the depth increment of the resistor, and ω the width of the resistor. Following the same reasoning as in subsec 2.5.2, the transverse piezoresistive coefficient is neglected, and the fractional change of the resistor becomes [1],

$$\begin{aligned} \frac{\Delta(\delta R)}{\delta R} &= \pi_l \sigma_l \\ &= \frac{\pi_l F_c y(0) x y}{I_z} \end{aligned} \tag{A.20}$$

where π_l is the longitudinal piezoresistive coefficient, σ_l is the longitudinal stress, F_c is the force constant of the cantilever, x and y the position of the resistor element, and I_z the inertial moment.

Substituting Eq. A.19 into Eq. A.20,

$$\Delta(\delta R) = \frac{\pi_l F_c x y \rho dx}{I_z \omega dy} \tag{A.21}$$

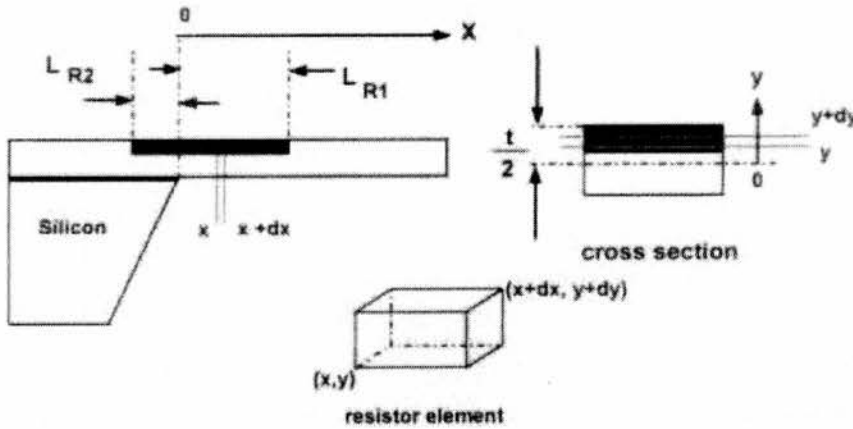


Figure A.2: A sketch of the cross-section of the resistors in the cantilever.

Integrating Eq. A.21 with x from 0 to L_{R1} and y from $\frac{t}{2} - x_j$ to $\frac{t}{2}$, see Fig. A.2, the total change in the resistance R_1 is then given by,

$$\Delta R_1 = \frac{\pi_l F_c L_1 t y(0)}{2 I_z} \frac{(1 - \frac{L_{R1}}{2 L_1}) 2 x_j}{t \ln(\frac{t}{t - 2 x_j})} R_1 \tag{A.22}$$

Comparing this expression with the corresponding equation for the ideal case, Eq. 2.36,

$$\frac{\Delta R}{R} = \frac{\pi_l L_1 t F_c y(0)}{2I_z} \quad (\text{A.23})$$

the correction factor β_2 can be deduced,

$$\beta_2 = \frac{2x_j(1 - \frac{LR_1}{2L})}{t \ln(\frac{t}{t-2x_j})} \quad (\text{A.24})$$

Therefore, the total correction factor β is given by,

$$\begin{aligned} \beta &= \beta_1 \cdot \beta_2 \\ &= \frac{R_1}{R_1 + R_2} \frac{2x_j(1 - \frac{LR_1}{2L})}{t \ln(\frac{t}{t-2x_j})} \end{aligned} \quad (\text{A.25})$$

In summary, the fractional change of the piezoresistor from an ideal model is given by,

$$\frac{\Delta R}{R} = \frac{\pi_l L_1 t F_c y(0)}{2I_z}$$

and the fractional change of a piezoresistor from the rfeal model is given by,

$$\frac{\Delta R}{R} = \beta \frac{\pi_l L_1 t F_c y(0)}{2I_z}$$

References

- [1] K. Yamada *et al.*, 'Nonlinearity of the Piezoresistance Effect of P-type Silicon Diffused Layers', IEEE Trans. Electron. Devices, **29** (1), 71-77, (1982).

Appendix B

Process Listings

B.1 Simple Cantilever Paddles

B	R	G	No	1	2	3	4	5	6	ID	Description	Doc
										k1740s	JH-Naiara Elejalde Micromachined magnetometers	
										red1	backside	
										g1	BACK ETCHING IN KOH	
1										G-S6	Title page 6 wafers ***SOI*** p-type Si thickness 3.5 micron	0
2										G-1P	Lithography Notes K714M	0
3										G-1	Notebook page	0
											BACK ETCHING IN KOH	0
4										W-C1	RCA clean	0
5										F4-W106	Initial ox. 600nm+-20nm, 1100degC, IdO2_rmpO2,x>wetO2,umldN2	0
6										LN-160	Deposit Si3N4 160nm +- 20nm on BOTH SIDES	0
7										P-GB	Photolith mask K714M BK, Dark Field 2.2um Resist on BACKS Fronts protected	0
8										P-RHBW	* Hardbake for wet etch	0
9										P-0	Paint resist around edges	0
10										P-RHBD	* Hardbake for dry etch	0
11										D-NO1S	Etch Si3N4. Anisot. from BACKS OPT80+ CHF3+Ar	0
12										WH-7E1	Wet etch oxide, 7:1 BHF 25degC. To hydrophobic Si + 20secs.	0
13										P-RS	Resist strip	0
14										WS-3	Etch silicon in KOH leave ~20um Si film	0
15										WN-1	+ Strip/Wet etch Si3N4, Orthophosphoric acid 160degC	0
										red2	frontside	
										g2	TP mask for alignment	
											TP FOR ALIGNMENT	0
16										W-C2	* Fuming Nitric acid clean, 2nd pot only	0
17										P-GDF	Photolith: Double sided alignment: K714M Mask TP, Light Field on FRONTS. Use special alignment mark - ASK JFC or GE 2.2um Resist	0
18										P-RHBW	* Hardbake for wet etch	0
19										D-D60	Descum: 1 min. SRS barrel O2	0
20										WH-7E1	+ Wet etch oxide, 7:1 BHF 25degC. To hydrophobic Si + 20secs.	0
21										P-RS	Resist strip	0
										g3	IMPLANT B+ for whole area	
											BLANKET IMPLANT B+	0
22										W-C2	Fuming Nitric acid clean, 2nd pot only	0
23										IB-3035	Implant Boron: 5E13 B+ 30KeV Wafer fronts	0
										g4	PIEZORESISTOR	
											PIEZORESISTOR	0
24										W-C1	RCA clean	0
25										F5-0	Dry oxidation: 100nm at 950degC	0
26										P-G2	Photolith mask K714M PZ, Dark Field: 2.2um resist	0
27										P-RHBI	* Hardbake for wet etch and Implant	0
28										D-D60	Descum: 1 min. SRS barrel O2	0
29										WH-7E1	+ Wet etch oxide, 7:1 BHF 25degC. To hydrophobic Si + 20secs.	0
30										IP-0	Implant PHOS+, 5E14 @ 88KeV	0
31										P-RS	Resist strip	0

B	R	G	No	1	2	3	4	5	6	ID	Description	Count
										g5	CONTACT WINDOW DOPING	
											CONTACT WINDOW DOPING	0
			32							W-C2	Fuming Nitric acid clean, 2nd pot only	0
			33							P-G2	Photolith mask K714M NA, Dark Field: 2.2um Resist	0
			34							P-RHBI	* Hardbake for implant	0
			35							IA-8055	Implant Arsenic: 5E15 As+ 80KeV	0
			36							P-RS	Resist strip	0
										g6	SUBSTRATE CONTACT DOPING	
											SUBSTRATE CONTACT DOPING	0
			37							W-C2	Fuming Nitric acid clean, 2nd pot only	0
			38							P-G2	Photolith mask K714M PA, Dark Field: 2.2um Resist	0
			39							P-RHBI	* Hardbake for wet etch and implant	0
			40							D-D60	Descum: 1 min. SRS barrel O2	0
			41							WH-7E1	Wet etch oxide, 7:1 BHF 25degC. To hydrophobic Si + 20secs.	0
			42							IBF-7055	Implant BF2+: 5E15 BF2+ 70KeV	0
			43							P-RS	Resist strip	0
										g7	PATTERN CANTILEVER	
											PATTERN CANTILEVER	0
			44							W-C1	RCA clean	0
			45							LO-400	LTO deposition: 400nm +/- 40nm at 400degC SiH4 and O2	0
			46							F10-8	Density LTO then neutral resistor, 1000degC 30min dryO2. Xp=0.5um, R=100-200/ohm	0
			47							P-G2	Photolith mask K714M CL, Dark Field: 2.2um Resist	0
			48							P-RHBW	* Hardbake for wet etch	0
			49							D-D60	Descum: 1 min. For OPTICAL resist SRS barrel O2	0
			50							WH-7E1	Wet etch oxide, 7:1 BHF 25degC. To hydrophobic Si + 20secs.	0
			51							D-S2S	Deep etch Si. ~3.5um Partially anisot. OPT80+ SF6 THROUGH TO SOI OXIDE	0
			52							P-RS	Resist strip	0
										g8	CONTACT WINDOWS	
											CONTACT WINDOWS	0
			53							W-C2	Fuming Nitric acid clean, 2nd pot only	0
			54							P-G2	Photolith mask K714M CW, Dark Field 2.2um Resist:	0
			55							P-RHBW	* Hardbake for wet etch	0
			56							D-D60	Descum: 1 min. SRS barrel O2	0
			57							WH-7E1	Wet etch oxide, 7:1 BHF 25degC. To hydrophobic Si + 20secs.	0
			58							P-RS	Resist strip	0
										g9	DEPOSIT METAL FILM	
											DEPOSIT METAL FILM	0
			59							W-C2	Fuming Nitric acid clean, 2nd pot only	0
			60							WH-2D2	Dip etch, 20:1 BHF 25degC, 30 seconds. (Pre-metallisation)	0
			61							MS-TA10	Sputter 1000nm Ti-Al/Si 1% in TRIKON SIGMA	0
			62							P-G2	Photolith mask K714M M1, Light Field: 2.2um resist	0
			63							P-RHBW	* Hardbake for wet etch	0
			64							WM-AST	Wet etch Al/Si+Ti, 3 Stage etch: Phos acid, Ti etch, Defreckle.	0
			65							P-RS	Resist strip	0
			66							F9-H35	Alloy/ Anneal: 30mins H2/N2 350degC 5*N2,30'H2/N2,5*N2.	0
										red3	photoresist to protect metal film and dry etching backside to release cantilever	
										g10	RELEASE CANTILEVER	
											RELEASE CANTILEVER	0
			67							P-G2	Photolith mask K714M MP, Light Field: 2.2um resist	0
			68							P-RHBW	* Hardbake for wet etch	0
			69							D-S2S	Trench etch Si, BACKS OPT 80+ SF6 ~14um through to SOI oxide	0
			70							WH-7E1	Wet etch oxide (front + back), 7:1 BHF 25degC. To hydrophobic Si + 20secs.	0
			71							P-RS	Resist strip	0
			72							P-8	Apply resist for sawing	0
			73							G-2	See Naiera for sawing instructions	0
			74							P-RS	Resist strip	0

B.2 Cobalt Etching with Ion-bem Miller

B	R	G	No	1	2	3	4	5	6	ID	Description	Con
										k1864s	NE-cobalt etching with ion-beam miller	
										r1		
										g1		
			1							G-S12	Title Page: 4 wafers, MATERIAL-P-100, 17-33 test (PVM)	0
			2							G-1P	Lithography Notes	0
			3							G-1	Notebook page	0
			4							W-C2	* Fuming Nitric acid clean, 2nd pot only WAFERS #1,3 ONLY	0
			5							W-C1	* RCA clean WAFERS #2,4 ONLY	0
			6							F4-W006t	* Wet oxidation: 600nm, 1000degC: LrO2,x*WO2,uN2	0
			7							G-3	Evaporate at same time as Co Lift-off Batch (nelitt)	0
			8							ME-0	Evaporate 40nm Cr + 2um Co WAFERS #1,2 ONLY WAFERS COULD BE Au CONTAMINATED	0
			9							ME-0	Evaporate 40nm Cr + 2um Co SHADOW MASK WAFERS#3,4 ONLY WAFERS COULD BE Au CONTAMINATED	0
			10							P-GSX	* STEPPER Photolith: reticle K936R, Light Field: (1.1um resist) (for wafers with GOLD)	0
			11							P-RHBX	* Hardbake (for wafers with GOLD)	0
			12							B-0	Ion-Beam Mill: 2um Co	0
			13							P-RSX	* Resist strip (for wafers with GOLD)	0
			14							X-0	General inspection stage	0

B.3 Cobalt Lift-off

B	R	G	No	1	2	3	4	5	6	ID	Description	Con
										k1865s	NE-Cobalt lift-off	
										r1		
										g1		
			1							G-S12	Title Page: 4 wafers, MATERIAL: P-100, 17-33 test (PVM)	0
			2							G-1P	Lithography Notes	0
			3							G-1	Notebook page	0
			4							W-C2	* Fuming Nitric acid clean, 2nd pot only WAFERS #1,3 ONLY	0
			5							W-C1	* RCA clean WAFERS #2,4 ONLY	0
			6							F4-W006t	* Wet oxidation: 600nm, 1000degC: LrO2,x*WO2,uN2	0
			7							P-GL1	* PMGI Lift-off process: Photolith mask K936M, Dark Field, 2um	0
			8							P-GL3	* PMGI Lift-off Hardbake + Descum	0
			9							ME-0	Evaporate 40nm Cr + 2um Co WAFERS COULD BE Au CONTAMINATED	0
			10							P-GL5	* LIFT-OFF metal (PMGI process)	0
			11							X-0	General inspection stage	0

B.4 Test for Electroplating

B	R	G	No	1	2	3	4	5	6	ID	Description	Count
										k1957s	NE-test wafer for electroplating	
										r1		
										g1		
1										G-S12	Title Page: 4 wafers. MATERIAL: 17-33 test wafers	4
2										G-1P	Lithography Notes	4
3										G-1	Notebook page	4
4										W-C1	* RCA clean	4
5										F4-W001	* Wet oxidation 100nm+-10nm, 1000degC, 10'O2,x>wetO2,30'N2.	4
6										P-G2	* Photolith mask K965M CW, Dark Field: nom. 2.2um resist	4
7										P-RHBW	* Hardbake for wet etch	4
8										D-D60	* Descum: 1 min. For OPTICAL resist Technics uWave Asher	4
9										WH-7E1	+ Wet etch oxide, 7:1 BHF 25degC. To hydrophobic Si + 20secs.	4
10										IBF-7055	* Implant BF2+: 5E15 BF2+ 70KeV (CMOS P-ch S&D through gate ox.)	4
11										P-RS	* Resist strip	4
											SEED LAYER	0
12										W-C2	* Fuming Nitric acid clean, 2nd pot only	4
13										W-C1	* RCA clean	4
14										RA-1	RTA implant activation 10secs 1100degC (Std.CMOS S & D)	4
15										WH-20D	Dip etch, 200:1 BHF (Pre-metallization for silicided CW)	4
16										MS-B	Sputter 100nm Ti in TRIKON SIGMA sputtered films. RESIST PROHIBITED	4
17										P-G2	* Photolith mask K965M M1, Light Field: 2.2um resist	4
18										G-2	* See Engineer: INSPECT	4
19										P-RHBW	* Hardbake for wet etch	4
20										WM-AST	Wet etch Ti	4
21										P-RS	* Resist strip	4
22										W-C3	* Fuming Nitric Acid clean, metallised wafers	4
23										F9-H35	* Alloy/ Anneal: 30mins H2/N2 350degC 5'N2,30'H2/N2,5'N2. 5 more wafers same process	4
												0
24										W-C1	* RCA clean	5
25										F4-W001	* Wet oxidation 100nm+-10nm, 1000degC, 10'O2,x>wetO2,30'N2.	5
26										P-G2	* Photolith mask K965M CW, Dark Field: nom. 2.2um resist	5
27										P-RHBW	* Hardbake for wet etch	5
28										D-D60	* Descum: 1 min. For OPTICAL resist Technics uWave Asher	5
29										WH-7E1	+ Wet etch oxide, 7:1 BHF 25degC. To hydrophobic Si + 20secs.	5
30										IBF-7055	* Implant BF2+: 5E15 BF2+ 70KeV (CMOS P-ch S&D through gate ox.)	5
31										P-RS	* Resist strip	5
											SEED LAYER	5
32										W-C2	* Fuming Nitric acid clean, 2nd pot only	5
33										W-C1	* RCA clean	5
34										RA-1	RTA implant activation 10secs 1100degC (Std.CMOS S & D)	5
35										WH-20D	Dip etch, 200:1 BHF (Pre-metallization for silicided CW)	5
36										MS-B	Sputter 100nm Ti in TRIKON SIGMA sputtered films. RESIST PROHIBITED	5
37										P-G2	* Photolith mask K965M M1, Light Field: 2.2um resist	5
38										G-2	* See Engineer: INSPECT	5
39										P-RHBW	* Hardbake for wet etch	5
40										WM-AST	Wet etch Ti	5
41										P-RS	* Resist strip	5
42										W-C3	* Fuming Nitric Acid clean, metallised wafers	5
43										F9-H35	* Alloy/ Anneal: 30mins H2/N2 350degC 5'N2,30'H2/N2,5'N2. ELECTROPLATING All wafer join 9 total	5
												9
44										P-2	Photolith mask K965M EP, Dark Field: SU-8 100um resist	9
45										G-2	* See Engineer: INSPECT	9
46										G-3	* Special Instructions— Hardbake	9
47										P-RHBW	* Hardbake + Descum for 2 min	9
48										G-3	Electroplate Nickel	9
49										X-B	General inspection stage	9

B.5 Cantilevers with Electroplated Nickel Using SU-8

Photoresist

B	R	G	No	1	2	3	4	5	6	ID	Description	Count
										k2010s	NE-Naira Elejalde Micromachined magnetometers	
										red1	backside	
										g11		
			1							G-S12	* Title Page: 12 wafers. 5 ****SOI****, p-type Si thickness 4mu. 6 chuck wafers 17-33 test wafers, #1-6	0
			2							P-EM	E-BEAM Mask/Reticle Writing	0
			3							G-1P	Lithography Notes K965M	0
			4							G-1	Notebook page	0
										g3	IMPLANT B+ for whole area BLANKET IMPLANT B+, ****SOI**** wafers	0
			5							W-C2	Fuming Nitric acid clean, 2nd pot only **** SOI wafers only ****	6
			6							IB-3035	Implant Boron: 5E13 B+ 30KeV Wafer fronts	6
										g1	BACK ETCHING IN KOH BACK ETCHING IN KOH all wafers	0
			7							W-C1	RCA clean ALL WAFERS	12
			8							F4-W106	Initial ox. 600nm+-20nm, 1100degC, IdO2.rmpO2.x>wetO2.unldN2	12
			9							LN-160	Deposit Si3N4 160nm +- 20nm on BOTH SIDES	12
			10							P-GB	Photolith mask K965M BK, Dark Field 2.2um Resist on BACKS Fronts protected	12
			11							P-RHBW	* Hardbake for wet etch	12
			12							P-RG	* Spin resist on edges	12
			13							P-RHBD	* Hardbake for dry etch	12
			14							D-NO1F	Etch Si3N4, Anisot. from BACKS OPT80+ CHF3+Ar D/F EBMF/OPTICAL resist	12
			15							WH-7E1	Wet etch oxide, 7:1 BHF 25degC. To hydrophobic Si + 20secs.	12
			16							P-RS	Resist strip	12
			17							W-C2	Fuming Nitric acid clean, 2nd pot only	12
			18							WS-3	Etch silicon in KOH leave ~20um Si film	12
			19							WN-1	+ Strip/Wet etch Si3N4, Orthophosphoric acid 160degC	12
			20							G-3	* Special Instructions: Standard wafers Nos 1 - 6 only for spinning SU-8 photoresist	6
										g15	Electroplating Electroplating	0
			21							P-0	Photolith mask K965M EP Dark Field, SU8 100um resist	6
			22							G-2	* See Engineer: Inspect.	6
			23							P-0	+ photolith mask K965M V2, dark field: 1um resist	6
			24							G-2	* See Engineer for instructions	6
			25							P-0	+ Hardbake	6
			26							G-3	Electroplate Nickel	6
			27							G-3	* No further processing of wafers 1-6	6

B	R	G	No	1	2	3	4	5	6	ID	Description	Con
										red2	frontside CONTINUE WITH SOI WAFERS ONLY	
										g14	CONTACT WINDOW DOPING and mask for alignment	
											CONTACT WINDOW DOPING and FOR ALIGNMENT	0
			28							W-C2	Fuming Nitric acid clean, 2nd pot only	6
			29							P-G2	Photolith mask K965M NA, Dark Field: 2.2um Resist	6
			30							G-2	* See Engineer for instructions	6
			31							P-RHBW	* Hardbake for wet etch	6
			32							WH-7E1	+ Wet etch oxide, 7:1 BHF 25degC. To hydrophobic Si + 20secs. SOI WAFERS I	6
			33							IA-8055	Implant Arsenic: 5E15 As+ 80KeV	6
			34							P-RS	Resist strip	6
			35							W-C2	* Fuming Nitric acid clean, 2nd pot only	6
										g4	PIEZORESISTOR	
											PIEZORESISTOR	0
			36							P-G2	Photolith mask K965M PZ, Dark Field: 2.2um resist	6
			37							G-2	* See Engineer: inspect	6
			38							P-RHBI	* Hardbake for wet etch and Implant	6
			39							D-D60	Descum: 1 min. SRS barrel O2	6
			40							WH-7E1	+ Wet etch oxide, 7:1 BHF 25degC. To hydrophobic Si + 20secs. SOI WAFERS!	6
			41							IP-8	Implant PHOS+, 5E14 @ 80KeV	6
			42							P-RS	Resist strip	6
			43							W-C2	Fuming Nitric acid clean, 2nd pot only	6
										g6	SUBSTRATE CONTACT DOPING	
											SUBSTRATE CONTACT DOPING	0
			44							W-C1	RCA clean	6
			45							F4-W0010	* Wet oxidation 100nm+-10nm, 1000degC. 10'O2,x>wetO2,30"N2.	6
			46							P-G2	Photolith mask K965M PA, Dark Field: 2.2um Resist	6
			47							G-2	* See Engineer: inspect	6
			48							P-RHBI	* Hardbake for wet etch and Implant	6
			49							D-D60	Descum: 1 min. SRS barrel O2	6
			50							WH-7E1	Wet etch oxide, 7:1 BHF 25degC. To hydrophobic Si + 20secs. SOI WAFERS!	6
			51							IBF-7055	Implant BF2+: 5E15 BF2+ 70KeV	6
			52							P-RS	Resist strip	6
			53							W-C2	Fuming Nitric acid clean, 2nd pot only	6
			54							WH-7C1	Strip all SiO2 from wafer: 7:1 BHF 25degC	6

B	R	G	No	1	2	3	4	5	6	ID	Description	Count
										g7	PATTERN CANTILEVER	
											PATTERN CANTILEVER	0
			55							W-C1	RCA clean	6
			56							LO-400	LTO deposition: 400nm +/- 40nm at 400degC SiH4 and O2	6
			57							F10-8	Density LTO then anneal resistor, 1000degC 30min dryO2. Xr=0.5um, R=100-200/sg	6
			58							P-G2	Photolith mask K965M CL, Dark Field: 2.2um Resist	6
			59							G-2	* See Engineer: Inspect	6
			60							P-RHBW	* Hardbake for wet etch	6
			61							D-D60	Descum: 1 min. For OPTICAL resist SRS barrel O2	6
			62							WH-7E1	Wet etch oxide, 7:1 BHF 25degC. To hydrophobic Si + 20secs. SOI WAFERS!	6
			63							D-S2S	Deep etch Si. ~3.5um Partially anisot. OPT80+ SF6 THROUGH TO SOI OXIDE	6
			64							P-RS	Resist strip	6
										g8	CONTACT WINDOWS	
											CONTACT WINDOWS	0
			65							W-C2	Fuming Nitric acid clean, 2nd pot only	6
			66							P-G2	Photolith mask K965M CW, Dark Field 2.2um Resist:	6
			67							G-2	* See Engineer: Inspect	6
			68							P-RHBW	* Hardbake for wet etch	6
			69							D-D60	Descum: 1 min. SRS barrel O2	6
			70							WH-7E1	Wet etch oxide, 7:1 BHF 25degC. To hydrophobic Si + 20secs. SOI WAFERS!	6
			71							P-RS	Resist strip	6
										g9	DEPOSIT METAL FILM	
											DEPOSIT METAL FILM	0
			72							W-C2	Fuming Nitric acid clean, 2nd pot only	6
			73							WH-2D2	Dip etch, 20:1 BHF 25degC, 30 seconds. (Pre-metallisation)	6
			74							MS-TA10	Sputter 1000nm Ti-Al/Si 1% in TRIKON SIGMA	6
			75							P-G2	Photolith mask K965M M1, Light Field: 2.2um resist	6
			76							G-2	* See Engineer: Inspect	6
			77							P-RHBW	* Hardbake for wet etch	6
			78							WM-AST	Wet etch Al/Si+Ti, 3 Stage etch: Phos acid, Ti etch, Defreckle.	6
			79							P-RS	Resist strip	6
			80							W-C3	* Fuming Nitric Acid clean, metallised wafers	6
			81							F9-H35	Alloy/ Anneal: 30mins H2/N2 350degC 5'N2,30'H2/N2,5'N2.	6
										g12	Seed Layer	
											Seed Layer	0
			82							W-C3	* Fuming Nitric Acid clean, metallised wafers	6
			83							P-G2	Photolith mask K965M M2, Dark Field: 2.2um resist	6
			84							G-2	* See Engineer: Inspect	6
			85							P-RHBW	* Hardbake for wet etch	6
			86							WM-A2	+ Wet etch Al, Orthophosphoric acid, 37degC, till clear.	6
			87							P-RS	* Resist strip	6
			88							W-C3	* Fuming Nitric Acid clean, metallised wafers	6
										g13	Electroplating	
											Electroplating	0
			89							P-8	Photolith mask K965M EP Dark Field: SUB 100um resist	6
			90							G-2	* See Engineer: Inspect	6
			91							P-8	+ photolith mask K965M V2, dark field: 1um resist	6
			92							G-2	* See Engineer for instructions	6
			93							P-8	* Hardbake if required, see test wafers 1-6	6
			94							G-3	Electroplate Nickel	6
										red3	dry etching backside to release cantilever	
										g10	RELEASE CANTILEVER	
											RELEASE CANTILEVER	0
			95							D-S2X	Track etch Si: BACKS Au CONTAM PT RIE80 SF6, ~14um through to SOI oxide	6
			96							D-D1X	+ Etch SiO2 Anisot Au CONTAM PT RIE80 CHF3+Ar Backs of wafers	6
			97							G-2	See Naira for sawing instructions	6

B.6 Cantilevers with Electroplated Nickel Using SPR220-7 Photoresist

B	R	G	No	1	2	3	4	5	6	ID	Description	Cont
										k2059s	NE-Naiara Elejalde Micromachined magnetometers	
										red1	backside	
										g11		
			1							P-EM	E-BEAM Mask/Reticle Writing	0
			2							G-S12	* Title Page: 12 wafers, 6 ****SOI****, p-type Si thickness 4mu. 6 check wafers 17-33 test wafers, #1-6	0
			3							G-1P	Lithography Notes K965M	0
			4							G-1	Notebook page	0
										g3	IMPLANT B+ for whole area BLANKET IMPLANT B+, ****SOI**** wafers	0
			5							W-C2	Fuming Nitric acid clean, 2nd pot only **** SOI wafers only ****	6
			6							IB-3035	Implant Boron: 5E13 B+ 30KeV Wafer fronts	6
										g1	BACK ETCHING IN KOH BACK ETCHING IN KOH all wafers	0
												0
			7							W-C1	RCA clean ALL WAFERS	12
			8							F4-W106	Initial ox. 600nm+-20nm, 1100degC. IdO2.rmpO2.x>wetO2.unidN2	12
			9							LN-160	Deposit Si3N4 160nm +- 20nm on BOTH SIDES	12
			10							P-GB	Photolith mask K965M BK, Dark Field 2.2um Resist on BACKS Fronts protected	12
			11							P-RHBW	* Hardbake for wet etch	12
			12							P-RG	* Spin resist on edges	12
			13							P-RHBD	* Hardbake for dry etch	12
			14							D-NO1F	Etch Si3N4. Anisot. from BACKS OPT80+ CHF3+Ar D/F EBMF/OPTICAL resist	12
			15							WH-7E1	Wet etch oxide, 7:1 BHF 25degC. To hydrophobic Si + 20secs.	12
			16							P-RS	Resist strip	12
			17							W-C2	Fuming Nitric acid clean, 2nd pot only	12
			18							WS-3	Etch silicon in KOH leave ~20um Si film	12
			19							WN-1	+ Strip/Wet etch Si3N4, Orthophosphoric acid 160degC	12
												0
			20							G-3	* Special Instructions: Standard wafers Nos 1 - 6 only for spinning SU-8 photoresist	6
										g15	Electroplating Electroplating	0
			21							W-C2	* Fuming Nitric acid clean, 2nd pot only	6
			22							WH-7D1	Dip etch, 7:1 BHF 25degC. To hydrophobic Si + 20secs.	6
			23							MS-0	TRIKON SIGMA. Sputter Ti 250nm	6
			24							P-G2	* Photolith mask k965m M1 L/Field: nom. 2.2um resist (for trench or metal dry-etch)	6
			25							G-2	* See Engineer: INSPECT	6
			26							P-RHBW	* Hardbake for wet etch	6
			27							WM-0	Wet etch Ti	6
			28							P-RS	* Resist strip	6
			29							W-C3	* Fuming Nitric Acid clean, metallised wafers	6
			30							P-0	Photolith mask K965M EP Dark Field: SU8 100um resist	6
			31							G-2	* See Engineer: Inspect	6

B	R	G	No	1	2	3	4	5	6	ID	Description	Con
			32							P-8	* photolith mask K965M V2, Dark field 1um resist	6
			33							G-2	* See Engineer for instructions	6
			34							P-8	* Hardbake	6
			35							W-C3	* Fuming Nitric Acid clean, metallised wafers	6
			36							G-3	Electroplate Nickel	6
			37							G-3	* No further processing of wafers 1-6	6
										red2	frontside CONTINUE WITH SOI WAFERS ONLY	
										g14	CONTACT WINDOW DOPING and mask for alignment CONTACT WINDOW DOPING and FOR ALIGNMENT	0
			38							W-C2	Fuming Nitric acid clean, 2nd pot only	6
			39							P-G2	Photolith mask K965M NA, Dark Field: 2.2um Resist	6
			40							G-2	* See Engineer for instructions	6
			41							P-RHBW	* Hardbake for wet etch	6
			42							WH-7E1	* Wet etch oxide, 7:1 BHF 25degC. To hydrophobic Si + 20secs. SOI WAFERS !	6
			43							IA-8055	Implant Arsenic: 5E15 As+ 80KeV	6
			44							P-RS	Resist strip	6
			45							W-C2	* Fuming Nitric acid clean, 2nd pot only	6
										g4	PIEZORESISTOR PIEZORESISTOR	0
			46							P-G2	Photolith mask K965M PZ, Dark Field: 2.2um resist	6
			47							G-2	* See Engineer: Inspect	6
			48							P-RHBI	* Hardbake for wet etch and Implant	6
			49							D-D60	Descum: 1 min. SRS barrel O2	6
			50							WH-7E1	* Wet etch oxide, 7:1 BHF 25degC. To hydrophobic Si + 20secs. SOI WAFERS!	6
			51							IP-8	Implant P+10S+, 5E14 @ 80KeV	6
			52							P-RS	Resist strip	6
			53							W-C2	Fuming Nitric acid clean, 2nd pot only	6
										g6	SUBSTRATE CONTACT DOPING SUBSTRATE CONTACT DOPING	0
			54							W-C1	RCA clean	6
			55							F4-W001	* Wet oxidation 180nm+-10nm, 1800degC, 18'O2,x'wetO2.30"N2.	6
			56							P-G2	Photolith mask K965M PA, Dark Field: 2.2um Resist	6
			57							G-2	* See Engineer: Inspect	6
			58							P-RHBI	* Hardbake for wet etch and Implant	6
			59							D-D60	Descum: 1 min. SRS barrel O2	6
			60							WH-7E1	Wet etch oxide, 7:1 BHF 25degC. To hydrophobic Si + 20secs. SOI WAFERS!	6
			61							IBF-7055	Implant BF2+: 5E15 BF2+ 70KeV	6
			62							P-RS	Resist strip	6
			63							W-C2	Fuming Nitric acid clean, 2nd pot only	6
			64							WH-7C1	Strip all SiO2 from wafer. 7:1 BHF 25degC.	6

B	R	G	No	1	2	3	4	5	6	ID	Description	Count
										g7	PATTERN CANTILEVER	
											PATTERN CANTILEVER	0
			65							W-C1	RCA clean	6
			66							LO-400	LTO deposition: 400nm +/- 40nm at 400degC SiH4 and O2	6
			67							FT0-8	Densify LTO then anneal resistor, 1000degC 30min dryO2, X2=0.5um, R=100-200/sq	6
			68							P-G2	Photolith mask K965M CL, Dark Field: 2.2um Resist	6
			69							G-2	* See Engineer: Inspect	6
			70							P-RHBW	* Hardbake for wet etch	6
			71							D-D60	Descum: 1 min. For OPTICAL resist SRS barrel O2	6
			72							WH-7E1	Wet etch oxide, 7:1 BHF 25degC. To hydrophobic Si + 20secs. SOI WAFERS I	6
			73							D-S2S	Deep etch Si. ~3.5um Partially anisot. OPT80+ SF6 THROUGH TO SOI OXIDE	6
			74							P-RS	Resist strip	6
										g8	CONTACT WINDOWS	
											CONTACT WINDOWS	0
			75							W-C2	Fuming Nitric acid clean, 2nd pot only	6
			76							P-G2	Photolith mask K965M CW, Dark Field 2.2um Resist.	6
			77							G-2	* See Engineer: Inspect	6
			78							P-RHBW	* Hardbake for wet etch	6
			79							D-D60	Descum: 1 min. SRS barrel O2	6
			80							WH-7E1	Wet etch oxide, 7:1 BHF 25degC. To hydrophobic Si + 20secs. SOI WAFERS I	6
			81							P-RS	Resist strip	6
										g9	DEPOSIT METAL FILM	
											DEPOSIT METAL FILM	0
			82							W-C2	Fuming Nitric acid clean, 2nd pot only	6
			83							WH-2D2	Dip etch, 20:1 BHF 25degC, 30 seconds. (Pre-metallisation)	6
			84							MS-TA10	Sputter 100nm Ti-Al/Si 1% in TRIKON SIGMA	6
			85							P-G2	Photolith mask K965M M1, Light Field: 2.2um resist	6
			86							G-2	* See Engineer: Inspect	6
			87							P-RHBW	* Hardbake for wet etch	6
			88							WM-AST	Wet etch Al/Si+Ti, 3 Stage etch: Phos acid, Ti etch, Defreckle.	6
			89							P-RS	Resist strip	6
			90							W-C3	* Fuming Nitric Acid clean, metallised wafers	6
			91							F9-H35	Alloy/ Anneal: 30mins H2/N2 350degC 5"N2,30"H2/N2,5"N2.	6
										g12	Seed Layer	
											Seed Layer	0
			92							W-C3	* Fuming Nitric Acid clean, metallised wafers	6
			93							P-G2	Photolith mask K965M M2, Dark Field: 2.2um resist	6
			94							G-2	* See Engineer: Inspect	6
			95							P-RHBW	* Hardbake for wet etch	6
			96							WM-A2	* Wet etch Al, Orthophosphoric acid, 37degC, till clear.	6
			97							P-RS	* Resist strip	6
			98							W-C3	* Fuming Nitric Acid clean, metallised wafers	6
										g13	Electroplating	
											Electroplating	0
			99							P-0	Photolith mask K965M EP Dark Field: SPR220-7 5.4um resist	6
			100							G-2	* See Engineer: Inspect	6
			101							G-2	* See Engineer for instructions	6
			102							P-0	* Hardbake if required, see test wafers 1-5	6
			103							G-3	Electroplate Nickel	6
										red3	dry etching backside to release cantilever	
										g10	RELEASE CANTILEVER	
											RELEASE CANTILEVER	0
			104							D-S2X	Trench etch Si BACKS Au CONTAM PT RIE88 SF6 ~14um through to SOI oxide	6
			105							D-D1X	* Etch SiO2 Anisot. Au CONTAM PT RIE88 CHF3+Ar Backs of wafers	6
			106							G-2	See Nairara for sawing instructions	6

Appendix C

Finite Element Analysis

C.1 Determination of The Right Angle

/COM FEA model of a simple cantilever defined respect the angle theta of the arm.

/UNITS,SI

/PREP7

/TITLE, Modal analysis of simple cantilever paddles.

Stheta=0

Ftheta=0.698

Itheta=0.1745

*DO, theta,Stheta,Ftheta,Itheta

/prep7

K=0

*dim,fres,,1

arm = 250e-6 ! length of the arm

w2 = 40e-6 ! Width of the arm

$arm_l = arm \times \cos(\theta)$

pad_l = 200e-6 ! length of the paddle from the base

w1 = 30e-6 ! Width from the edge of the paddle to the arm

t = 3.5e-6 ! Thickness of the cantilever

$w3 = w2 + w1 - arm_l \times \sin(\theta)$

```
si = 1
! Keypoint defined
k,1
k,2,w1
k,3,w2+w1
k,4,w3,-arml
k,5,w3-w2,-arml
k,6,w1+w2+w1
k,7,w1+w2+w1,padl
k,8,w1+w2,padl
k,9,w1,padl
k,10,,padl
!AREA DEFINED
a,1,2,9,10
a,2,3,4,5
a,3,6,7,8
a,3,8,9,2
/COM Reflect half model
local,11,0,(w1+w2+w1)
arsymn,x,all
csys
/COM Definition of the element type
mat,si
et,si,63
r,1,t
! young's mod.
mp,ex,1,1.7e11
! Density
mp,dens,si,2.33e3
```

```
!Poisson ratio
mp,nuxy,si,0.28
!thermal expansion
mp,alpx,si,2.36e-6
/COM compress model and merge coincidences
numm,node,1e-6
numm,elem,1e-6
numm,kp,1e-6
numc,node
/COM Mesh the cantilever paddle
kesize,all,w2/4
amesh,all
/COM Fix nodes at base of Cantilever
nsel,s,loc,y,-arm1
d,all,all
nsel,all
/COM reorder nodes (to obtain a matrix easier to diagonalise)
waves
save, paddle
/SOLU
antype,2
modopt,subsp,1
mxpand,1
solve
FINISH
!postprocessing
/post1
K=K+1
!Smod=1
```

```

!Fmod=5
!Imod=1
*get,fres(K),mode,mod,freq
*CFOPEN,results,txt,,APPEND
*VWRITE,
("THETA",8X,"mode",8X,"Freq")
*VWRITE,theta,mod,fres(1)
(F6.5,6X,F3.1,8X,E12.6/)
*CFCLOSE
FINISH
!redirect output, clear screen and restart analysis with incremented angle
/output,junk
/clear,start
/output
*ENDDO

```

C.2 Iron Magnetic Particle

/COM, FE model of a simple cantilever paddle with an iron particle attached to it.

```

/UNITS, SI
/prep7
/title, Iron Magnetic Particle
! Parameters used to define keypoint positions
arml = 250e-6 ! Length of the arm
w1 = 40e-6 ! Width of the arm
padl = 450e-6 ! Length of the paddle from the base.
w2 = 130e-6 ! Right width of the paddle
w3 = 160e-6 ! Left width of the paddle
w4 = 90e-6
w5 = 60e-6

```

t = 3.5e-6 ! Thickness of the cantilever paddle

si = 1

fe = 2

c = 2.5e-8

/COM, Keypoints and area geometry.

!Keypoints defined

k,1

k,2,w1

k,3,w2,arm_l

k,4,w3,arm_l

k,5,w3,pad_l

k,6,w2,pad_l

k,7,w4,pad_l

k,8,w5,pad_l

k,9,w5,arm_l

k,10,w4,arm_l

!Area defined

a,1,2,3,10

a,3,4,5,6

a,3,6,7,10

a,7,8,9,10

/COM, Reflect half model

local,11,0,w3

arsymm,x,all

csys

/COM, Definition of element type

mat,si

et,si,shell99

r,1,1

```
rmore
rmore,1,,t
rmore
r,2,2
rmore
rmore,1,0,t,2,0,c
!Young's Mod.
mp,ex,1,1.7e11
mp,ex,2,211.4e11
!Density
mp,dens,si,2.33e3
mp,dens,2,8000
!Poisson Ratio
mp,nuxy,si,0.28
mp,nuxy,2,0.293
!thermal expansion
mp,alpx,si,2.3e-6
mp,alpx,2,11.8e-6
/COM, Compress model and merge coincidences
numm,node,1e-6
numm,elem,1e-6
numm,kp,1e-6
numc,node
/COM, Mesh the cantilever paddle
kesize,all,w1/4
amesh,all
/COM, Fix nodes at base of cantilever
nsel,s,loc,y
d,all,all
```

```
nselect,all
esel,s,elem,,224
esel,a,elem,,223
and all the other needed elements
emodif,all,real,2
emodif,all,mat,2
esel,all
/COM, Reorder nodes
waves
save,paddle
finish
/solu
antype,static
acel,0,0,10
pstres,on
outpr,basic,1
solve
finish
/solu
antype,modal
modopt,subsp,2
mxpand,2
pstres,on
solve
!finish
```

C.3 Mass Sensitivity with Iron Magnetic Particle

/COM FEA model of the cantilever sensitivity, change of frequency vs. mass.

```
/UNITS,SI
```

```
/PREP7
/TITLE, BLABLABLA
Sthick=600e-6
Fthick=7.875e-4
Ithick=0.125e-4
*DO,thick,Sthick,Fthick,Ithick
/prep7
K=0
*dim,fres,,1
! Parameters used to define keypoint positions
arml = 250e-6 ! Length of the arm
w1 = 40e-6 ! Width of the arm
padl = 450e-6 ! Length of th paddle from the base.
w2 = 130e-6 ! Right width of the paddle
w3 = 160e-6 ! Left width of the paddle
w4 = 90e-6
w5 = 60e-6
t = 2e-6 ! Thickness of the cantilever paddle
si = 1
fe = 2
c = thick !thickness of the magnetic particle
/COM, Keypoints and area geometry.
!Keypoints defined
k,1
k,2,w1
k,3,w2,arml
k,4,w3,arml
k,5,w3,padl
k,6,w2,padl
```

```
k,7,w4,padl
k,8,w5,padl
k,9,w5,arml
k,10,w4,arml
!Area defined
a,1,2,3,10
a,3,4,5,6
a,3,6,7,10
a,7,8,9,10
/COM, Reflect half model
local,11,0,w3
arsymm,x,all
csys
/COM, Definition of element type
mat,si
et,si,shell99
r,1,1
rmore
rmore,1,,t
rmore
r,2,2
rmore
rmore,1,0,t,2,0,c
rmore
!Young's Mod.
mp,ex,1,1.7e11
mp,ex,2,211.4e11
!Density
mp,dens,si,2.33e3
```

```
mp,dens,2,8000
!Poisson Ratio
mp,nuxy,si,0.28
mp,nuxy,2,0.293
!thermal expansion
mp,alpx,si,2.3e-6
mp,alpx,2,11.8e-6
/COM, Compress model and merge coincidences
numm,node,1e-6
numm,elem,1e-6
numm,kp,1e-6
numc,node
/COM, Mesh the cantilever paddle
kesize,all,w1/2
amesh,all
/COM, Fix nodes at base of cantilever
nsel,s,loc,y
d,all,all
nsel,all
esel,s,elem,,54
esel,a,elem,,41
and all the other needed elements
emodif,all,real,2
emodif,all,mat,2
esel,all
/COM, Reorder nodes
waves
save,paddle
/solu
```

```
antype,modal
modopt,subsp,2
mxpand,2
solve
finish
!postprocessing
/post1
K=K+1
Smod=1
Fmod=2
Imod=1
*Do,mod,Smod,Fmod,Imod
*get,fres(K),mode,mod,freq
*CFOPEN,results,txt,,APPEND
*VWRITE,
("THICK",8X," mode",8X," Freq")
*VWRITE,thick,mod,fres(1)
(F6.5,6X,F3.1,8X,E12.6/)
*CFCLOS
*enddo
FINISH
!redirect output, clear screen and restart analysis with incremented thickness
/output,junk
/clear,start
/output
*ENDDO
```

Publications

1. N. Elejalde, *et al.*, 'Development of a Device to Measure Small Changes Based on Resonating Microfabricated Structures', MME'99, 105-108, (Sept. 1999), Gif-sur-Yvette, France.
2. N. Elejalde, *et al.*, 'Positive and Negative Photoresist as Thick Moulds for Electroplating High Aspect Ratio 3D Structures', MME'01, 11-14, (Sept. 2001), Cork, Ireland.
3. S. Lee, *et al.*, 'Micromechanical Sensors for Specific Chemical Detection', Royal Academy of Engineering, UK Focus for Biomedical Engineering, Sept. 2002, Aston, Birmingham.
4. L. Grigore, *et al.*, 'On Optimisation of Nickel Electroforming for MEMS Applications', MME'02, 83-86, (Oct. 2002), Bucharest, Romania.

Contributed Talks and Posters

1. Poster on 'Resonating Microfabricated Structures for Nanogramic Detection', Second Euroconference on Nanoscience and Nanotechnology, Nov. 1999.
2. Poster on 'Magnetically actuated microfabricated devices for application in molecular probe chemistry', Homogeneous Fluorescent Reporting systems for Real-Time Quantitative PCR: Optimisation, Probe Technology & Future Systems., Sept. 2001, Winchester, UK
3. Talk on 'Desarrollo de un Sensor Micromecanizado Para Detección Bio/Química', Electricity and Electronics Department, Euskal Herriko Unibertsitatea, Bilbao, May 2002.

Acknowledgements

My most sincere thanks are for Prof. Steven Lee. First of all for giving me the opportunity to carry out this research, and then for the support and advice.

I would like to thank Prof. Alan G. Evans for allowing us to use the clean room facilities in Southampton University, and for all the good suggestions during those four years.

Dr. Graham Ensell, thank you very much for all you help, explanations, suggestions and so on along the way.

I would also like to thank Dr. Feodore Ogrin for all his help in my first months, and all the input towards this project.

Dr. Luminita Grigore, thanks for the work done to fulfill the last batch of cantilevers, especially in improving the electroplating bath and optimising the last step.

I would like to take this opportunity to thank the DSTL for my studentship.

In the white kitchen:

Corrie, for having so much patience and explaining whatever, whenever I asked.

Elaine, for her help and tips with the photolithography and the subtleties of the English language.

Richard, for this, and that, and the other thing, and the car and that time when you pretended to drop all my wafers after all I had to go through...

Jean, the chef, for letting me jump the queues, and for putting up with me in my orphan times...

Paul, for introducing me to the incredible world of 'cooking'.

Trevor, for the very basics of the 'ugly' world, and Ruth for all her 'advice' in FEA...

Graham, for those first group meetings, and last ones... 'proof reading' a few chapters, and being one of the most patient person I've ever met.

And all the other 'cooks' for their help and their cheerfulness.

In the back kitchen:

Sandrine et Mikäel, Mikäel et Sandrine, mes bons amis, qu'est ce que j'aurais fait sans vous... certainement j'aurais finie en deux mois !

Muchisímas gracias van para Ibone y Juan Mari, por estar siempre al otro lado del teléfono escuchando mis pataletas y dándome consejos, incluso cuando los demás salían corriendo al oír mi tono... Fijo que sin vosotros hubiese sido demasiado poco diplomática, sobre todo para los estandards de por aquí. Además de ese apoyo moral, y ese empuje para que solucionase el 'pequeño' problema.

Peñari, nola esan, mila bider esandakoa? Nola esan? Nola esango det?

Ruth and Carl, many many many thanks for putting up with me, specially Ruth as she had to do it so many times... Just lovely to spend all that time with you, I only hope I will be able 'to pay back', but rather than in Southampton, in Bilbao!!!, after all you must be dying to visit, like Sandrine and Mikäel, and Michael, and Dominik, and Mir, and Nele, and Jim, and Ketan, and Becky, and all the others I came across...

Shannon and Paul should also be mentioned, even if I told you a thousand times you wouldn't be mentioned... after all you've always been in the thick of it...

And Ben, for that needed last push.

YO OPINARÍA QUE...
PERO MEJOR NO
TOCAR EL TEMA ¿NO?



I would 'have to' say that...
but it's probably best to
avoid the subject, isn't it?